INFORMATION TO USERS

This manuscript has been reproduced from the microfilm master. UMI films the text directly from the original or copy submitted. Thus, some thesis and dissertation copies are in typewriter face, while others may be from any type of computer printer.

The quality of this reproduction is dependent upon the quality of the copy submitted. Broken or indistinct print, colored or poor quality illustrations and photographs, print bleedthrough, substandard margins, and improper alignment can adversely affect reproduction.

In the unlikely event that the author did not send UMI a complete manuscript and there are missing pages, these will be noted. Also, if unauthorized copyright material had to be removed, a note will indicate the deletion.

Oversize materials (e.g., maps, drawings, charts) are reproduced by sectioning the original, beginning at the upper left-hand corner and continuing from left to right in equal sections with small overlaps.

Photographs included in the original manuscript have been reproduced xerographically in this copy. Higher quality 6" x 9" black and white photographic prints are available for any photographs or illustrations appearing in this copy for an additional charge. Contact UMI directly to order.

Bell & Howell Information and Learning
300 North Zeeb Road, Ann Arbor, MI 48106-1346 USA
800-521-0600

UMI®

ATMOSPHERIC MODEL AND DATA ANALYSIS IN TERMS OF EMPIRICAL NORMAL MODES

By

Dinh Hai Tran

SUBMITTED IN PARTIAL FULFILLMENT OF THE
REQUIREMENTS FOR THE DEGREE OF
DOCTOR OF PHILOSOPHY
AT
McGILL UNIVERSITY
MONTREAL, QUEBEC
JULY, 1998

0-612-50323-2

Dedicated to my parents: Ban Tran and Thinh Thi Luong

Abstract

The Empirical Orthogonal Function (EOF) analysis technique has proven to be one of the most powerful methods to analyze data in meteorology and many other fields. However, this method is statistical only and has no physical basis. Brunet (1994) has introduced Held's (1985) concept of conservation of wave activity and orthogonal functions into the EOF analysis and called it the "Empirical Normal Mode" (ENM) analysis technique. This new method uses both statistical concepts from the classical EOF analysis method and a dynamical constraint from the generalized Eliassen-Palm theorem to ensure that the functions that we obtained are orthogonal to each other and are the solutions of linearized dynamical equations.

In this thesis, we use the ENM analysis to analyze data from both a (2D) shallow water model integration and from 3-D atmospheric observations, with an emphasis on stratospheric sudden warming events.

For the shallow water model case, the results of the ENM analysis are evaluated by testing against the theoretical (numerical) normal mode solutions provided by Longuet-Higgins (1968). It is shown that the ENM analysis can recover the spatial structures and the frequencies of the normal modes with a great degree of accuracy if the temporal record is sufficiently long. The average errors in the periods for 2000 and 100 day time series are found to be 1% and 4.6%, respectively. From the eigenvalues (percentage of the total variance) and sharp frequency peaks associated with normal modes, the ENM analysis shows that the model generates only a few modes with monochromatic frequencies. The method can be used to test a new or modified shallow water model integration or to study other Hough modes generated by different kinds of forcings.

Having shown the value of the ENM technique in a barotropic context, we advance further by performing an ENM analysis on an 11 year atmospheric data set. In this study, we focus on stratospheric warming events. The winter (DJF) data set is partitioned into warming and non-warming periods in order to characterize the flow differences between the regimes. The stratospheric quasi-potential vorticity or wave activity structure in the warming period is found to be much stronger, as expected, than in the non-warming periods. The ENM analysis clearly shows the tropospheric difference between the two periods, e.g., a higher wave activity in the main tropospheric structure as well as in the tropospheric polar regions in the warming periods. The analysis also reveals that there is a higher level of stratospheric wave activity during the warming periods in the second normal mode of zonal wave number 1 but the tropospheric structures of the quasi-potential vorticity are the same as during non-warming periods. This suggests that there is/are (a) mechanism(s) associated with the stratospheric warming other than the upward wave propagation. All the common features of the stratospheric warming event are captured by the first two normal modes of zonal wave numbers 1 and 2, such as wave-mean flow interaction leading to the deceleration of the zonal mean wind, the polar vortex being displaced by the northward movement of the Aleutian High, as well as wave amplitude enhancement/reduction during the growing/decaying stages.

Résumé

La méthode d'analyse des fonctions orthogonales empiriques (EOF) est une des plus puissantes pour l'analyse de données en météorologie et en beaucoup d'autres domaines. Cependant, cette méthode n'est que de nature statistique et n'a pas de base physique. Brunet (1994) a introduit le concept de Held (1985) de la conservation de l'activité ondulatoire et des fonctions orthogonales dans l'analyse EOF et l'a nommée la méthode des modes normaux empiriques (ENM). Cette nouvelle méthode emploie des concepts statistiques de l'analyse EOF et une contrainte dynamique provenant du théorème généralisé de Eliassen-Palm pour s'assurer que les fonctions soient orthogonales et qu'elles soient les solutions d'équations dynamiques linéaires.

Dans cette thèse, nous utilisons la méthode ENM pour analyser des données provenant d'un modèle barotrope (équations de Saint-Venant) et des observations météorologiques en trois dimensions, en mettant l'accent sur des épisodes de réchauffement stratosphériques subits.

Les résultats de l'analyse ENM pour les données du modèle sont comparés avec les solutions des modes normaux théoriques (numériques) de Longuet-Higgins (1968). Nous démontrons que l'analyse ENM peut capturer les structures spatiales et les fréquences des modes normaux avec une grande précision si la série temporelle est suffisamment longue. Les erreurs moyennes des périodes d'oscillation sont de 1% et 4,6% pour des dennées disponibles sur 2000 jours et 100 jours, respectivement. L'analyse ENM montre que le modèle produit seulement quelques modes avec des fréquences

monochromatiques. La méthode peut être utilisée pour tester d'autres intégrations modifiées du modèle des équations de Saint-Venant ou pour étudier d'autres modes Hough produits par différents forçages.

Après avoir démontré l'importance de la méthode ENM dans un contexte barotrope, nous continuons avec une analyse ENM de données atmosphériques couvrant 11 ans. Dans cette étude nous nous concentrons sur les événements de réchauffement stratosphérique. Les données d'hiver (DJF) sont séparées entre des périodes de réchauffement et des périodes sans réchauffement pour pouvoir caractériser les différences entre la dynamique des deux régimes d'écoulement. Le tourbillon quasi-potentiel stratosphérique ou la structure de l'activité ondulatoire pendant les périodes de réchauffement est, comme prévue, beaucoup plus forte que pendant les périodes sans réchauffement. L'analyse ENM démontre clairement les différences troposphériques entre les deux périodes, e.g., une plus grande activité ondulatoire dans la structure troposphérique principale aussi bien que dans les régions troposphériques polaires pendant les périodes de réchauffement. L'analyse montre aussi une forte activité ondulatoire stratosphérique pendant les périodes de réchauffement pour le deuxième mode normal du nombre d'onde zonal 1 mais les structures troposphériques du tourbillon quasi-potentiel ne diffirent pas. Cela implique qu'il y a au moins un autre mécanisme pour expliquer le réchauffement stratosphérique autre que la propagation verticale d'ondes. Toutes les caractéristiques communes aux réchauffements stratosphériques sont reproduites par les deux premiers modes des nombres d'onde 1 et 2. Par exemple, la décélération du vent zonal moyen produite par l'interaction entre les ondes et l'écoulement moyen, le déplacement du vortex polaire à cause du mouvement vers le nord de l'anticyclone aléoutien, et aussi l'augmentation/la réduction des amplitudes des ondes pendant les phases de croissance/décroissance.

Acknowledgments

I would like to express my deepest thanks to my supervisors, Professor Jacques Derome and Dr. Gilbert Brunet, for their guidance throughout this work. Their constant encouragements and invaluable assistances made my study at McGill an enjoyable experience. I benefited greatly from their profound and extensive knowledge of atmospheric dynamics.

I am indebted to Dr. William J. Randel for his permission to use the 11 year Geopotential Height data set in Chapter 4 of this thesis.

I acknowledge Alan Schwartz' help in solving some computer problems. I would also like to thank Marc Klasa who helped me proof-read part of this thesis.

I would thank the Natural Sciences and Engineering Research Council, the Atmospheric Environment Service of Canada and the Canadian Middle Atmosphere Model (MAM) project for financial support during my study.

Finally I would like to thank all my family members, especially my sisters Minh Hien Tran and Xuan Phuong Tran, for their patience, understanding and support.

Contents

List of Tables

List of Figures

List of Symbols

a: Earth's radius (6.371×10^6 m)

$a_n(t)$: time series

$\mathbf{a}$: position in phase space, Eq. (4.11)

$\dot{\mathbf{a}}$: rate of change of position, Eq. (4.12)

$\mathcal{A}$: wave activity density

c: zonal phase speed of a wave, Eq. (1.1)

k, l: zonal and meridional wave number, Eq. (1.1)

$\mathbf{k}$: unit vector along the z axis, Eq. (4.3)

f: Coriolis parameter ($\equiv 2\Omega \sin \phi$)

$f(\alpha, \mathbf{a})$: Gaussian distribution function, Eq. (4.11)

f_o: midlatitude value of Coriolis parameter

g: acceleration of gravity ($\equiv 9.81$ m s^{-2})

h: perturbation height (sections 2.2 and 3.1)

h_m: mountain height, Eq. (3.4)

h_o: mountain height amplitude. Eq. (3.4)

n: length of time series

n_k^2: refractive index, Eq. (1.2)

p: pressure

p_o: reference pressure ($\equiv$ 1000 hPa)

q: quasi-geostrophic potential vorticity

q_ϕ: latitudinal quasi-geostrophic potential vorticity gradient

t: time

u: eastward component of velocity

v: northward component of velocity

(u_g, v_g): geostrophic wind components

w: Gaussian weighting factor, Eq. (2.12); z component of velocity (upward), Eq. (A.2)

x, y: eastward and northward distance, respectively

$\overline{v^*}, \overline{w^*}$: the residual meridional circulation, Eqs. (1.4)-(1.5)

z: vertical coordinate in log-pressure system

C, **G**: covariance matrix, Eqs. (1.19) and (2.11)

D: frictional and diabatic terms, Eq. (1.10)

E: pseudoenergy matrix, Eq. (3.12)

F: The Eliassen-Palm flux

F_n: Empirical Orthogonal Function

$\bar{\mathrm{J}}$: Ertel potential vorticity gradient, Eq. (A.14)

H: scale height ($\equiv$ 7 km), Eq. (1.1); Shallow Water Model mean depth (section 2.2)

L: self-adjoint matrix, Eq. (2.40)

$\mathbf{M}$: pseudomomentum matrix

N: sample size, Eq. (2.21)

N^2: square of the bouyancy, Eq. (1.1)

P: Ertel potential vorticity (Appendix A)

$\mathbf{P}$: self-adjoint matrix, Eq. (2.40)

$\mathbf{Q}$: self-adjoint matrix, Eq. (3.11)

$\overline{Q}$: diabatic heating rate, Eq. (1.7)

R: gas constant for dry air, Eq. (A.18)

T: number of observations, Eq. (2.21); temperature, Eq (4.1)

$\mathbf{V}$: horizontal velocity vector

X: wave vector

$\mathrm{X}_n, \mathrm{Y}_n$: Eigenvector, EOF or ENM

X, Y, Z: components of friction force per unit mass, Eqs. (3.1–3.3)

Z: geopotential height (section 4.1)

α: the field to be smoothed, Eq. (4.11)

β: $\equiv df/dy$, variation of the Coriolis parameter with latitude

γ: PV gradient, Eq. (1.21), $(\equiv \epsilon^{-\frac{1}{2}})$ dimessionless parameter section 3.4

$\delta\lambda$: sampling error, Eq. (2.21)

ϵ: dimensionless parameter, Eq. (3.5); relative wind change between each iteration and the previous step, Eq. (4.9)

ζ: relative vorticity

η: barotropic non-divergence wave function, Eq. (1.30); basic state absolute vorticity, Eq. (A.4)

θ: potential temperature

κ: (= 2/7) ratio of the gas constant and specific heat at a constant pressure

λ: longitude, positive eastward

λ_n: eigenvalue

ρ_o: background atmospheric density

ϕ: latitude

χ: zonal Fourier component of the wave function or wave vector

ψ: streamfunction

ω_n: frequency, Eq (3.16)

Δ: difference

Π: modified Ertel potential vorticity in log-pressure coordinate

Φ: Geopotential (section 4.1)

Ω: angular velocity of the earth (=7.292×10^{-5} rad s^{-1})

$\bar{a}$: zonal and time mean

$\overline{a'b'}$: zonal mean

$()'$: departure from time average

$()_o$: basic state

$\{...\}$: time average

$< ... >$: domain average

∇: horizontal gradient operator

∇^2: Laplacian

Statement of Originality

The original results contained in this thesis are as follows:

1) For the first time we have used the Empirical Normal Mode Analysis technique to recover the Hough functions and their associated frequencies from the data generated by a Shallow Water Model intergation (linearized version with a basic state at rest). The results showed that both the normal modes (ENMs) and their associated frequencies are in good agreement with theoretical (numerical) results from Longuet-Higgins (1968) in all aspects.

2) Neither the Empirical Orthogonal Function (EOF) nor Empirical Normal Mode (ENM) analysis has been used before to analyze the structure of the real atmosphere for the stratospheric sudden warming events. We use the ENM analysis to investigate the structural difference between the non-warming and warming periods;

3) By comparing the empirical modal structurres of the quasi-potential vorticity and thus the wave activity during the warming events and with those for the rest of the data, we have found that the wave activity in the stratosphere during the warming events is much stronger than that of the non-warming periods, especially for the zonal wave number 1;

4) If the "cause" of the stratospheric warming is the propagation of the wave activity from below then this would be reflected in tropospheric structure differences between the warming events and the rest of the data set. These structure differences appeared in the first (most important) empirical modes for both zonal wave numbers

1 and 2 from the ENM analysis in the high latitude region.

5) The phase diagram of the empirical normal mode of the warming periods have never been studied before. By partitioning the warming periods into the growing and decaying stages, we investigated the phase space of each empirical model structure. The results showed that during the growing stage, the modal amplitudes of wave number 1 were increasing with eastward phase speeds. In contrast, the modal amplitudes were reduced during the decaying stage with an eastward phase speed found in ENM1 and a more complex phase propagation in ENM2;

6) During the growing stage of the warming events, the northward motion of the Aleutian High pushing the polar vortex off the pole along the Greenwich meridian is clearly seen in the first two empirical modes of the zonal wave number 1. This polar vortex is restored when the zonal mean temperature returns to the normal winter condition. The evolution of the zonal wave number 1 has a preferred phase (along 0-180° longitude line) and time (usually at the begining of the warming) while the occurrence of wave number 2 does not.

Chapter 1

Introduction

In the past two decades, a considerable amount of work has been done to understand the dynamics and chemistry of the stratosphere. Observational and theoretical research has been quite successful, especially for the stratospheric chemistry. The stratosphere, an atmospheric layer that extends from about 10 to 50 km above the ground, contains the ozone layer which absorbs most of the harmful solar ultra-violet radiation before it reaches the ground. This absorption is associated with photochemical processes in the ozone layer. Ozone depletion has been a topic of scientific and public interest for more than a decade. Much of the research in this field dealt with chemical interactions and photo-dissociation that are quite well known. The result of solar ultra-violet absorption by the ozone layer is a warming of the stratosphere, leading to a vertical temperature inversion. Without this ozone layer, there would be no stratosphere. The existence of the ozone layer is important not only for the general circulation in the stratosphere but also for the protection of the biosphere. Although ozone is formed mainly in the tropics at an altitude of about 25 km, high ozone concentrations (in term of mixing ratio) are found in the low stratopheric polar region, so that there must exist a dynamical mechanism to transport ozone out of the source region. To properly understand the stratosphere one needs to combine chemistry, dynamics and their interactions. In this thesis we concentrate on the dynamics of the stratosphere by analyzing observational data using a relatively new statistical method.

The main scientific goal of this research is to use the relative new statistical method of Empirical Normal Mode analysis to study stratospheric warming events in three dimensions, an approach which has never been used before. It will be of interest to see how the new analysis technique helps characterize the dynamics of stratospheric warmings.

We briefly review the basic dynamics in this chapter to explain the climatological observations in the stratosphere. The Eliassen and Palm (EP) flux is also introduced in section 1.2 as a diagnostic tool to explain the wave-zonal mean flow interaction. One of the most striking phenomena observed in the stratosphere is the sudden polar warming event. It has been known from climatological data that in the middle stratosphere the zonal wind in winter is generally westerly (from west) and the temperature decreases from the middle latitudes towards the winter pole. Every few years this normal pattern is abruptly changed in midwinter. The polar stratospheric temperature increases rapidly, leading to the reversal of the latitudinal temperature gradient, and the westerly zonal wind is replaced by an easterly (from east) one. We describe the possible mechanism which causes this phenomenon in section 1.3. In the last section we discuss a new statistical method to analyze data. It is different from other statistical methods in that it uses dynamical equations as a constraint to construct a statistical variable. This new *Empirical Normal Mode Analysis* method is argued to be a better technique than the ordinary *Empirical Orthogonal Function Analysis* on the basis of an analysis done on the output of a global barotropic non-divergent model.

1.1 Overview of the Stratospheric Dynamics

The atmosphere is conventionally divided into layers based on its vertical temperature profile. The troposphere is defined to be the region from the ground to the tropopause; in this layer the temperature normally decreases with height. The thickness of the troposphere is about 15 km at the equator and 9 km at the poles. Even though the layer is relatively thin in comparison with the others, the troposphere contains about 80% of the mass of the atmosphere and almost all its water vapour. The weather disturbances are found in this layer. Above the troposphere is the stratophere, in which the temperature increases with height to the stratopause (about 50 km from the Earth's surface or at the 1 hPa pressure level). Although this layer has less mass than the troposphere, the stratosphere can affect the tropospheric dynamics due to the strength and position of the strong jet (polar night jet).

Boville (1984) has used the NCAR (National Center for Atmospheric Research) Community Climate Model to show that the position and strength of the stationary planetary waves and the level of transient eddy activity in the troposphere are affected by the polar night jet, located in the stratosphere. If in a model the polar night jet is too strong, then more planetary waves are trapped in the troposphere due to the change of the refractive properties of the mean flow. A model without a stratosphere may permit vertically propagating waves to be reflected at the top of the model. Some models, e.g., the Canadian Middle Atmosphere Model (Shepherd *et al.* 1996), use a "sponge layer" (an artificial absorbing layer) at the top of the model to avoid wave reflection into the lower domain.

The observed Northern Hemisphere climatology from 11 winters (DJF) (Dec. 1, 1979 to Feb. 28, 1990) of the zonal mean temperature and wind from 700 hPa to 1 hPa are shown in Figures 1.1 and 1.2, respectively. Figure 1.1 illustrates the basic temperature structure which has a minimum at the equatorial tropopause. The temperature decreases with height in the troposphere and generally increases with height in the stratosphere. A fairly uniform temperature decrease from the Southern Hemisphere (summer hemisphere) to the Northern Hemisphere (winter hemisphere) is observed in the upper stratosphere. The zonal mean wind diagram (Fig. 2) shows a winter hemisphere westerly jet located at about 45 degrees of latitude in the upper stratosphere and the lower mesosphere, called the polar night jet. Similarly, there is an easterly jet in the summer hemisphere.

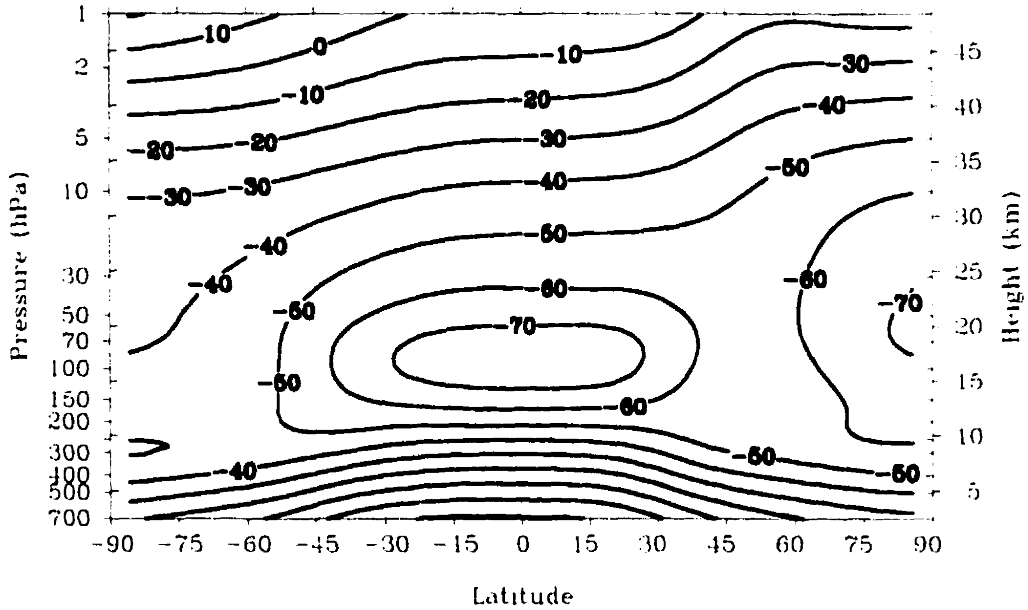

Figure 1.1: Observed climatological zonal temperature from 11 Northern Hemisphere winters (DJF) (Dec. 1, 1979 to Feb. 28, 1990). Contour interval is 10°C.

Figures 1.3a and 1.3b show the average polar stereographic charts of geopotential height of 11 northern winters and southern summers (DJF) at 10 hPa, respectively. Similarly, Figures 1.3c and 1.3d illustrate the southern winters and northern summers (JJA). From the four Figures 1.3a-d, we observe that only the Northern winter Hemisphere (1.3a) polar vortex is distorted, whereas the others are fairly zonally

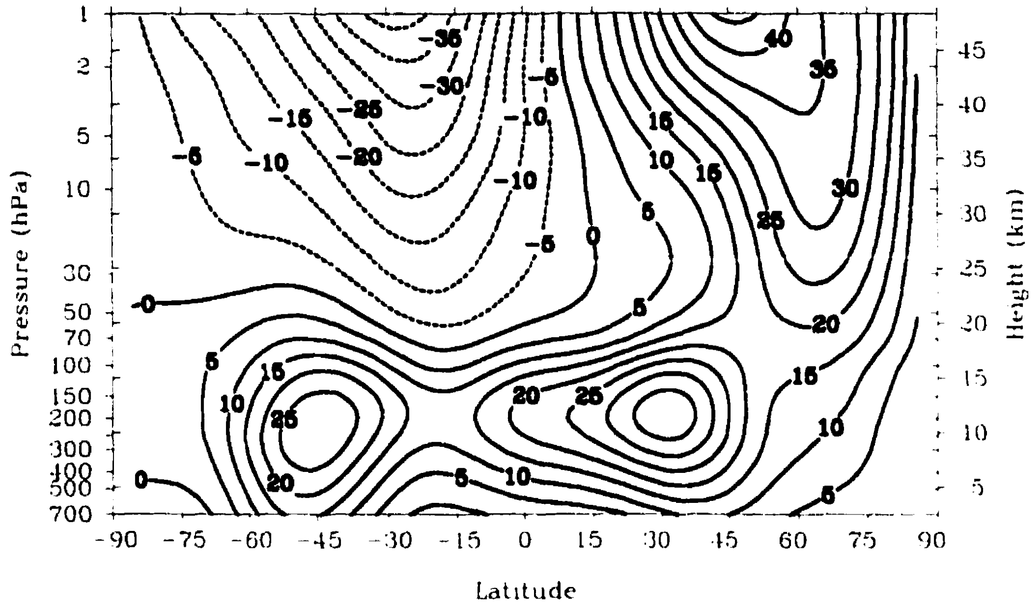

Figure 1.2: Observed climatological zonal wind from 11 Northern Hemisphere winters (DJF) (Dec. 1, 1979 to Feb. 28, 1990). Contour interval is 5 ms^{-1}.

symmetric. This suggests that the existence of the stationary planetary waves in the Northern winter Hemisphere is produced by upward propagating waves forced from the troposphere by the orography and land-sea thermal contrast.

Apart from the existence of free traveling planetary waves, most planetary waves in the middle atmosphere appear to propagate upward from the forcing regions in the troposphere. Charney and Drazin (1961) were the first to discuss in detail the vertical propagation of planetary waves. They used a linearized, midlatitude β-plane, quasi-geostrophic (QG) model [the model restricted to large scale, low frequency motions; see Andrews *et. al.* (1987) section 3.2.3 for more details] to investigate conditions under which vertical wave propagation is possible. They found that QG waves can propagate vertically when

$$0 < \bar{u} - c < \bar{u}_c \equiv \beta(k^2 + l^2 + f_o^2/4H^2N^2)^{-1} \qquad (1.1)$$

where $\bar{u}$ is the background zonal mean wind, c is the wave phase speed, β is the

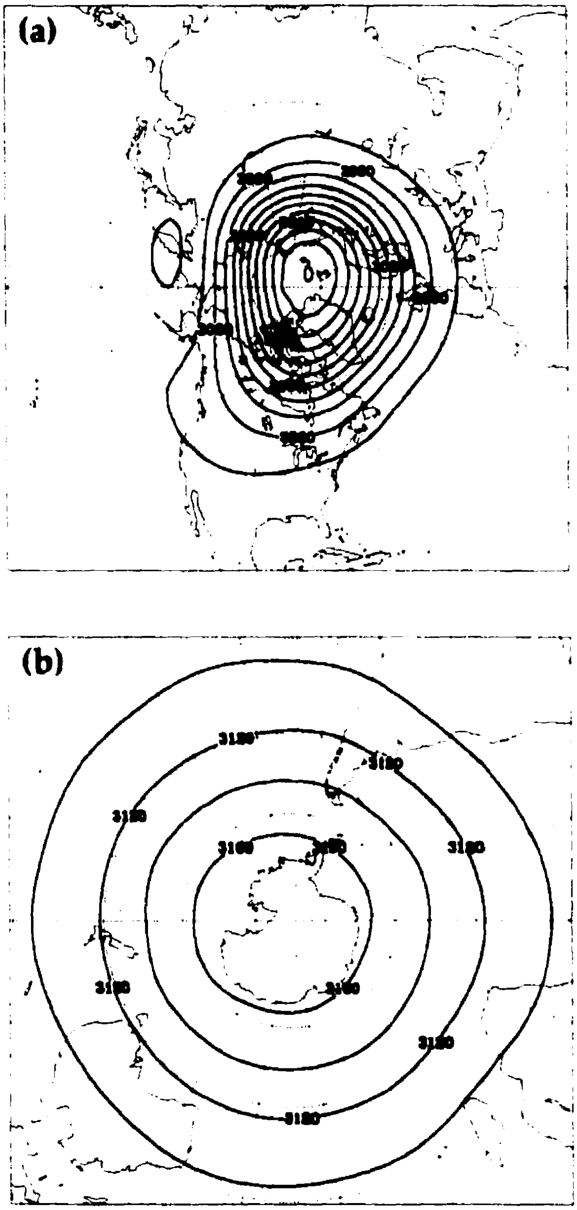

Figure 1.3: Observed climatological (1980-1990) polar stereographic charts of 10 hPa geopotential height for: **(a)** Northern Hemisphere winters (DJF), **(b)** Southern Hemisphere summer (DJF), **(c)** Southern Hemisphere winters (JJA) and **(d)** Northern Hemisphere summer (JJA). The contour interval is 30 dam. Latitude circles are shown at 20° intervals, with the outermost circle at 20°. *Figure continued)*

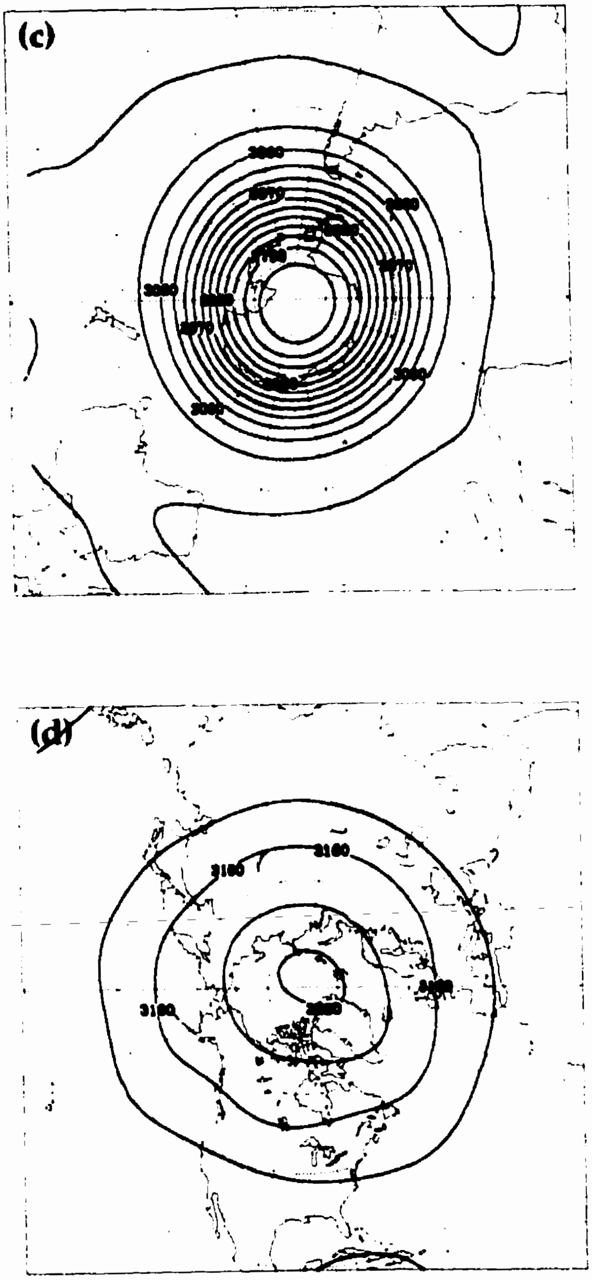

Figure 1.3: *continued*

derivative of the Coriolis parameter with respect to y ($\equiv a(\phi - \phi_o)$) evaluated at latitude $\phi = \phi_o$=45°, f_o is the midlatitude value of the Coriolis parameter, a is radius of the Earth, H is the scale height ($\equiv$ 7 km), N^2 is the square of the buoyancy frequency and k, l are respectively the zonal and meridional wave numbers. Here $\bar{u}$ and N are assumed to be constants. For a stationary wave (c=0 relative to the ground), the criterion states that only ultra-long waves (that is, two dimensional wave number $K^2 = k^2 + l^2$ sufficiently small to make $\bar{u}_c > \bar{u}$) in the presence of a westerly mean flow ($\bar{u} > 0$) can propagate upward. All other waves are trapped in the troposphere. Also in an easterly background flow ($\bar{u} < 0$) no vertical propagation is possible. Even though the real atmospheric zonal mean flow varies with height and latitude, the Charney and Drazin criterion agrees broadly with the observation that the stratospheric waves are predominately composed of Fourier components of zonal wave numbers 1, 2 and 3 in the winter westerlies and tend to be absent in the summer easterlies. In the case of traveling waves, equation (1.1) also shows us that Rossby waves with an eastward phase speed ($c > 0$) more easily satisfy the propagation criterion than waves with a westward phase speed ($c < 0$).

The vertically propagating stationary planetary waves in the winter Northern Hemisphere were first quantitatively investigated in detail by Matsuno (1970). He used a linearized quasi-geostrophic model on a sphere with the perturbation meridional wind modified to include an ageostrophic term which was called the "isallobaric" wind. The ageostrophic term is included to ensure energetic consistency. Similarly to the Charney-Drazin criterion, Matsuno introduced a refractive index which is analogous to the refractive index in the theory of acoustics or optics, n_k^2.

$$n_k^2 = \frac{\bar{q}_\phi}{a\bar{u}} - \frac{k^2}{a^2\cos^2\phi} - \frac{f^2}{4N^2H^2} \tag{1.2}$$

where

$$\bar{q}_\phi = 2\Omega\cos\phi - \left[\frac{(\bar{u}\cos\phi)_\phi}{a\cos\phi}\right]_\phi - \frac{a}{\rho_o}\left(\frac{\rho_o f^2}{N^2}\bar{u}_z\right)_z$$

is the latitudinal potential vorticity gradient, k is zonal wave number and ρ_o is the background atmospheric density. Notice that the log-pressure, z, is used as the vertical coordinate which is defined as

$$z \equiv -H \ln\left(\frac{p}{p_o}\right) \tag{1.3}$$

where p and p_o are pressure and the reference pressure, usually taken at 1000 hPa, respectively. We will use the vertical log-pressure coordinate throughout this thesis. Waves can only propagate in the regions where the refractive index is large and positive, and are prohibited where n_k^2 is negative. From equation (1.2) we see that longer waves (smaller k) are more favourable for propagation than shorter ones. Matsuno concentrated on the hypothesis that the stationary planetary waves in the stratosphere of the Northern Hemisphere winter are forced from below. Based on this hypothesis he imposed the 500 hPa observed geopotential height as the lower boundary condition in his numerical model. A realistic zonal mean wind fields varying with latitude and height was used for the basic state. The results from Matsuno's model were in good agreement with observations, especially in the simulation of the upward propagation of wave number 1, though the wave number 2 amplitude decayed more rapidly with height than in the observations. Once again the Charney-Drazin criterion was qualitatively confirmed. Later, Lin (1982) used more sophisticated models to study the vertical propagation of planetary waves to the stratosphere from below. He pointed out that the upward propagation of ultra-long waves is sensitive to the zonal mean wind structure and the latitudinal position of the polar night jet.

1.2 The Eliassen-Palm Flux

In this section we introduce the Eliassen-Palm (EP) flux and its divergence as a diagnostic tool to study the stratospheric dynamics and the interaction between the planetary-scale Rossby waves and the zonal mean flow, an interaction that plays an important role in stratospheric sudden warming events. For simplicity, we discuss the EP flux using a midlatitude β-plane formulation. The EP flux for a more complex model such as one with 3D primitive equations in spherical geometry will be discussed in the next chapter. The EP flux vector is defined in equation (1.10), having the eddy momentum flux ($\overline{u'v'}$) in the north-south direction and meridional eddy heat flux ($\overline{\theta' v'}$) in the vertical direction.

The usefulness of the EP flux and its divergence was well-appreciated when Andrews and McIntyre (1976) introduced the concept of the residual mean meridional circulation and the transformed Eulerian-mean (TEM) equations. The motivation behind this transformation is that there is a strong cancelation between the meridional eddy heat flux convergence and the adiabatic cooling in the zonal mean thermodynamic equation (see Holton 1992 section 10.2.2). The residual meridional circulation is the circulation due to the diabatic processes, and is defined as

$$\overline{v^*} = \bar{v} - \rho_o^{-1}\frac{\partial}{\partial z}\left(\frac{\rho_o \overline{v'\theta'}}{\theta_{oz}}\right) \tag{1.4}$$

$$\overline{w^*} = \bar{w} + \frac{\partial}{\partial y}\left(\frac{\overline{v'\theta'}}{\theta_{oz}}\right) \tag{1.5}$$

where θ_o is the basic state potential temperature that always increases with height, and ρ_o is the basic state density. The vertical velocity component, $\overline{w^*}$, defined here is just the difference in contribution between the adiabatic term and the meridional eddy heat flux divergence. With the above definition of residual circulation ($\overline{v^*}, \overline{w^*}$), the zonal mean momentum, thermodynamic, mass continuity and thermal wind balance equations are transformed to

$$\bar{u}_t - f_o\overline{v^*} = \rho_o^{-1}\nabla\cdot\ \mathbf{F} \tag{1.6}$$

$$\bar{\theta}_t + \overline{w^*}\theta_{oz} = \overline{Q} \tag{1.7}$$

$$\bar{v}^*_y + \rho_o^{-1}(\rho_o \overline{w^*})_z = 0 \qquad (1.8)$$

$$f_o \bar{u}_z + H^{-1} R \exp\left(-\frac{\kappa z}{H}\right) \bar{\theta}_y = 0 \qquad (1.9)$$

where $\overline{Q}$ is the diabatic heating rate. The EP flux vector in this quasi-geostrophic β-plane formulation is

$$\mathbf{F} \equiv (-\rho_o \overline{v'u'}, \rho_o f_o \overline{v'\theta'}/\theta_{oz}) \qquad (1.10)$$

and its divergence is

$$\nabla \cdot \mathbf{F} \equiv -(\rho_o \overline{v'u'})_y + (\rho_o f_o \overline{v'\theta'}/\theta_{oz})_z \qquad (1.11)$$

where the subscripts y and z denote differentiation with respect to the meridional and vertical directions.

Under the Transformed Eulerian Mean (TEM) formulation, equation (1.6) clearly shows that the eddy heat and the momentum fluxes act together as an EP flux divergence to change the zonal mean flow. This property of the EP flux divergence is used as a diagnostic tool to study the wave-mean flow interaction. For a steady, linear and conservative system the EP flux divergence vanishes $\nabla \cdot \mathbf{F} \equiv 0$ (Edmond *et. al.* 1980). Later, Eliassen and Palm's work was extended to include frictional and diabatic effects in spherical geometry by Boyd (1976) and non-steady disturbances (i.e., transient waves) by Andrews and McIntyre (1976, 1978). The *generalized Eliassen-Palm theorem* has the form

$$\frac{\partial A}{\partial t} + \nabla \cdot \mathbf{F} = D + O(\alpha^3) \qquad (1.12)$$

where A, D and $\mathbf{F}$ are quadratic functions of disturbance quantities. The quantity A is called the *wave-activity density* and its time differentiation represents the transient effect, D contains frictional and diabatic terms and $O(\alpha^3)$ represents non-linear terms, α being a measure of the disturbance amplitude. Notice that the above generalized EP theorem is not restricted to the QG model. However, under the QG approximation, the EP flux $\mathbf{F}$ is defined by equation (1.10) and the wave activity density $\mathcal{A}$ has the form

$$\mathcal{A} \equiv \frac{1}{2}\rho_o \frac{\overline{q'^2}}{\overline{q}_y} \tag{1.13}$$

where the disturbance QG potential vorticity q' and the latitudinal gradient $\overline{q}_y$ of its mean zonal counterpart are defined as:

$$q' \equiv -u'_{gy} + v'_{gx} + \frac{f_o}{\rho_o}\left(\frac{\rho_o \theta'}{\theta_{oz}}\right)_z \tag{1.14}$$

$$\overline{q}_y \equiv \beta - (\overline{u_g})_{yy} + \frac{f_o}{\rho_o}\left(\frac{\rho_o \overline{\theta}_y}{\theta_{oz}}\right)_z \tag{1.15}$$

where u_g and v_g are the geostrophic wind components. Thus under the generalized Eliassen-Palm theorem, the physical properties of the flow can be clearly seen. For example, for the steady ($\partial\mathcal{A}/\partial t = 0$), linear ($O(\alpha^3) = 0$) and conservative ($D = 0$) disturbances, the EP flux divergence vanishes ($\nabla \cdot \mathbf{F} = 0$). Therefore under the stated conditions, the total eddy force on the mean flow disappears in the TEM formulation. By contrast, under the same conditions, the ordinary Eulerian-mean momentum and thermodynamics equations are

$$\begin{aligned} \bar{u}_t - f_o\bar{v} &= -(\overline{v'u'})_y \\ \bar{\theta}_t + \theta_{oz}\bar{w} &= \bar{Q} - (\overline{v'\theta'})_y. \end{aligned} \tag{1.16}$$

The eddy forcing terms ($(\overline{v'u'})_y$ and $(\overline{v'\theta'})_y$) are generally non-zero. In general one cannot easily anticipate how the zonal-mean flow and temperature will respond to these eddy forcing terms.

Some properties of the EP flux and its divergence which can be used as diagnostic tools to study the stratosphere are summarized as follows:

(1) The EP flux vector represents the wave activity flow from one latitude and height to another (equation (1.12)).

(**2**) In the TEM formulation, the eddy heat and eddy momentum fluxes are combined together as a single term, EP flux divergence, which is used to study the wave-mean flow interaction (equation (1.6)).

(**3**) For steady, linear and conservative disturbances, the EP flux is non-divergent (equation (1.12)) and therefore there is no change in zonal mean flow and temperature (equations (1.6) and (1.7)).

(**4**) Under linear and conservative conditions (but not steady), the EP flux divergence can be used to study the temporal variation of the wave activity (equation (1.12) and the temporal variation of the mean zonal wind equation (1.6)).

1.3 The Stratospheric Sudden Warming

As shown in Figures 1.1 and 1.2, the middle and upper stratosphere temperature decreases poleward, except at the tropical tropopause, and westerly zonal winds are generally found in the winter hemisphere. Every few years in the northern winter, the meridional gradient of the zonal mean temperature and occasionally the wind direction are reversed. This event is called a *stratospheric sudden warming.* Stratospheric sudden warmings are classified in two groups: minor and major warmings. In a minor warming the poleward gradient of the 10 hPa zonal mean temperature reverves so that temperature increases poleward, but the flow remains westerly. In a major warming the reversal of both temperature and zonal mean wind (to easterly) near the polar region takes place. In some years the polar temperature has dramatically risen by as much as 40-60 degrees Kelvin within a week at the 10 mb level. Following a change in temperature leading to a poleward increase in zonal mean temperature (minor warming), on occasion the zonal mean wind reverses and becomes easterly (major warming).

The Northern Hemisphere winter 84/85 stratospheric major warming is exhibited

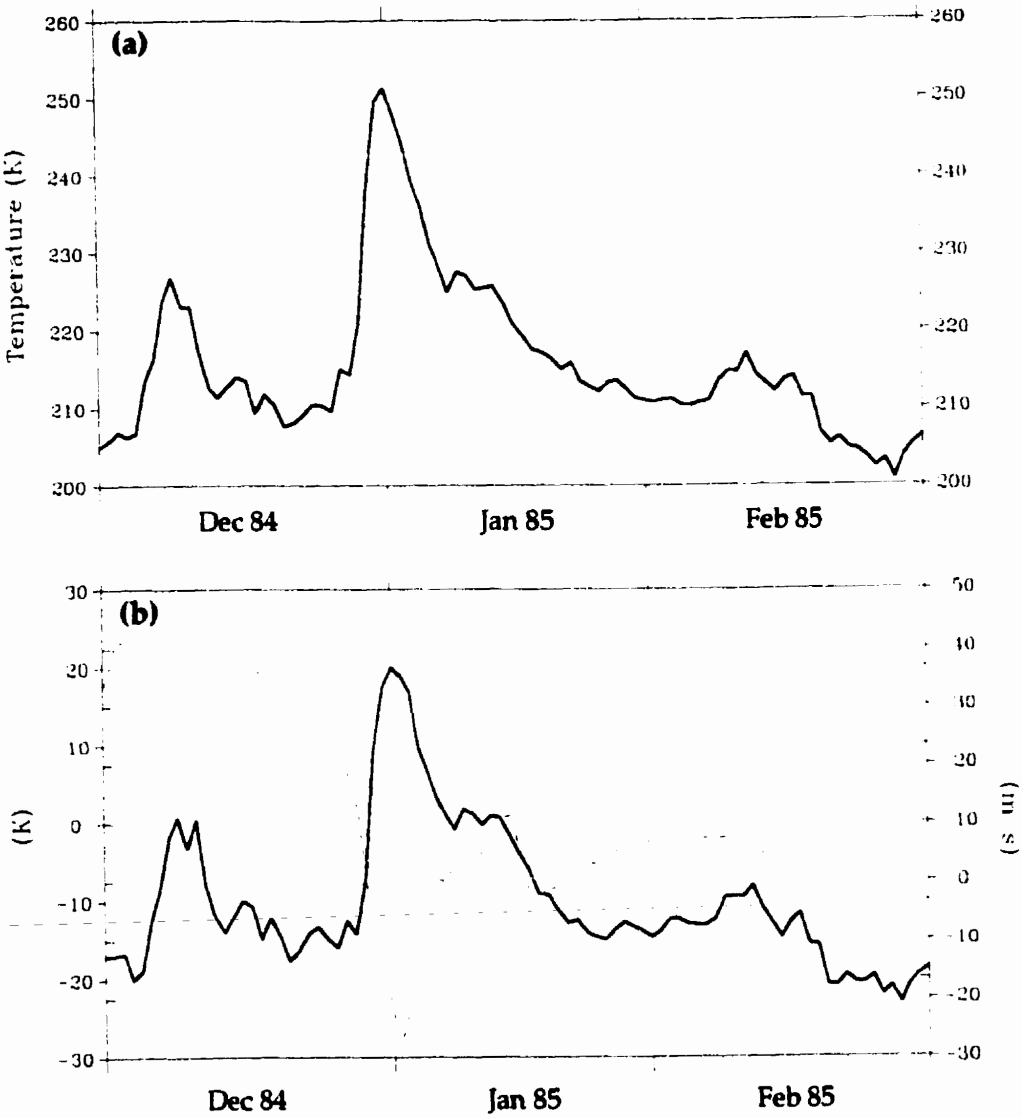

Figure 1.4: Observed winter 84/85 (DJF) major warming at 10 hPa (**a**) zonal mean temperature at 80° and (**b**) zonal mean temperature difference between 80° and 50° (solid) and zonal mean wind at 65° (dashed).

in Figure 1.4. Figure 1.4a shows the zonal mean temperature near the pole (at 80°N) in the middle stratosphere (10 hPa). The temperature rises more than 40 degrees Kelvin in 4 days. The warming episode peaks around Jan. 1. Figure 1.4b illustrates the zonal temperature difference (ΔT) between latitudes of 80°N and 50°N (solid curve). The normal negative temperature difference in winter is replaced by a positive one during the warming period. The zonal mean zonal wind at latitude of 65°N (dashed curve) becomes easterly (negative wind speed) and resumes to westerly after the ensuing cooling episode.

During sudden warming years the normal cyclonic polar vortex is elongated and pushed off the pole and sometimes splits. Stratospheric sudden warmings are observed in the Northern Hemisphere, but not in the Southern Hemisphere. It is believed that because of the large amplitude of the zonal mean wind in the Southern Hemisphere winter (large latitudinal gradient of geopotential height, Figure 1.3(c)), a much stronger forcing is required to reverse the wind direction. More importantly, the tropospheric forcing due to the vertical ultra-long wave propagation is relatively weaker in the Southern Hemisphere than in the Northern Hemisphere because of the lack of topographically forced waves.

Matsuno (1971) was the first to demonstrate numerically that stratospheric sudden warmings can be induced by the upward propagation of planetary (Rossby) waves from the troposphere and their interaction with the zonal mean flow in the stratosphere. According to the Charney and Drazin (1961) non-acceleration theorem, if the perturbations are steady, linear and conservative then the waves induce no mean flow change ($\bar{u}_t = 0$). However the zonal mean wind is observed to decelerate during the sudden warming period, which implies that some of the theorem's conditions are violated during this event. Within the sudden warming time scale (less than a week), the energy conservation condition is approximately satisfied because the radiative and frictional dissipations are relatively small. Thus, for a linear system, the theorem's only condition which is clearly violated is that of the steady waves. To see how transient (non-steady) waves can induce the change in the zonal mean wind (the transient waves–mean flow interaction), for simplicity, we consider a barotropic model (height independent variables) for which the zonal mean potential vorticity tendency takes the form

$$\frac{\partial q}{\partial t} = -\frac{\partial \overline{q'v'}}{\partial y} \tag{1.17}$$

where the potential vorticity flux is given by

$$\overline{q'v'} = -\frac{1}{2\overline{q_y}}\frac{\partial \overline{q'^2}}{\partial t} \tag{1.18}$$

and

$$\overline{q} = f_o + \beta y - \overline{u}_{yy}; \tag{1.19}$$

q' and $\overline{q_y}$ are as defined in equations (1.14) and (1.15) without the last terms (vertical derivative terms). Substituting (1.18) and (1.19) into (1.17) we obtain

$$\frac{\partial \overline{u}_g}{\partial t} = -\frac{1}{2\overline{q_y}}\frac{\partial \overline{q'^2}}{\partial t}. \tag{1.20}$$

Therefore, for a growing wave ($\overline{q'^2}$ increasing with time) equation (1.20) shows that there will be a decrease in zonal mean wind with time provided $\overline{q_y}$ is positive (as observed in the stratosphere). Even though we use a simple barotropic model to discuss how transient waves alter the zonal mean flow here, the same conclusion can be found in Holton (1992) for a more sophisticated model.

To illustrate how a transient waves-mean flow interaction can give rise to the stratospheric sudden warming, we consider an idealized system whose Eliassen-Palm (EP) flux is positive (constant) below some z_o level and zero above that (see Figure 1.5a). This configuration can be caused by a wave being "turned on" and propagating upward at some time t=0. At some time t=t$_o$, the leading edge of the wave packet has reached up to level z_o. Above z_o the flux vanishes (no wave there) and below z_o the flux is (nearly) constant because the wave is "steady". At z_o there is a jump

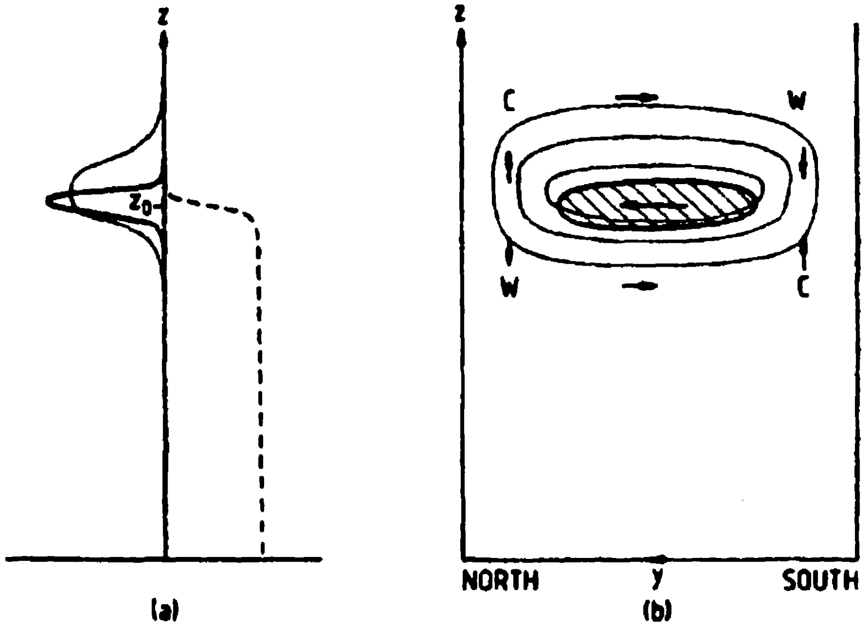

Figure 1.5: Schematic description of the interaction with the zonal-mean flow of a transient vertically propagating planetary-wave during the stratospheric warming. (a) Height profiles of EP flux (dashed), EP flux divergence $\nabla \cdot \mathbf{F}$ (heavy line) and zonal mean wind acceleration (thin line); z_0 is the level reached by the leading edge of the wave packet. (b) Meridional-height diagram showing the region where EP flux is convergent (hatched), contours of induced zonal (negative) acceleration (thin lines) and the induced residual circulation $(\overline{v^*}, \overline{w^*})$ (arrows). Regions of warming (W) and cooling (C) associated with $\overline{w^*}$ are also shown [From Andrews *et. al.* 1987].

in the flux, i.e. at the leading edge of the wave. According to equation (1.6) the deceleration of zonal mean wind must follow in the region of EP flux convergence. A part of this EP flux convergence will be balanced by the Coriolis term of the residual mean meridional circulation $(f_0\overline{v^*})$ which implies increasing $\overline{v^*}$. Since the residual meridional wind, $\overline{v^*}$, increases in the region of EP flux convergence it will induce a vertical circulation required by continuity (Figure 1.5b). Referring to equation (1.7), the downward motion associated with negative $\overline{w^*}$ below and north of the convergence region will warm the polar region ($\partial\overline{\theta}/\partial t > 0$ for $\overline{w^*} < 0$). As the winter westerly zonal mean flow decelerates, a critical line (where $\overline{u} - c$=0) may be formed, with $\overline{u} - c < 0$ above, which prevents waves from propagating upward (equation (1.1)). This process causes the region of EP flux convergence to move downward. With the right initial conditions, e.g., large wave amplitude, a zonal mean wind distribution that is favourable for upward and poleward wave propagation, a stratospheric sudden warming can result.

1.4 The Statistical Analysis

In the analysis of Stratospheric warming events it is naturally of interest to use statisticcal tools that yield the maximum information. We will use the Empirical Normal Mode (ENM) analysis, which as we will see, is an extension of the Empirical Orthogonal Function (EOF) analysis technique. The ENM technique is attractive in that it is constructed from the set of dynamical equations so that it has a physical as well as statistical basis. data is the Empirical Normal Mode (ENM) analysis. This method is not only a pure

Empirical Orthogonal Function analysis has proven to be one of the most powerful statistical techniques to analyze long-time meteorological records over a large domain. This technique is used to find an orthogonal complete set of spatial functions to represent the dataset. This set of orthogonal functions is constructed based on the dataset itself through the calculus of variation while other conventional orthogonal functions, e.g., Fourier series, Legendre polynomial, etc. have a fixed basis. The choice of fixed basis functions is usually dependent on the geometry of the domain over which data are to be analyzed. In contrast, the EOF analysis automatically adapts the functions to the domain of interest and the structures of functions depend on the data. By construction, EOFs represent the most variance with the least number of functions (patterns). The EOFs, F_n, of the dataset are the solutions of the eigenvalue problem

$$\mathbf{C}F_n = \lambda_n F_n \tag{1.21}$$

where **C** is the covariance matrix whose elements $c_{ij} = < f_i f_j >$ are two-location (i and j) covariances of variable f and the angle brackets denote an ensemble average or time mean, and λ_n is the eigenvalue corresponding to eigenfunction F_n. Each eigenvector has a time series (or coefficients) that modulates it. For a non-degenerated case, each eigenvalue associated with a different eigenvector gives the percentage of total variance explained by the particular eigenvector. Eigenvalues are usually arranged in a descending order to show the degree of importance of each eigenvector. For example, if we analyze a one-year data set of surface temperature fields, we may obtain an eigenvalue $\lambda_1 = 0.5$ (50%), a pattern F_1 and a time series of F_1. This means that F_1 represents 50% of the total variance and the plot of the time series would be expected to represent the annual cycle. The spatial function F_1 should have a large scale structure in the middle and high latitudes where the temperature has a large temporal variance in comparison to the tropical regions.

The EOF analysis is of course not limited to analyzing meteorological data. It has widely been used in many other fields, especially in computer science. The most basic application of EOF analysis in computer science is to compress data for storage. Another well-known application of EOF analysis in computer science is in *face recognition.* The approach is to use human pictures to construct eigen-pictures. From these eigen-pictures, an algorithm can easily and quickly identify whether a person is a member of an ensemble (of persons) in the database. [see Sirovich and Everson(1992) for more technical details about the *face recognition*]

Kutzbach (1967) used this technique to analyze sea-level pressure, surface temperature and precipitation at 23 points in North America for 25 Januaries. Legler (1983) applied Hardy and Walton's (1978) technique, by considering the horizontal vector wind field (u,v) as complex numbers, e.g., $\mathbf{u}=u+iv$, to analyze the tropical Pacific winds from 1961 to 1978. Kutzbach has given a precise description of this analysis technique and physical interpretation of the results.

Even though EOF analysis is a powerful tool to analyze data in terms of *orthogonal functions*, this technique is, however, statistical only and has no physical basis. To illustrate this we use a simple linearized non-divergent barotropic model on a β-plane. The conservation of absolute vorticity can be written as

$$\left[\frac{\partial}{\partial t}+u_o\frac{\partial}{\partial x}\right]\zeta'+\gamma v'=0, \tag{1.22}$$

where $u_o(y)$ is basic state zonal wind, ζ' and v' are the perturbation (relative) vorticity and meridional wind, respectively, γ is the latitudinal gradient of the basic state absolute vorticity (PV gradient) and is defined as

$$\gamma=\beta-\frac{\partial^2 u_o}{\partial y^2}. \tag{1.23}$$

The non-divergent winds and relative vorticity are defined as

$$(u,v)=\left(-\frac{\partial\psi}{\partial y},\frac{\partial\psi}{\partial x}\right) \tag{1.24}$$

and

$$\zeta=\frac{\partial v}{\partial x}-\frac{\partial u}{\partial y}=\nabla^2\psi, \tag{1.25}$$

where ψ is the streamfunction. We assume that ζ' and ψ' have the form

$$[\zeta'(x,y,t),\psi'(x,y,t)]=\sum_{k=0}^{\infty}\sum_{n=1}^{\infty}[\zeta_{kn}(y),\psi_{kn}(y)]\,e^{ik(x-c_{kn}t)}+c.c. \tag{1.26}$$

so that ζ' and ψ' are 2π periodic in x. For a particular zonal wave number k (dropping subscript k hereafter), substituting (1.26) into (1.22) we have

$$(u_o-c_n)\zeta_n+\gamma\psi_n=0. \tag{1.27}$$

If we write another equation like (1.27) with subscript m, then multiply the m-equation by ζ_n and the n-equation by ζ_m and subtract, this yields

$$(c_n - c_m)\zeta_m\zeta_n + \gamma(\zeta_n\psi_m - \zeta_m\psi_n) = 0 \tag{1.28}$$

or

$$(c_n - c_m)\frac{\zeta_m\zeta_n}{\gamma} = \frac{\partial}{\partial y}\left(\psi_m\frac{\partial\psi_n}{\partial y} - \psi_n\frac{\partial\psi_m}{\partial y}\right). \tag{1.29}$$

Integrating the above equation over a channel with boundary condition

$$\psi_n(y) = 0 \qquad \text{at} \qquad y = 0, L \tag{1.30}$$

the right-hand side of equation (1.29) vanishes, so that we have

$$(c_n - c_m)\int_0^L \frac{\zeta_m\zeta_n}{\gamma}\mathrm{d}y = 0 \tag{1.31}$$

or

$$(c_n - c_m)\int_0^L \eta_m\eta_n\mathrm{d}y = 0, \tag{1.32}$$

where $\eta_n(y) = \zeta_n(y)/\sqrt{\gamma}$ is the wavefunction. The wavefunctions are orthogonal to each other, that is,

$$\int_0^L \eta_m\eta_n\mathrm{d}y = 0 \qquad \text{if} \qquad m \neq n. \tag{1.33}$$

We can show from (1.22) that

$$\frac{\partial}{\partial t}\left(\frac{\overline{\eta'^2}}{2}\right) = \frac{\partial}{\partial y}(\overline{u'v'}), \tag{1.34}$$

where the overbar denotes a zonal average. From (1.34) we can see that the square of the wavefunction is conserved over the channel providing $v = 0$ at $y = 0, L$. The conserved quantity P is called the pseudomomentum (or wave activity in the above model) and is defined as

$$P = -\int\frac{\eta'^2}{2}\mathrm{d}y = -\int\frac{1}{2}\frac{\zeta'^2}{\gamma}\mathrm{d}y. \tag{1.35}$$

Thus if we perform an EOF analysis on the relative vorticity, ζ, the eigenvectors $\{\zeta_i, i = 1, N\}$ are orthogonal to each other, e.g., $\int \zeta_m \zeta_n dy = \delta_{mn}$. According to (1.31) the normal modes, ζ_m, are, in general, not orthogonal to each other if $m \neq n$ unless γ is a constant. In other words, the orthogonal eigenvectors (EOFs) of the relative vorticity are not solutions of the dynamical equation (1.22).

Held (1985) has pointed out this non-orthogonality. Thus the total eddy enstrophy $\{\zeta, \zeta\} \equiv \int \zeta\zeta dy$ and eddy energy $\{\psi, \zeta\}$ cannot be expressed as the sum of contributions of normal modes. This implies that the energy or entrophy of a normal mode is not constant in time. Held has also shown the relationship between the conservation law and modes: if a quantity (squared wave amplitude) is conserved then the normal modes are orthogonal to each other. In the above model, modes of the wavefunction, η, are orthogonal to each other, but not those of the relative vorticity ζ.

Brunet (1994) has used the relationship between the conservative property of wave activity and the orthogonality to bring the concept of a conservative norm (time invariance of the trace of the covariant matrix in EOF analysis) into the EOF analysis technique. For a linear and conservative system, with the right choice of a variable, the EOFs are just the normal modes of the dynamical equation. In the above example, the variable is $\eta = \zeta/\sqrt{\gamma}$, not ζ. The choice of variable can be found with the help of the generalized Eliassen-Palm theorem

$$\frac{\partial \mathcal{A}}{\partial t} + \nabla \cdot \ \mathbf{F} = 0. \tag{1.36}$$

The area integrated wave activity, $\mathcal{A}$, is conserved if there is no EP flux divergence when integrated over the domain. In other words, either the normal flux vanishes on the domain boundary or, less strictly, the fluxes into the domain is equal to the fluxes out of the domain. The method of EOF analysis with a conserved norm was introduced and called by Brunet *Empirical Normal Mode Analysis.*

Chapter 2

Statistical Diagnosis

In this chapter we first discuss the Empirical Orthogonal Function (EOF) analysis technique as a statistical method to analyze data. From the conservative property of the wave activity and the orthogonality of EOFs we introduce the Empirical Normal Mode Analysis technique for the Shallow Water Model and for the primitive equations in the sections 2.2 and 2.3.

2.1 Empirical Orthogonal Function Analysis

In this section we review the EOF analysis technique which has been discussed in a number of articles. In meteorology, the EOF analysis results can have strong dependence on the geometry of the analysis domain. The selected data points should be chosen in such a way that they represent equal areas in the domain (Kutzbach 1967). Since we use the spherical geometry throughout this thesis, the EOF analysis is derived to work with each zonal Fourier component separately. We also consider the effect of the sample size on the eigenvectors (EOFs) associated with small eigenvalues. This was discussed in detail by North *et al.* (1982). This review provides a background to understand the Empirical Normal Mode analysis in the subsequent chapters.

Empirical orthogonal function (EOF) analysis, also known as principal components analysis (PCA), has been shown to be a most powerful statistical technique to analyze meteorological data. It is used to separate large spatial and temporal records into patterns (eigenvectors) and their corresponding time series (coefficients). The EOF analysis matrix formulation can be expressed in the form of an eigenvalue problem as

$$\mathbf{C}\mathbf{X}_i = \lambda_i \mathbf{X}_i \tag{2.1}$$

where **C** is the covariance matrix whose elements, $c_{ij} =< T_i T_j >$, are the correlations of the variable T at two locations i and j and the angle brackets denote an ensemble average (time mean). Each of the patterns (EOFs) which represents the spatial structure of the data set is associated with an eigenvalue (partial variance) that explains the degree of importance of the corresponding eigenvector. The time series of the amplitude of a specific eigenvector is used to see the temporal variability of that pattern. The spatial functions or eigenvectors have certain advantages over conventional orthogonal functions such as Fourier series, Legendre polynomial etc.. For example, the construction of the eigenvectors is based on observed data through the calculus of variation while other conventional functions have fixed bases. The eigenvalues are arranged in descending order

$$\lambda_1 \geq \lambda_2 \geq \cdots \geq \lambda_n \geq 0. \tag{2.2}$$

By construction they represent the most variance with the least number of patterns.

The application of EOF analysis to meteorological variables has usually been done in two-dimensions in such a way that every grid point (station) represent an equal area (Kutzbach 1967, Buell 1978). We are here interested in analyzing data for each zonal Fourier component separately. It so happens that our EOFs are functions of latitude for the shallow water model and are functions of latitude and height for the primitive equations. For simplicity we discuss the two-dimensional case (longitudinal Fourier analysis and latitudinal EOF analysis), although the same argument can be easily generalized for the three-dimensional case.

Consider a zonal Fourier coefficient variable, $\eta(\phi, t)$, which is a function of latitude and time only. Let us assume that the observed data, $\eta(\phi, t)$, can be written as the product of temporal and spatial functions and a remainder as:

$$\eta(\phi, t) = A(t)F(\phi) + r(\phi, t) \tag{2.3}$$

where ϕ is latitude, $r(\phi, t)$ is the remaining (error) term and $A(t)$ and $F(\phi)$ are functions to be determined such that $A(t)F(\phi)$ represents the maximum variance of $\eta(\phi, t)$. Here we try to find $A(t)$ and $F(\phi)$ in such a way that the variance of r is minimum. In other words, $A(t)$ and $F(\phi)$ are varied until the least possible value of $\iint r^2 \cos\phi d\phi dt$ can be found.

For every latitude, ϕ, we require $P(\phi) = \int r^2 dt$ to be minimum and for each time, t, we minimize $Q(t) = \int r^2 cos\phi d\phi$. These lead to

$$\frac{\partial P}{\partial F} = 0 = \int [\eta(\phi, t) - A(t)F(\phi)]\, A(t)dt \tag{2.4}$$

and

$$\frac{\partial Q}{\partial A} = 0 = \int [\eta(\phi, t) - A(t)F(\phi)]\, F(\phi)cos(\phi)d\phi. \tag{2.5}$$

The function $F(\phi)$ is normalized such that:

$$\int F^2 cos(\phi)d\phi = 1. \tag{2.6}$$

From (2.5) we see that $A(t)$ is just the projection of η on $F(\phi)$ (with normalization condition (2.6)). Letting

$$\frac{1}{T}\int A^2(t)dt = \lambda \tag{2.7}$$

be a positive number representing the variance, where T is the time period, (2.4) and (2.5) become:

$$\lambda F(\phi) = \frac{1}{T} \int \eta(\phi, t) A(t) \mathrm{d}t \tag{2.8}$$

and

$$A(t) = \int \eta(\phi, t) F(\phi) cos(\phi) \mathrm{d}\phi. \tag{2.9}$$

Substituting $A(t)$ from equation (2.9) into equation (2.8) we find the integral equation

$$\begin{aligned} \lambda F(\phi) &= \frac{1}{T} \int_t \eta(\phi, t) \left[\int_{\phi'} \eta(\phi', t) F(\phi') cos(\phi') \mathrm{d}\phi' \right] \mathrm{d}t \\ &= \int_{\phi'} \left[\frac{1}{T} \int_t \eta(\phi, t) \eta(\phi', t) \mathrm{d}t \right] F(\phi') cos(\phi') \mathrm{d}\phi' \\ &= \int G(\phi, \phi') F(\phi') cos(\phi') \mathrm{d}\phi', \end{aligned} \tag{2.10}$$

where

$$G(\phi, \phi') = \frac{1}{T} \int \eta(\phi, t) \eta(\phi', t) \mathrm{d}t$$

is the symmetric covariance function of the field between the two points ϕ and ϕ'. The above EOF theory is discussed in the context of continuous space and time. However, in practice $\eta(\phi, t)$ is measured in discrete space (grid points) and time (with a constant time interval). We can express the covariance function, $G(\phi, \phi')$, in matrix form as:

$$\mathbf{G}(\phi_i, \phi_j) = \frac{1}{T} \sum_{k=1}^{T} \eta(\phi_i, t_k) \eta(\phi_j, t_k), \tag{2.11}$$

where T is the number of observations. Since our data are available on a Gaussian grid (see Washington and Parkinson (1986), Appendix B), the spatial integral in (2.10) can be exactly replaced by a summation as follows [see also Buell 1971, 1978 for more discussion of approximating the integral in (2.10) by a finite-dimensional matrix equation]:

$$\lambda \mathbf{F}(\phi_i) = \sum_{j=1}^{M} \mathbf{G}(\phi_i, \phi_j) \mathbf{F}(\phi_j) w(\phi_j), \tag{2.12}$$

where M is the number of Gaussian latitude points and $w(\phi_j)$ is the Gaussian weighting factor. One can refer to Washington and Parkinson (1986) appendix B for the calculation of the Gaussian weighting factor. Equation (2.12) is not in the form of the standard eigenvalue problem, e.g., $[\mathbf{A}]X=\lambda X$. However, we can transform it into the standard form by multiplying (2.12) by $\sqrt{w(\phi_i)}$ and rearranging as:

$$\lambda \mathrm{F}(\phi_i)\sqrt{w(\phi_i)} = \sum_{j=1}^{M} \mathrm{F}(\phi_j)\sqrt{w(\phi_j)}\left[\mathbf{G}(\phi_i,\phi_j)\sqrt{w(\phi_i)w(\phi_j)}\right]$$

or

$$\lambda \tilde{\mathrm{F}}(\phi_i) = \sum_{j=1}^{M} \tilde{\mathbf{G}}(\phi_i,\phi_j)\tilde{\mathrm{F}}(\phi_j), \tag{2.13}$$

where

$$\tilde{\mathbf{G}}(\phi_i,\phi_j) = \mathbf{G}(\phi_i,\phi_j)\sqrt{w(\phi_i)w(\phi_j)} \quad \text{and} \quad \tilde{\mathrm{F}}(\phi_i) = \mathrm{F}(\phi_i)\ \sqrt{w(\phi_i)}.$$

Now (2.13), but not (2.12), is a standard eigenvalue problem and can be readily solved for λ and $F(\phi)$ by standard techniques. Each eigenvalue, λ_n, is associated with an eigenfunction (EOF) $F_n(\phi)$. The larger the value of λ_n, the larger the explained variance. The time series associated with each eigenvector can be calculated from (2.9) or

$$A_n(t) = \sum_{j=1}^{M} \eta(\phi_j,t)\mathrm{F}_n(\phi_j)w(\phi_j) = \sum_{j=1}^{M}\left[\eta(\phi_j,t)\sqrt{w(\phi_j)}\right]\tilde{\mathrm{F}}_n(\phi_j). \tag{2.14}$$

Since the covariance matrix, $\mathbf{C}$, in (2.1) is a real and symmetric matrix (Hermitian), the eigenvalues, λ_i, are real and the eigenvectors are orthogonal to each other. To show this we multiply equation (2.1) by a row vector $X_j^\dagger$ and write another equation by replacing i by j, which yields

$$X_j^\dagger \mathbf{C} X_i = \lambda_i X_j^\dagger X_i \tag{2.15}$$

and

$$X_i^\dagger \mathbf{C} X_j = \lambda_j X_i^\dagger X_j. \tag{2.16}$$

Taking the adjoint of this equation, we have

$$X_j^\dagger C^\dagger X_i = X_j^\dagger C X_i = \lambda_j^* X_j^\dagger X_i, \qquad (2.17)$$

where the asterisk denotes the complex conjugate while the dagger represents the complex conjugate transpose of a matrix. The first equality comes from the fact that **C** is Hermitian. Subtracting equation (2.17) from equation (2.15), we obtain

$$(\lambda_i - \lambda_j^*) X_j^\dagger X_i = 0. \qquad (2.18)$$

First if we let $i = j$ in (2.18) then a nontrivial solution requires the eigenvalue λ_i to be real ($\lambda_i = \lambda_i^*$). Second, for $i \neq j$ and $\lambda_i \neq \lambda_j^*$, we find

$$(\lambda_i - \lambda_j^*) X_j^\dagger X_i = 0. \qquad (2.19)$$

or

$$X_j^\dagger X_i = 0 \qquad (2.20)$$

so that the eigenvectors of distinct eigenvalues are orthogonal. In the case of degeneracy ($\lambda_i = \lambda_j$), the eigenvectors X_i and X_j are not automatically orthogonal: however, they can be made orthogonal by using a well-known method called Gram-Schmidt orthogonalization (see Arfken 1985 section 9.3). We also note that not only are the eigenvectors mutually orthogonal but so are their associated time series, $A_n(t)$ (Kutzbach 1967).

In the above discussion of EOF theory all the eigenvectors are used to represent data without any concern about degenerate multiplets or sampling errors in constructing the covariance matrix. In practice, however, only the first few eigenvectors are used to approximate the physical field. If one's interest is in the structure of the data set itself then the aspect of most concern is the degeneracy of EOFs. In that case, two or more eigenvectors have the same eigenvalue and any linear combination of these eigenvectors is also a solution. Hence the structure of the data set is not unique. Kutzbach has used 25 Januaries of sea-level pressure, surface temperature and precipitation to construct the combination EOFs in which all three variables are used to construct a covariance matrix. He noticed that if only 15 of these 25 Januaries were used, the first three eigenvectors were similar to the previous ones (although the first two reversed in order of importance); the eigenvectors which were associated with smaller eigenvalues had changed significantly. North *et al.* (1982) studied this change in EOFs by perturbing the covariance matrix. In this work, a small symmetric perturbation matrix (sampling errors) was added to the covariance matrix to estimate the shifts in eigenvectors and eigenvalues. According to the results, North *et al.* suggested the the following estimate for sampling errors:

$$\delta\lambda = \lambda\sqrt{\frac{2}{N}}. \qquad (2.21)$$

where N is the sample size and λ is the eigenvalue. If the difference between two neighbouring eigenvalues, $\Delta\lambda$, is less than the sampling error, $\delta\lambda$, then the eigenvector is considered as "effectively degenerate". This EOF will be changed significantly if the sample size is reduced as in Kutzbach's case. Since sampling errors exist in practice, only EOFs which have differences in the spectrum of eigenvalues that are greater than the sampling error are considered to be independent (i.e., do not mix with the neighbouring EOFs).

2.2 ENM Analysis for the Shallow Water Model

Longuet-Higgins (1968) has solved the Laplace tidal equations, also called the linearized shallow-water model equations on a sphere for a basic state at rest, i.e. for $u_o = v_o = \zeta_o = 0$. The solutions to this problem, which are functions of the latitude and longitude are called the Hough functions. Each of the Hough modes has a frequency associated with it. The shallow water model is one of the most used numerical model in both atmosphere and ocean research due to its simplicity. In this section we present the ENM formalism for the shallow water model. The formulae will be later used to analyze the model output and the results will be tested against the analytical solutions provided by Longuet-Higgins.

As mentioned earlier, the ENM analysis method is a technique that finds orthogonal functions of a dynamical variable based on the generalized EP theorem. To find such a variable, we begin with the horizontal momentum and continuity equations on a sphere linearized about a basic state at rest:

$$\frac{\partial u}{\partial t} - fv = -\frac{g}{a\cos\phi}\frac{\partial h}{\partial \lambda} \tag{2.22}$$

$$\frac{\partial v}{\partial t} + fu = -\frac{g}{a}\frac{\partial h}{\partial \phi} \tag{2.23}$$

and

$$\frac{\partial h}{\partial t} + \frac{\mathrm{H}}{a\cos\phi}\left[\frac{\partial u}{\partial \lambda} + \frac{\partial}{\partial \phi}(v\cos\phi)\right] = 0 \tag{2.24}$$

where $f = 2\Omega\sin\phi$ is the Coriolis parameter, Ω is the Earth's rotation rate, H is the constant basic state depth of the fluid, g is the acceleration of gravity, a is the Earth's radius, u, v are the perturbation eastward and northward components of velocity respectively, h is the perturbation height above the equilibrium level, λ is longitude and ϕ is latitude. In the above equations we have assumed that the perturbation height is much less than the mean depth, i.e., $h \ll \mathrm{H}$. The conservation of potential vorticity can be written as (Gill 1982 sections 11.2 and 11.3)

$$\frac{\mathrm{D}q}{\mathrm{D}t} = 0 \tag{2.25}$$

where

$$\frac{\mathrm{D}}{\mathrm{D}t} = \frac{\partial}{\partial t} + \frac{u}{a\cos\phi}\frac{\partial}{\partial \lambda} + \frac{v}{a}\frac{\partial}{\partial \phi} \tag{2.26}$$

and the potential vorticity is

$$q = \frac{f+\zeta}{\mathrm{H}+h} = \frac{1}{\mathrm{H}}\left(f + \zeta - \frac{f}{\mathrm{H}}h\right) + \mathrm{O}(q'^2) \tag{2.27}$$

with ζ being the perturbation relative vorticity and $O(q'^2)$ denotes non-linear terms. Substituting (2.27) into (2.25) and keeping only linear terms we have

$$\frac{\partial q'}{\partial t} + q_{oy}v = 0. \tag{2.28}$$

where the potential vorticity (PV) gradient is

$$q_{oy} = \frac{1}{a}\frac{\partial}{\partial\phi}\left(\frac{f}{\mathrm{H}}\right) = \frac{2\Omega\cos\phi}{a\mathrm{H}} \tag{2.29}$$

and the perturbation potential vorticity is

$$q' = \frac{1}{\mathrm{H}}\left(\zeta - \frac{f}{\mathrm{H}}h\right). \tag{2.30}$$

Multiplying (2.28) by H^2q' and dividing by q_{oy}, the resulting equation is then zonally averaged to obtain

$$\frac{\partial}{\partial t}\left(\frac{\mathrm{H}^2}{2}\frac{\overline{q'^2}}{q_{oy}}\right) + \mathrm{H}^2\overline{vq'} = 0. \tag{2.31}$$

If we multiply (2.22) by h and (2.24) by u, then add the resulting equations, we get

$$\frac{\partial}{\partial t}(uh) + \frac{\mathrm{H}}{a\cos\phi}\left[\frac{\partial}{\partial\lambda}\left(\frac{u^2}{2}\right) + u\frac{\partial}{\partial\phi}(v\cos\phi)\right] - fvh = -\frac{g}{a\cos\phi}\frac{\partial}{\partial\lambda}\left(\frac{h^2}{2}\right). \tag{2.32}$$

Taking the zonal mean of the above equation and using the longitudinal periodicity we have

$$\frac{\partial}{\partial t}(\overline{uh}) + \frac{\mathrm{H}}{a\cos\phi}\overline{u\frac{\partial}{\partial\phi}(v\cos\phi)} - f\overline{vh} = 0, \tag{2.33}$$

where the overbar denotes a zonal mean. Since

$$\zeta = \frac{1}{a\cos\phi}\left[\frac{\partial v}{\partial\lambda} - \frac{\partial}{\partial\phi}(u\cos\phi)\right], \tag{2.34}$$

we can write the second term in (2.31) as

$$\mathrm{H}^2\overline{vq'} = \mathrm{H}\overline{v\zeta} - f\overline{vh} = -\frac{\mathrm{H}}{a\cos\phi}\overline{v\frac{\partial}{\partial\phi}(u\cos\phi)} - f\overline{vh}. \tag{2.35}$$

Substituting (2.35) into (2.31) and subtracting (2.33) we obtain

$$\frac{\partial}{\partial t}\left[\frac{\mathrm{H}^2}{2}\frac{\overline{q'^2}}{q_{oy}} - \overline{uh}\right] = -\frac{\mathrm{H}}{a\cos\phi}\left[\overline{u\frac{\partial}{\partial\phi}(v\cos\phi)} + \overline{v\frac{\partial}{\partial\phi}(u\cos\phi)}\right]. \tag{2.36}$$

The right-hand side of (2.36) can be transformed into a flux divergence form by multiplying by cosϕ which becomes

$$\frac{\partial}{\partial t}\left[\cos\phi\left(\frac{H^2}{2}\frac{\overline{q'^2}}{q_{oy}}-\overline{uh}\right)\right]=-\frac{H}{a\cos\phi}\frac{\partial}{\partial\phi}(\overline{uv}\cos^2\phi). \qquad (2.37)$$

Integrating the above equation from latitude of $-\pi/2$ to $\pi/2$, i.e. $\int_{-\pi/2}^{\pi/2}(\bullet)\cos\phi d\phi$, the right-hand side of (2.37) vanishes, so that we have

$$\frac{\partial}{\partial t}\int_{-\pi/2}^{\pi/2}\left[\cos\phi\left(\frac{H^2}{2}\frac{\overline{q'^2}}{q_{oy}}-\overline{uh}\right)\right]\cos\phi d\phi=0. \qquad (2.38)$$

Therefore for the shallow-water model, the pseudomomentum density, $\mathcal{P}$, is conserved over the domain, where

$$\mathcal{P}=\cos\phi\left(\frac{H^2}{2}\frac{q'^2}{q_{oy}}-uh\right). \qquad (2.39)$$

In order to show the relation between the orthogonality of the wave vector and the wave activity (pseudomomentum), we consider the dynamical equations of the shallow-water model in matrix form (see Held 1985)

$$\mathbf{L}X=c\mathbf{P}X, \qquad (2.40)$$

where **L** and **P** are self-adjoint matrices. The matrix **P** and the wave vector X are defined as

$$\mathbf{P}=\begin{pmatrix}0&\cos\phi&0\\ \cos\phi&0&0\\ 0&0&-\frac{H^2\cos\phi}{q_{oy}}\end{pmatrix} \quad \text{and} \quad X=\begin{pmatrix}u\\ h\\ q'\end{pmatrix}. \qquad (2.41)$$

For the meridional mode n, the (2.40) can be written as

$$\mathbf{L}X_n=c_n\mathbf{P}X_n \qquad (2.42)$$

where

$$X_n(\lambda,\phi,t)=\sum_k X_{kn}(\phi)e^{ik(\lambda-c_{kn}t)} \qquad (2.43)$$

and k is the zonal wave number. From now on we fix our attention on a particular k, so we drop the index k. Since the system is conservative (no energy source or sink), neutral modes are expected, i.e. the phase speeds, c_n, are real. The modal orthogonality can be shown by multiplying (2.42) by $X_m^\dagger$ and taking the adjoint of the resulting equation to obtain

$$X_n^\dagger \mathbf{L}^\dagger X_m = c_n X_n^\dagger \mathbf{P}^\dagger X_m. \tag{2.44}$$

Because $\mathbf{L}$ and $\mathbf{P}$ are self-adjoint matrices, we can write (2.44) as

$$X_n^\dagger \mathbf{L} X_m = c_n X_n^\dagger \mathbf{P} X_m. \tag{2.45}$$

Replacing the index n by m in (2.42), multiplying by $X_n^\dagger$ yields

$$X_n^\dagger \mathbf{L} X_m = c_m X_n^\dagger \mathbf{P} X_m. \tag{2.46}$$

Subtracting (2.46) from (2.45) we obtain the orthogonality condition between modes m and n as

$$(c_n - c_m)\left\langle X_n^\dagger \mathbf{P} X_m \right\rangle = 0, \tag{2.47}$$

where the angle brackets denote the latitudinal integration. From (2.47) we see that if the eigenvalues of two different modes are not equal ($c_n \neq c_m$) then the two modes are orthogonal, with the orthogonality condition being defined by

$$\left\langle X_n^\dagger \mathbf{P} X_m \right\rangle = 0 \qquad \text{if} \qquad n \neq m. \tag{2.48}$$

From the orthogonality in condition (2.48) and the conservation of the pseudomomentum in (2.39), we construct the angular pseudomomentum matrix for each wave number k (Brunet 1994) as

$$\mathbf{M}(\phi, \phi') = \frac{1}{2}\left\{\chi(\phi, t)\chi^\dagger(\phi', t)\right\}\mathbf{P}, \tag{2.49}$$

where the curly brackets denote a time mean and $\chi(\phi, t)$ is the coefficient of $e^{ik\lambda}$, i.e.

$$\chi(\phi, t) = \sum_n X_n(\phi) e^{-ikc_n t}. \tag{2.50}$$

Notice that $\left\{\chi(\phi,t)\chi^{\dagger}(\phi',t)\right\}$ is just the wave vector covariance matrix. If we substitute (2.50) into (2.49) and use the fact that

$$\frac{1}{\mathrm{T}}\int_{0}^{\mathrm{T}} \mathrm{e}^{-ik(c_n-c_m)t}\mathrm{d}t = \delta_{mn}, \tag{2.51}$$

where T is period and δ_{mn} is the Kronecker delta then (2.49) becomes

$$\mathbf{M}(\phi,\phi') = \frac{1}{2}\sum_{m} \mathrm{X}_m(\phi)\mathrm{X}_m^{\dagger}(\phi')\mathbf{P}. \tag{2.52}$$

If we rewrite, without loss of generality, (2.48) as:

$$\frac{1}{2}\left\langle \mathrm{X}_n^{\dagger}\mathbf{P}\mathrm{X}_m\right\rangle = \lambda_n\delta_{mn}, \tag{2.53}$$

then X_n is the eigenvector of $\mathbf{M}$ with eigenvalue, λ_n, because,

$$\begin{aligned}(\mathbf{M}(\phi,\phi')\mathrm{X}_n(\phi'))_{\phi'} &= \sum_{m} \mathrm{X}_m(\phi)\frac{1}{2}\left\langle \mathrm{X}_m^{\dagger}(\phi')\mathbf{P}\mathrm{X}_n(\phi')\right\rangle_{\phi'} \\ &= \lambda_n\mathrm{X}_n(\phi)\end{aligned} \tag{2.54}$$

where the subscript ϕ' outside the angle brackets denote the dummy variable of integration. Notice that the pseudomomentum matrix, $\mathbf{M}$, defined in (2.49) has a conserved norm (trace of the matrix) which is the pseudomomentum defined in (2.39).

We can write the shallow water model in a zonally-averaged conservation form of the generalized EP theorem in (1.36) where the gradient in polar coordinate is

$$\nabla = \frac{1}{a\cos\phi}\frac{\partial\cos\phi}{\partial\phi}, \tag{2.55}$$

the wave activity density, $\mathcal{A}$, is

$$\mathcal{A} = \cos\phi\left(\frac{\mathrm{H}}{2}\frac{\overline{q'}^2}{q_{oy}} - \overline{uh}\right) \tag{2.56}$$

and the EP flux, $\mathbf{F} = F^{(\phi)}$ is

$$F^{(\phi)} = \mathrm{H}\cos\phi\overline{uv}. \tag{2.57}$$

2.3 ENM Analysis Based on the Primitive Equations

The shallow water (one-layer) model used in the previous section is a convenient framework to study the barotropic (or extended) modes of oscillation in the atmosphere and oceans. To apply the model to the analysis of internal modes of oscillation with that framework one would have to assign the depth of the fluid to correspond to the equivalent depths of the internal modes, one mode at a time. As the equivalent depths of the various internal modes are not known a priori, the choice of the equivalent depths is arbitrary.

To analyze atmospheric oscillations it is much preperable to use the framework of a baroclinic (3-D) model. In this section, we use the wave activity conservation for the 3D primitive equations shown in Appendix A, which is similar to Andrews' (1987) work, to derive the ENM framework based on the conserved norm of the wave vector (wave activity). The technique will be used to analyze stratospheric data and selected datasets for warming events.

Similar to the previous section, we can construct the pseudomomentum matrix, **M**, for a particular zonal wave number which is based on the conservation of wave activity, $\mathcal{A}$, in equation (A.35) as

$$\mathbf{M}(\phi, z; \phi', z') = \frac{1}{2}\left\{\chi(\phi, z, t)\chi^{\dagger}(\phi', z', t)\right\}\mathbf{P} \qquad (2.58)$$

where the curly brackets denote a time average, $\chi(\phi, z, t)$ is the zonal Fourier coefficient of the wave vector, e.g., $\mathrm{X}(\lambda, \phi, z, t) = \chi(\phi, z, t)e^{ik\lambda}$ [see also (2.50)], the wave vector X and the matrix **P** are defined as

$$\mathrm{X} = \begin{bmatrix} \Pi' \\ \theta' \\ u'_z \end{bmatrix} \quad \text{and} \quad \mathbf{P} = a\rho\cos\phi \begin{bmatrix} \frac{\rho}{\mathrm{J}} & 0 & 0 \\ 0 & \frac{\rho}{\overline{\theta}_z^2}\left(\frac{\overline{u}_z}{\rho}\right)_z & -\frac{1}{\theta_z} \\ 0 & -\frac{1}{\theta_z} & 0 \end{bmatrix}. \tag{2.59}$$

By solving the eigenvalue problem

$$\mathbf{M}\mathrm{X}_n = \lambda_n \mathrm{X}_n \tag{2.60}$$

we obtain the ENM, X_n, and eigenvalue, λ_n [see also (2.54)]. Once again, the trace of the pseudomomentum matrix, **M**, defined in (2.58) is the conserved wave activity.

Notice that the reference basic states for the shallow water model (section 2.2) and the primitive equations are at rest and zonally symmetric, respectively. The choice of the basic state is otherwise not subject to any constraint. We require that the basic state be zonally symmetric to allow for a separation of the sine and cosine dependence in longitude. Zonally-varying basic states generally do not allow perturbations that can be expressed as a single zonal harmonic, but rather allow the propagation of modes that need to be expressed as a sum of zonal harmonics, a complication that we want to avoid in this study.

Chapter 3

Application of ENM Analysis to the Shallow Water Model

In this chapter the ENM analysis technique is used to analyze the output of a shallow water model integration. We have chosen the shallow water model in this study because the exact solutions to the problem are known so that comparisons of the exact meridional structures (Hough modes) and their frequencies to those of the ENM analysis results can be made. We want to see how well the ENM analysis can recover the known properties of the Hough modes (solutions of the linearized shallow water model equations) by applying this method to the output of a shallow water model integration.

We will discuss the model equations in section 3.1. Section 3.2 shows how the model output is generated. The methodology of the ENM analysis is found in section 3.3. The results of the ENM analysis are discussed in section 3.4.

3.1 Shallow-Water Model Equations

The non-linear shallow water model used in this study has the following momentum and mass continuity equations:

$$u_t + \frac{1}{a\cos\phi}\left[\frac{1}{2}u^2 + \frac{1}{2}v^2 + g(H + h + h_m)\right]_\lambda - vq = X, \tag{3.1}$$

$$v_t + \frac{1}{a\cos\phi}\left[\frac{1}{2}u^2 + \frac{1}{2}v^2 + g(H + h + h_m)\right]_\phi + uq = Y \tag{3.2}$$

and

$$h_t = \frac{1}{a\cos\phi}[(H + h)u]_\lambda + [(H + h)v]_\phi = -\frac{h}{\tau_r} + Z \tag{3.3}$$

where the absolute vorticity, q, is defined in (2.27), X, Y and Z are components of the friction force per unit of mass, g is the acceleration of gravity, h_m is the mountain height, $u = u_o + u'$ and $v = v_o + v'$ are horizontal velocity components in the eastward (λ) and northward (ϕ) directions, respectively, and τ_r is a damping time relaxation constant. Notice that H is the mean depth of the fluid layer in the 2-dimensional case (shallow water model) and the equivalent depth in the case of 3-dimensional primitive equations.

The model equations described here are similar to (2.22)-(2.24) in section 2.2 if the model is kept in the linear regime. By this we mean that the perturbation height (h) is much smaller than the mean depth (H) in which case the non-linear terms e.g., u'^2, v'^2 etc. are much smaller than linear terms e.g., fu', fv' etc. and are negligible.

3.2 Model data

In order to generate data for the ENM analysis we use a hemispherical shallow water spectral model with a T42 truncation. The model has been initialized with a basic state at rest. To keep the model in the linear regime we excite the flow by a small amplitude Gaussian-like mountain which has a half width of 2000 km. The mountain height, h_m, in (3.1)-(3.3) has the form

$$h_m(\lambda,\phi,t) = h_o \exp\left[-\frac{1}{2}\frac{(t-t_e)^2}{t_c^2}\right] \exp\left[-\frac{1}{2}\frac{(\phi-\phi_o)^2}{\phi_c^2} - \frac{1}{2}\frac{(\lambda-\lambda_e)^2}{\lambda_c^2}\right] \qquad (3.4)$$

where h_o is the mountain height amplitude, t_c, ϕ_c, λ_c are constants that provide the time and space scales of the height disturbance forcing, t_e, ϕ_o, λ_e are positions in time and space of the mountain centre.

We perform two experiments with mean depths of 0.88 km and 8.8 km, which correspond to the dimensionless parameter, $\epsilon = 100$ and 10, respectively [as in Longuet-Higgins (1968)], where ϵ is defined as

$$\epsilon = \frac{4\Omega^2 a^2}{gh}. \qquad (3.5)$$

The maximum amplitude of the mountain, h_o, is set to 1% of the mean depth, the latitudinal centre of the mountain is fixed at 45°N and the time constant, t_c, is one day. The relaxation time, τ_r, in equation (3.3) is equal to four weeks. Since the model has friction and relaxation terms, the wave amplitude will tend to decrease with time, so we use the growth-decay Gaussian-like mountain to randomly (in time, t_e, and longitude, λ_e) excite the model every 25 days on average. The main reason for choosing the above mean depths is that the calculated frequency (or phase speed) corresponding to each normal mode (ENM) can be exactly compared to Longuet-Higgins' Table 5. Each experiment has been integrated for 2000 days with a daily output of u, v and h. This model is the same as that used in Brunet and Vautard (1995).

3.3 Methodology

We now describe how to calculate the ENMs and their associated phase speeds for each wavenumber. We use the model output u, v and h to calculate the potential vorticity, q', according to (2.27). The wave vector, X, which contains 3 fields (u, h, q') is formed using (2.11). The wave vector is then zonally Fourier transformed into sine and cosine components. For each sine and cosine component of a particular wave number, k, we separately construct the pseudomomentum matrix, $\mathbf{M}^k_{s,c}$, as shown in (2.49) or

$$\mathbf{M}^k_{s,c}(\phi, \phi') = \frac{1}{2}\left\{X^k_{s,c}(\phi, t)X^{\dagger k}_{s,c}(\phi', t)\right\}\mathbf{P} \qquad (3.6)$$

where

$$X^k(\lambda, \phi, t) = X^k_s(\phi, t)\sin k\lambda + X^k_c(\phi, t)\cos k\lambda \qquad (3.7)$$

and the matrix, **P** is defined in (2.41). Notice that in constructing the pseudomomentum we have used the Gaussian weighting factor which was discussed in the paragraph following (2.11). For each pseudomomentum matrix, we solve the eigenvalue problem using (2.54) to obtain eigenvectors or ENMs, $\mathrm{X}_n(\phi)$, and eigenvalues, λ_n. Each eigenvalue, λ_n, associated with eigenvector, $\mathrm{X}_n(\phi)$, explains a portion of the variance in the dataset.

There is another conserved quantity (wave activity) called the pseudoenergy. To show this conservation we multiply (2.22) by $\mathrm{H}u$, (2.23) by $\mathrm{H}v$, (2.24) by gh and add the resultant equations to obtain

$$\frac{\partial}{\partial t}\left[\frac{1}{2}\mathrm{H}(u^2 + v^2) + \frac{1}{2}gh^2\right] = -\frac{g\mathrm{H}}{a\cos\phi}\left[\frac{\partial}{\partial\lambda}(uh) + \frac{\partial}{\partial\phi}(\cos\phi vh)\right]. \qquad (3.8)$$

We can write the above equation into the generalized EP theorem as in (1.36) with the new definition of the pseudoenergy, $\mathcal{A}$, as

$$\mathcal{A} = \frac{1}{2}\mathrm{H}(u^2 + v^2) + \frac{1}{2}gh^2 \tag{3.9}$$

and the new flux, $\mathbf{F}=(F^{(\mathcal{A})}, F^{(\phi)})$, is

$$\mathbf{F} = g\mathrm{H}(uh, vh). \tag{3.10}$$

With the above new definitions of $\mathcal{A}$ and $\mathbf{F}$, we have the new matrix $\mathbf{Q}$ and wave vector Y as [see also (2.41)]

$$\mathbf{Q} = \begin{pmatrix} \mathrm{H} & 0 & 0 \\ 0 & \mathrm{H} & 0 \\ 0 & 0 & g \end{pmatrix} \quad \text{and} \quad \mathrm{Y} = \begin{pmatrix} u \\ v \\ h \end{pmatrix}. \tag{3.11}$$

Following the same procedure as in section 2.2 we construct the pseudoenergy matrix, $\mathbf{E}$, as

$$\mathbf{E}(\phi, \phi') = \frac{1}{2}\sum_m \mathrm{Y}_m(\phi)\mathrm{Y}_m^\dagger(\phi')\mathbf{Q}. \tag{3.12}$$

We then solve the eigenvalue problem, $\mathbf{E}\mathrm{Y}_n=\lambda_n\mathrm{Y}_n$, to find the eigenvectors, Y_n.

The main purpose of the introduction of the pseudoenergy concept is to be able to use the modal pseudoenergy and pseudomomentum together in order to calculate the phase speed (or frequency). For each mode, the phase speed is computed from the ratio of modal pseudoenergy and pseudomomentum (see Held 1985 and Brunet 1994) as

$$c_n = \frac{\left\langle \mathrm{Y}_n^\dagger \mathbf{Q} \mathrm{Y}_n \right\rangle}{\left\langle \mathrm{X}_n^\dagger \mathbf{P} \mathrm{X}_n \right\rangle} \tag{3.13}$$

where the angle brackets denote spatial integration. This phase speed calculation is called the "theoretical" method. An alternative way to calculate the phase speed is to use time power spectrum analysis to analyze the time series associated with each

ENM. Similar to EOFs, ENMs are orthogonal to each other and form a complete set. We can expand the zonal Fourier coefficient of the wave vector, $\chi(\phi, t)$ as

$$\chi(\phi, t) = \sum_n a_n(t) \mathrm{X}_n(\phi). \tag{3.14}$$

By using the orthogonality condition in (2.48) we obtain the time coefficient, $a_n(t)$, by projecting data onto that particular ENM such as [see also Brunet 1994]

$$a_n(t) = \frac{\left\langle \mathrm{X}_n^\dagger(\phi) \mathbf{P} \chi(\phi, t) \right\rangle}{\left\langle \mathrm{X}_n^\dagger(\phi) \mathbf{P} \mathrm{X}_n(\phi) \right\rangle}. \tag{3.15}$$

The time series, $a_n(t)$, is then transformed into frequency space. The relation between frequency and phase speed of a wave number, k, is

$$c_n = \frac{\omega_n}{k}. \tag{3.16}$$

For more details about power spectrum analysis one can refer to Press *et al.* (1986), Chapter 12.

3.4 The Results of the ENM Analysis

In this section we present the results of the ENM analysis on the shallow water model data set mentioned in the previous section. The results of the numerical solutions to the Laplace tidal equations presented by Longuet-Higgins (1968) (hereafter LH) are represented in terms of spherical harmonics and known as the normal modes or Hough modes of the tidal equations.

First we present the results of the numerical eigenvalue analysis of the linearized shallow water model equations for a basic state at rest performed by LH. Part of the results are utilized for comparison with the our ENM analyses. Figures 3.1 and 3.2 show the non-dimensional eigenfrequencies ($\omega/2\Omega$) vs. the dimensionless parameter

$\gamma = \epsilon^{-\frac{1}{2}} = \sqrt{gH}/2a\Omega$ of zonal wave numbers 1 and 2, respectively. There are two groups of eigenfrequencies in each figure. The higher frequency (upper) group is associated with gravity waves while the lower frequency (lower) group is associated with Rossby or planetary waves. These figures are used to find the frequency, ω, corresponding to a specific mean depth. In our case, the mean depths are 0.88 and 8.8 km which correspond to $\gamma = 1/10$ and $\gamma = 1/\sqrt{10} = 0.316$, respectively. Figures 3.3 and 3.4 show the exact eigenfunctions or north-south (latitudinal) structures of the perturbation height for different values of mean depth or ϵ. These figures use colatitude (90° minus latitude) as a coordinate. The equator is at the bottom of the graph (90° of colatitude) and the north pole is at the top (0° of colatitude).

Second we present the results from the ENM analysis of our 2000-day integration data sets with two different mean depths of 0.88 and 8.8 km. Since we perform the ENM analysis on each sine and cosine zonal Fourier coefficients separately, the north-south structures (eigenfunctions) of perturbation height of the sine wave (dashed line) and the cosine wave (solid line) are shown separately in Figs. 3.5–3.12. Figure 3.5a shows the first normal mode (ENM1) of the perturbation height for wave number 1 with mean depth of 0.88 km from the ENM analysis. The structure is similar to that of Fig. 3.3a above LH with parameter $\epsilon = 10^2$. Both figures have a broad peak centred around 43°, a smaller one in the vicinity of 13° and a zero near 21° of latitude. When the ENM1 and the exact solution (LH) are compared, it is found that both approach the north pole and the equator in the same way. Similarly, Fig. 3.5b represents the second normal mode (ENM2) structure which is also like the $\epsilon = 10^2$ curve of Fig. 3.3b (LH). Both curves have a broad peak in the neighbourhood of 25° of latitude and approach the pole and the equator in the same manner.

The time series associated with the each ENM that is calculated from (3.15) was analyzed using the Maximum Entropy Method (Press *et al.*, section 13.7) to find the frequency or the phase speed of the structure. Figure 3.6a represents the power spectrum of the ENM1 in Fig. 3.5a. The figure shows the main power is spread from the periods of 20 to 50 days and peaks around the period of 32.8 days. We find the LH non-dimensional frequency in Fig. 3.1 of the structure (n′-s=3, which denotes number of zeros or nodes between the South pole to North pole) with $\gamma=1/10$ is -0.0153 which corresponds to a period of 32.6 days. Similarly, the period of ENM2 for wave number 1 can be found from the power spectrum curve in Fig. 3.6b. This figure has a narrow peak centred at a period of 14.9 days. The corresponding period found in Fig. 3.1 (LH) for the structure (n′-s=1) is 15.1 days. The broad power spectrum of ENM1 in Fig. 3.6a could come from the interference between the traveling wave of period 32.6 days and the mountain "wave" which centres at 45° and has an average period of 25 days. This broad spectrum is not found on other structures which have periods significantly different from the mountain forcing period.

The first two eigenfunctions for wave number 2 with the same above mentioned mean depths are presented in Fig. 3.7a and b. The ENM1 curve in Fig. 3.7a is analogous to the curve labeled $\epsilon = 10^2$ in Fig. 3.4a (LH). The large peak appears at approximately 42.5° of latitude in both curves. the smaller peak is found in the vicinity of 12.5° of latitude and the zero is located around 21° of latitude. The shapes of these curves are observed to be identical when they approach to the north pole and the equator. The period of the above ENM1 is found from a sharp spike in Fig. 3.8a to be 17.5 days. The same period is retrieved from the LH Fig. 3.2. The peak of the ENM2 mode in Fig. 3.7b is located at the same latitude (around 25°) as that of the LH $\epsilon = 10^2$ curve in Fig. 3.3b. However, as the ENM2 curve approaches the pole it tends to zero faster than the LH curve. The period of this ENM is found from the sharp spike in Fig. 3.8b to be 8.3 days, in good agreement with the 8.4 day period in Fig. 3.2 (LH).

We now discuss the results of the ENM analysis on the 2000-day integration data set for the mean depth of 8.8 km or $\epsilon = 10$ or $\gamma = 1/\sqrt{10} = 0.316$. Figure 3.9a displays the ENM1 of wave number 1. This curve has a broad maximum around 64°, one smaller amplitude peak in the vicinity of 20° and a zero in the proximity of 32° of latitude. The same features are found in curve $\epsilon = 10$ of Fig. 3.3a (LH). The two curves act in the same fashion when they approach the north pole and the equator. The ENM2 in Fig. 3.9b has only one peak at around 45° of latitude and monotonically approaches to the north pole. These features are also discovered in Fig. 3.3b (LH). Sharp spikes in the power spectra are exhibited in Figs. 3.10a and b with periods of 12.6 and 5.2 days for ENM1 and ENM2, respectively. The periods retrieved from curves (n'-s=3) and (n'-s=1) in Fig. 3.1 (LH), which correspond to the ENM1 and ENM2, are 12.6 and 5.3 days. Similarly, the structures of ENM1 and ENM2 for wave number 2 are shown in Figs. 3.11a and b. The ENM1 structure in Fig. 3.11a is similar to the LH $\epsilon = 10$ curve in Fig. 3.4a. These two curves have a large peak near 55° of latitude, a small amplitude peak near 20° and a zero at 30° of latitude. Further, they behave exactly the same when approaching the north pole and the equator. Unlike the ENM2 of wave number 1 with mean depth of 0.88 km in Fig. 3.7b which differs from LH's curve when approaching the north pole, the ENM2 of wave number 2 with mean depth of 8.8 km in Fig. 3.11b resembles the curve $\epsilon = 10$ in Fig. 3.4b (LH). However, this ENM2 does not match well the LH structure in the equatorial region. The periods of the ENM1 and ENM2 in Figs. 3.12a and b are found to be 8.6 and 3.8 days which are identical to LH's periods in Fig. 3.2.

The eigenvalues corresponding to the ENMs and their sampling errors which were discussed at the end of section 2.1 are shown in Fig. 3.13. For the case with a mean depth of 0.88 km, the variances explained by the ENM1 and ENM2 for wave number 1 are found to be 53% and 36% of the total variance. For wave number 2, the eigenvalues (in percentage of the total variance of that wave number) for ENM1 and ENM2 are 74% and 14%, respectively. In the case of the 8.8 km mean depth, the eigenvalues of ENM1 and ENM2 for wave number 1 are 58% and 33%, respectively.

Similarly, the wave number 2 eigenvalues for ENM1 and ENM2 are 96% and 3%. In all cases, the first two ENMs of each zonal wave number can explain more than 88% of the total variance. This means that the model has generated only a few important normal modes at zonal wave numbers 1 and 2 in the data set. For wave number 2, the explained variance is concentrated at the ENM1 for both mean depths. The sampling errors (vertical bars) found in this figure are much less than the separations between eigenvalues for each wave number so that the ENMs are considered to be independent.

From the definition of the wave vector in (2.41), when performing the ENM analysis on the data set, we also obtain the meridional structures for zonal wind, u. These zonal wind structures were also examined (but not shown in the thesis) and compared to the LH eigenfunctions. The agreement between the exact solutions and ENMs for zonal wind are as good as in the perturbation height case which are shown in this section.

We also performed an ENM analysis on 100-day data sets (subsets of the above discussed 2000-day data sets) to test the sensitivity of the ENM analysis technique to the length of the record. In the case with a mean depth of 0.88 km, the structures of 100-day (not shown) and 2000-day data sets are comparable. However, in the case of the 8.8 km mean depth, the structures are different, e.g., the small peak [see also Fig. 3.9a] near the equator for the structure of ENM1 from the 100-day data set for wave number 1 is larger than in the 2000-day data set and the zero is shifted northward by as much as 10 degrees of latitude.

The phase speeds of normal modes were also calculated from the ratio of the modal pseudoenergy to pseudomomentum as shown in (3.13). The period is then calculated with (3.16). Periods calculated by this technique agree well with the power spectrum analysis as seen in Table 3.1 and 3.2. The Tables give the time periods which are averaged from the periods of the sine and cosine components for the mean depths of 0.88 km and 8.8 km, respectively. The column labeled "LH" contains periods from Longuet-Higgins (1968). The column marked "Structure" denotes the periods associated with each ENM calculated from the ratio of the modal pseudoenergy to pseudomomentum as in (3.13). The "Power Spectrum" column gives periods from the power spectrum peaks calculated from time series analysis. The "Eigenvalue %" column exhibits the percentage of the total variance for the specific wave number. The values of 2000 d and 100 d represent the length of the time series. The average errors of 2000 and 100 days time series for the mean depth of 0.88 km (Table 1) are 0.58% and 3.72%, respectively. For the 8.8 km case (Table 2), these average errors are 1.46% (2000 days) and 5.4% (100 days).

The above discussion of the ENM analysis on linearized shallow water model data sets leads us to the following observations:

(a) The ENM analysis technique is capable of capturing both structures and time periods, especially with long temporal records (2000 days in our cases) with a high degree of accuracy.

(b) The model generates data which contain monochromatic frequency normal modes. This is supported by sharp spikes in the power spectra in most cases except for the ENM1 of wave number 1 with mean depth of 0.88 km, which is believed to be interfered by the mountain "wave".

(c) As might have been expected the quality of the ENM analysis results degrades as the record length is shortened. The results have shown that the average error of the 100 day time series period is about 4 times as much as for the 2000 days time series.

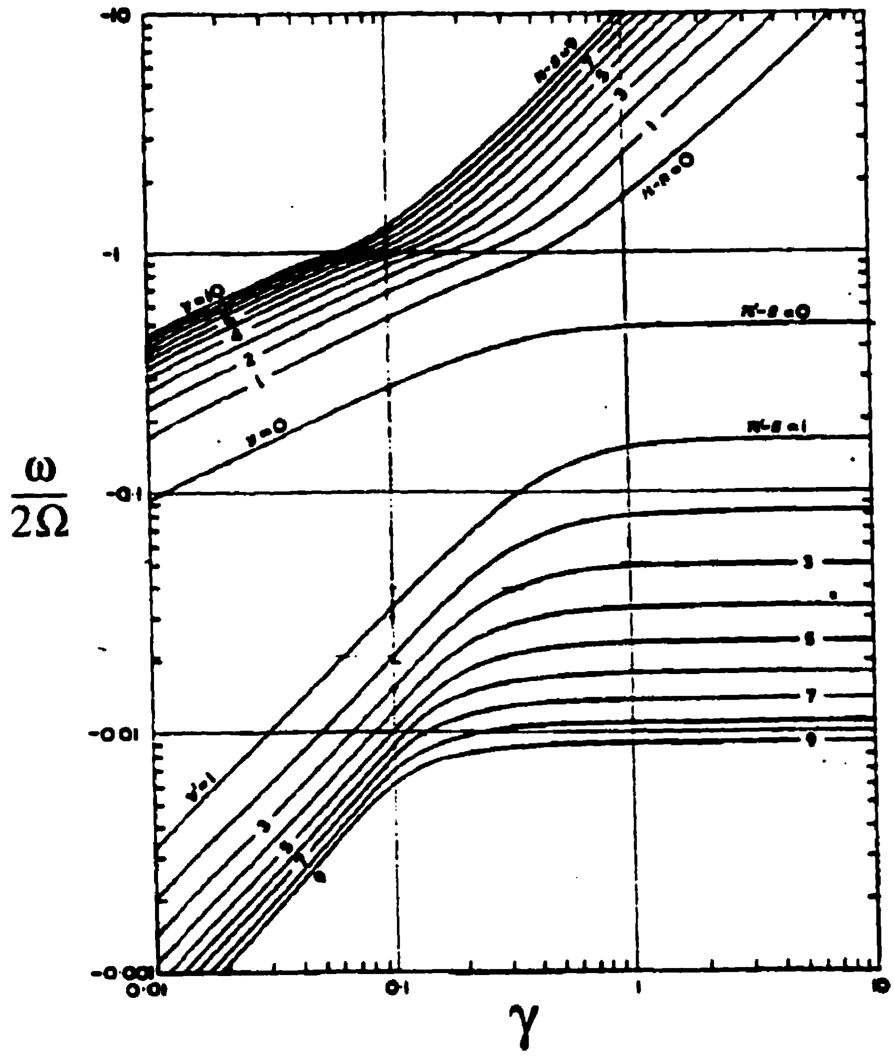

Figure 3.1: The eigenfrequencies of wave number 1 [from Longuet-Higgins].

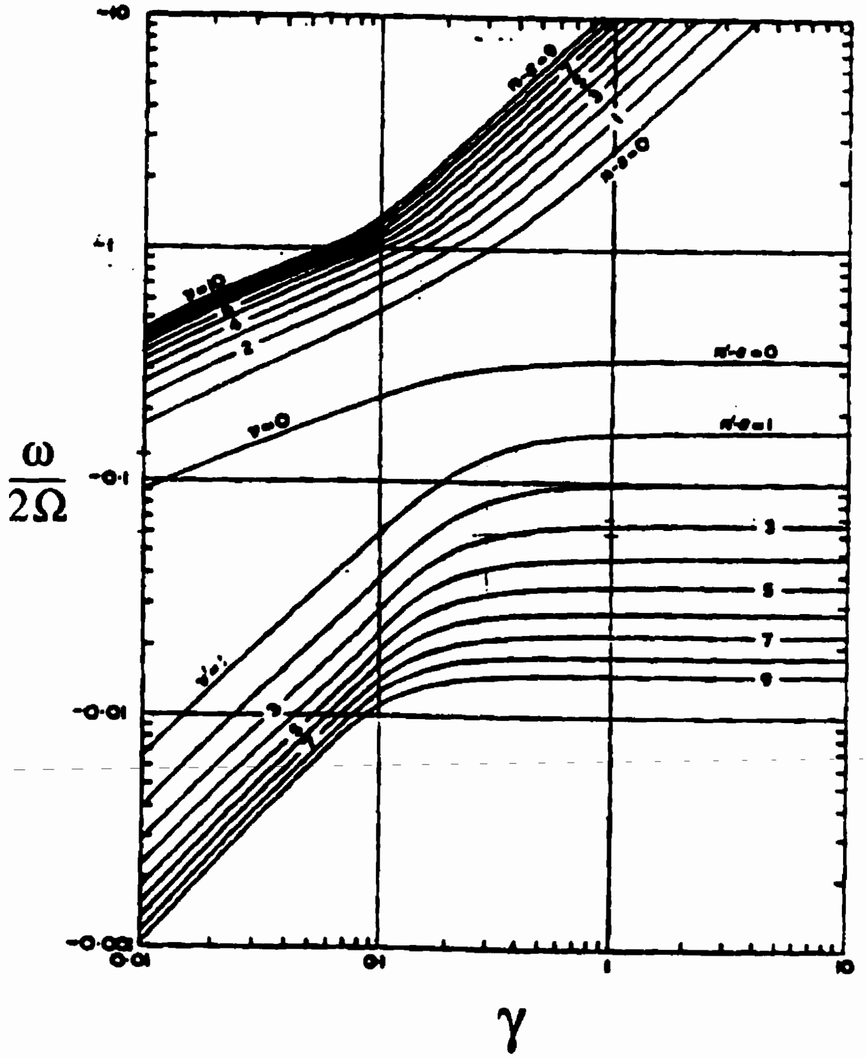

Figure 3.2: The eigenfrequencies of wave number 2 [from Longuet-Higgins].

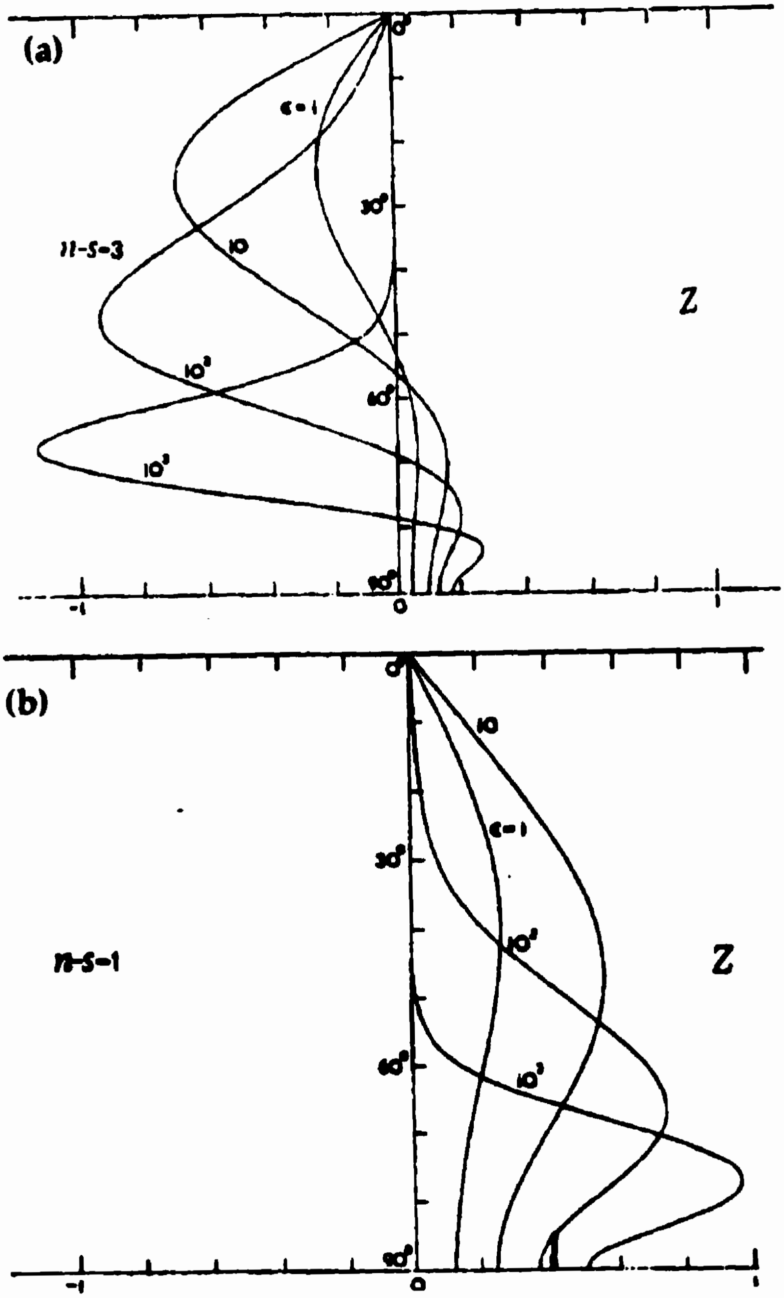

Figure 3.3: The eigenfunctions of height (**a**) n-s=3 and (**b**) n-s=1 of wave number 1 [from Longuet-Higgins].

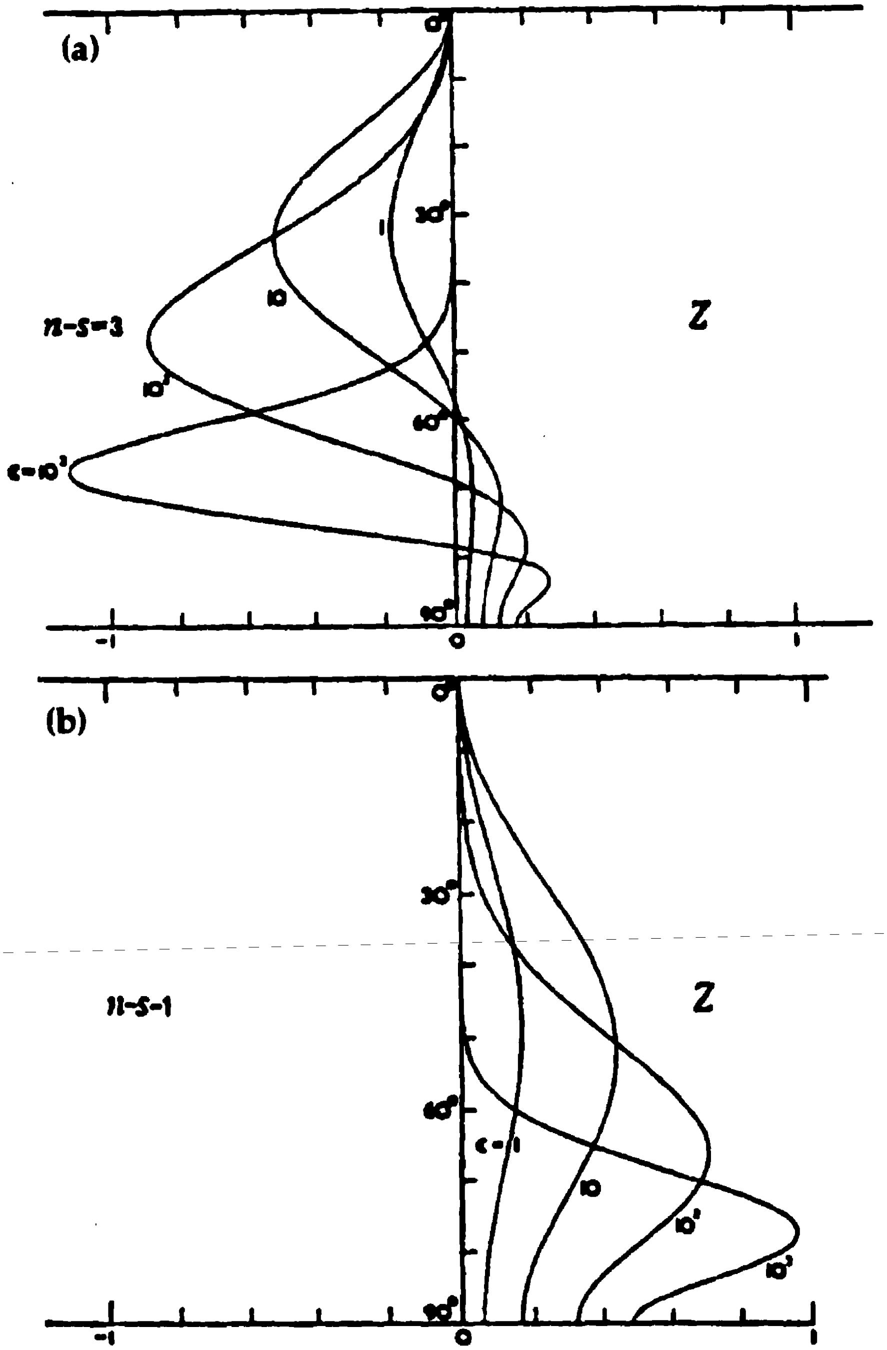

Figure 3.4: The eigenfunctions of height (**a**) n-s=3 and (**b**) n-s=1 of wave number 2 [from Longuet-Higgins].

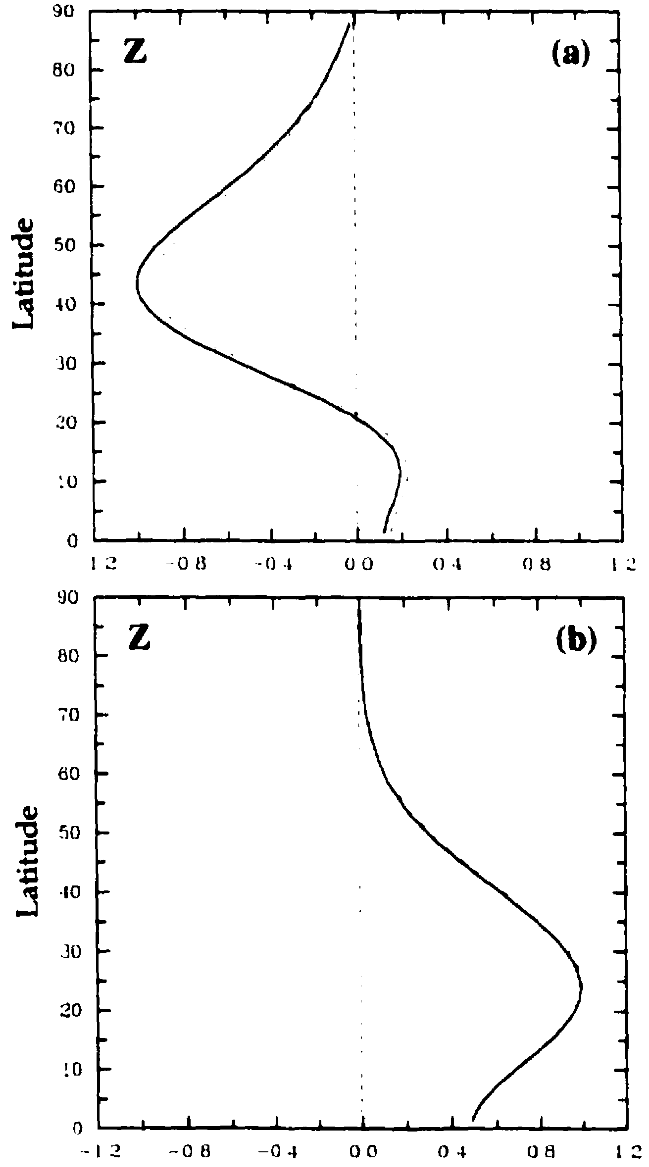

Figure 3.5: **(a)** The first ENM and **(b)** the second ENM of wave number 1 height with mean depth H=0.88 km ($\epsilon = 100$) for 2000-day integration. Cosine is solid and sine is dashed.

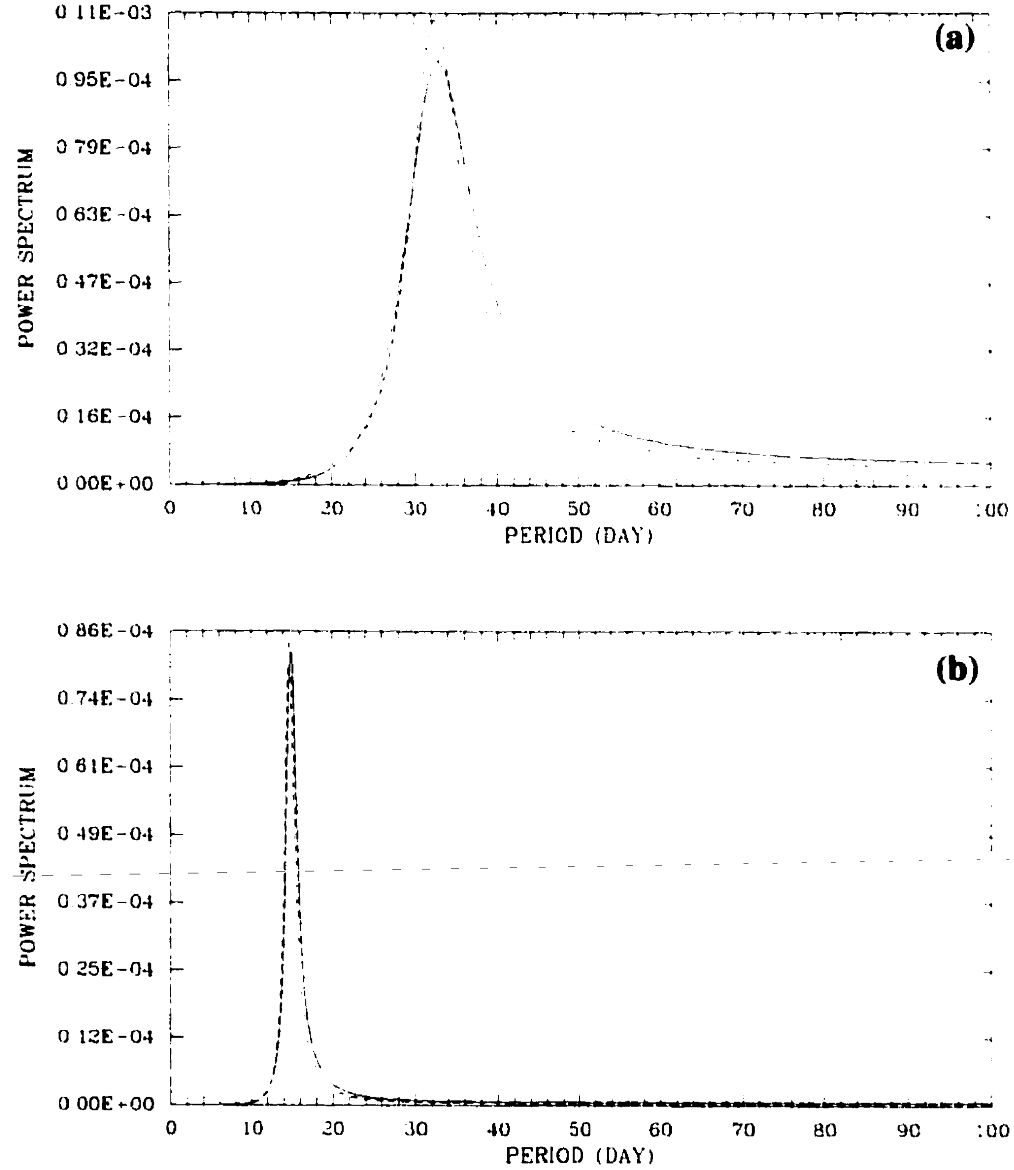

Figure 3.6: **(a)** The first ENM and **(b)** the second ENM power spectra of wave number 1 with mean depth H=0.88 km ($\epsilon = 100$) for 2000-day integration. Cosine is solid and sine is dashed.

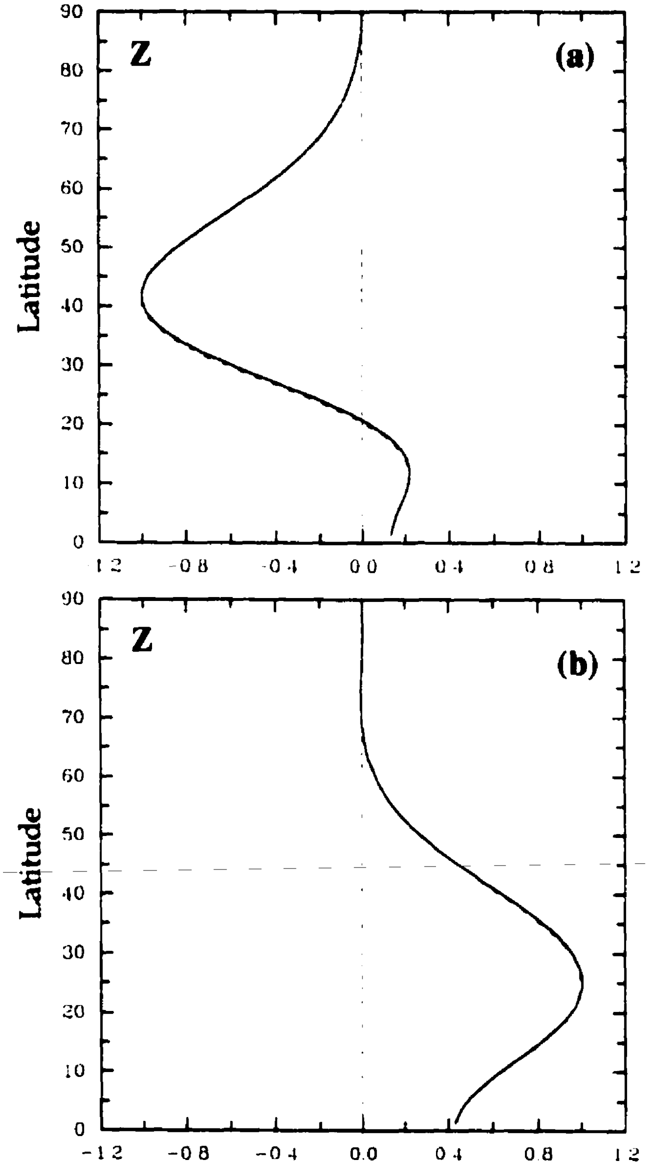

Figure 3.7: (**a**) The first ENM and (**b**) the second ENM of wave number 2 height with mean depth H=0.88 km ($\epsilon = 100$) for 2000-day integration. Cosine is solid and sine is dashed.

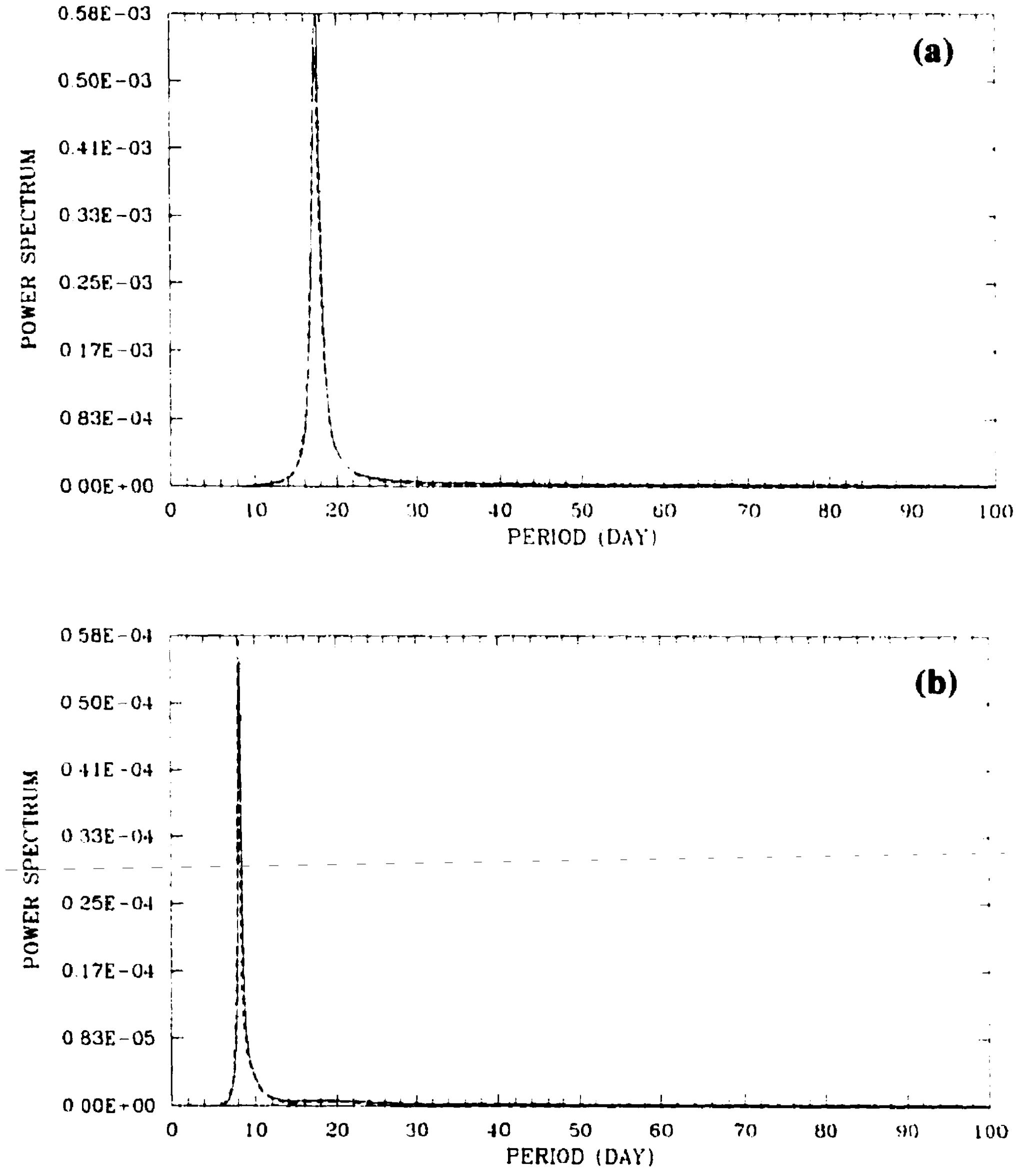

Figure 3.8: **(a)** The first ENM and **(b)** the second ENM power spectra of wave number 2 with mean depth H=0.88 km ($\epsilon = 100$) for 2000-day integration. Cosine is solid and sine is dashed.

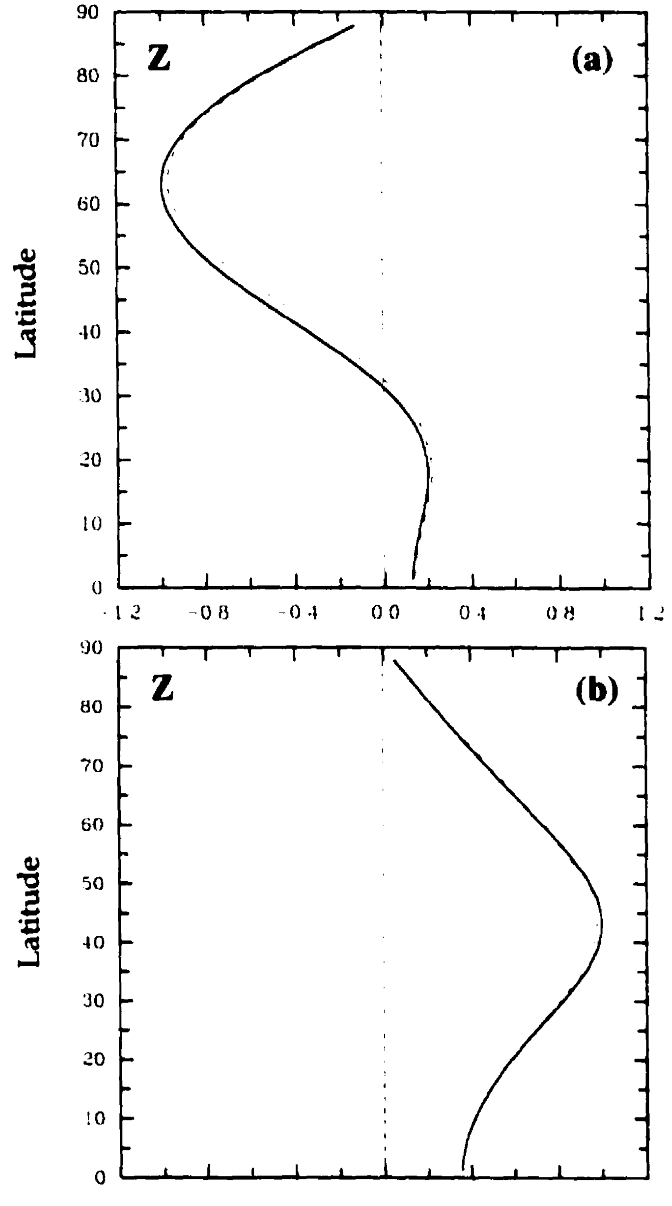

Figure 3.9: **(a)** The first ENM and **(b)** the second ENM of wave number 1 height with mean depth H=8.8 km ($\epsilon = 10$) for 2000-day integration. Cosine is solid and sine is dashed.

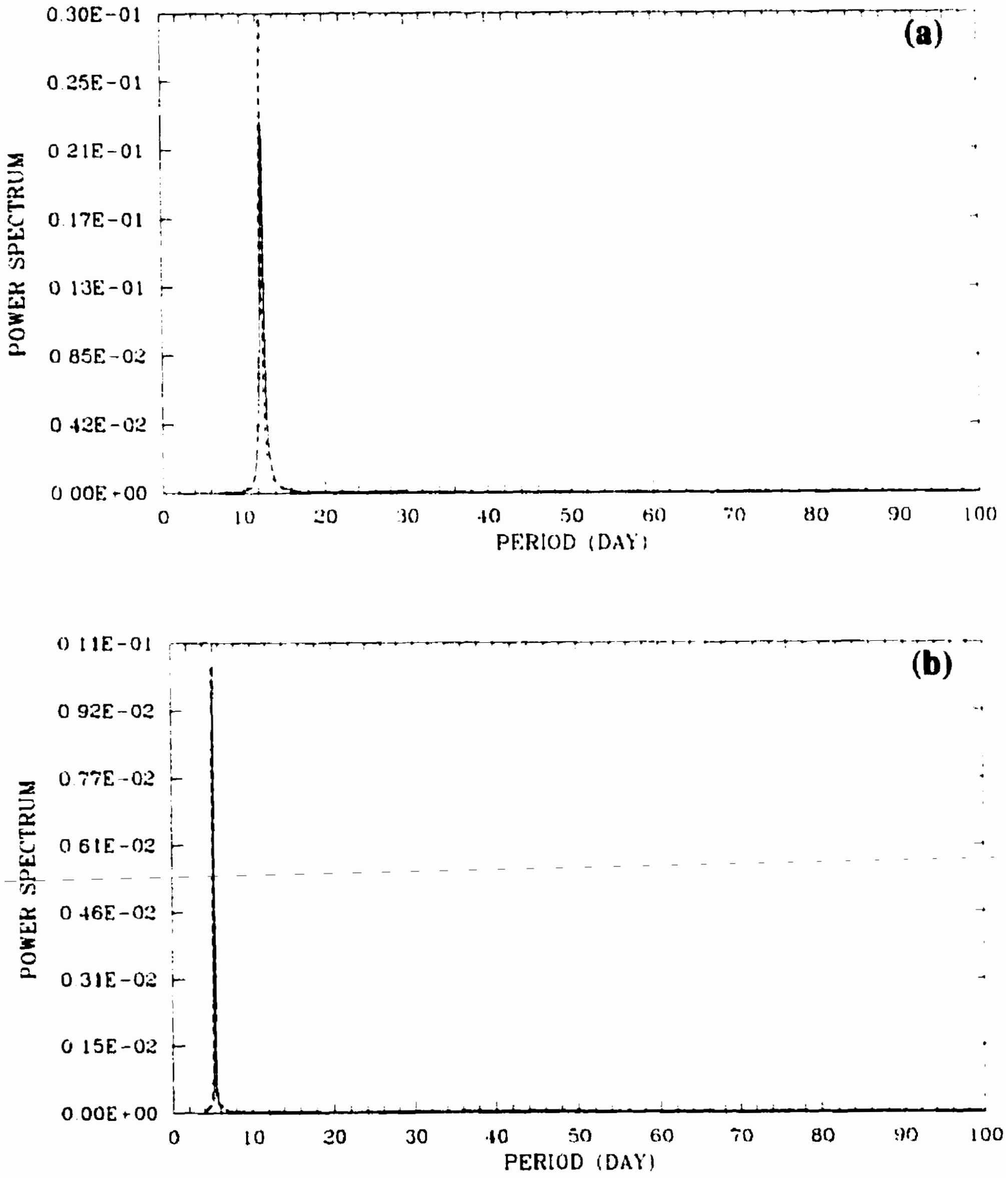

Figure 3.10: **(a)** The first ENM and **(b)** the second ENM power spectra of wave number 1 with mean depth H=8.8 km ($\epsilon = 10$) for 2000-day integration. Cosine is solid and sine is dashed.

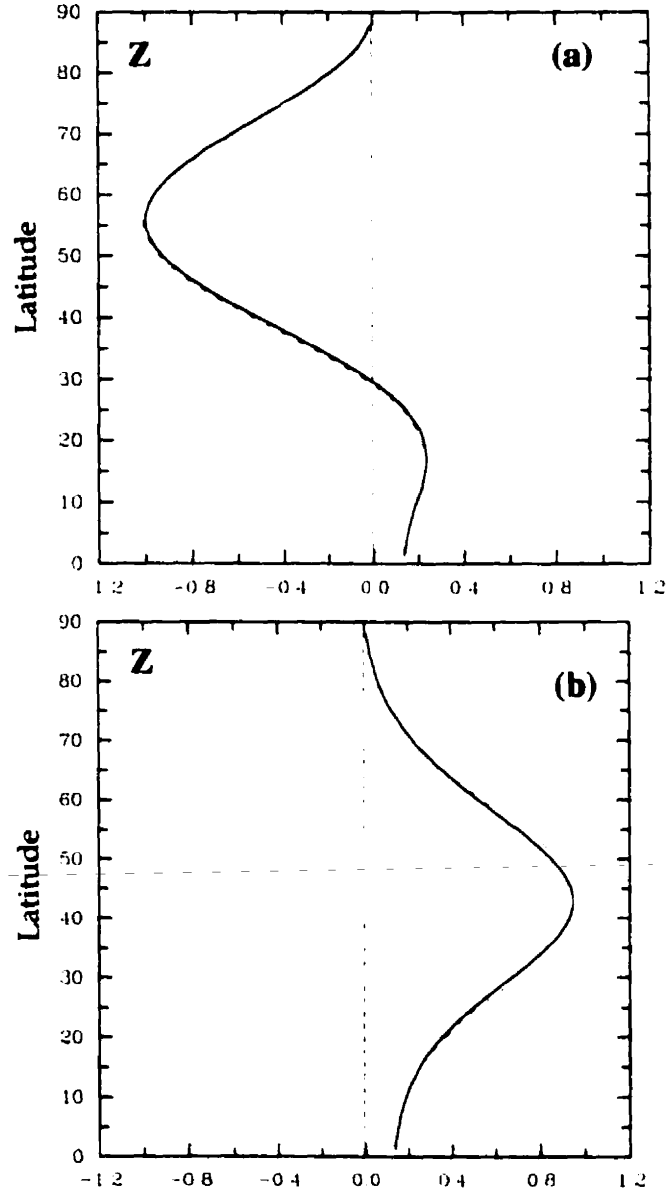

Figure 3.11: **(a)** The first ENM and **(b)** the second ENM of wave number 2 height with mean depth H=8.8 km (ϵ = 10) for 2000-day integration. Cosine is solid and sine is dashed.

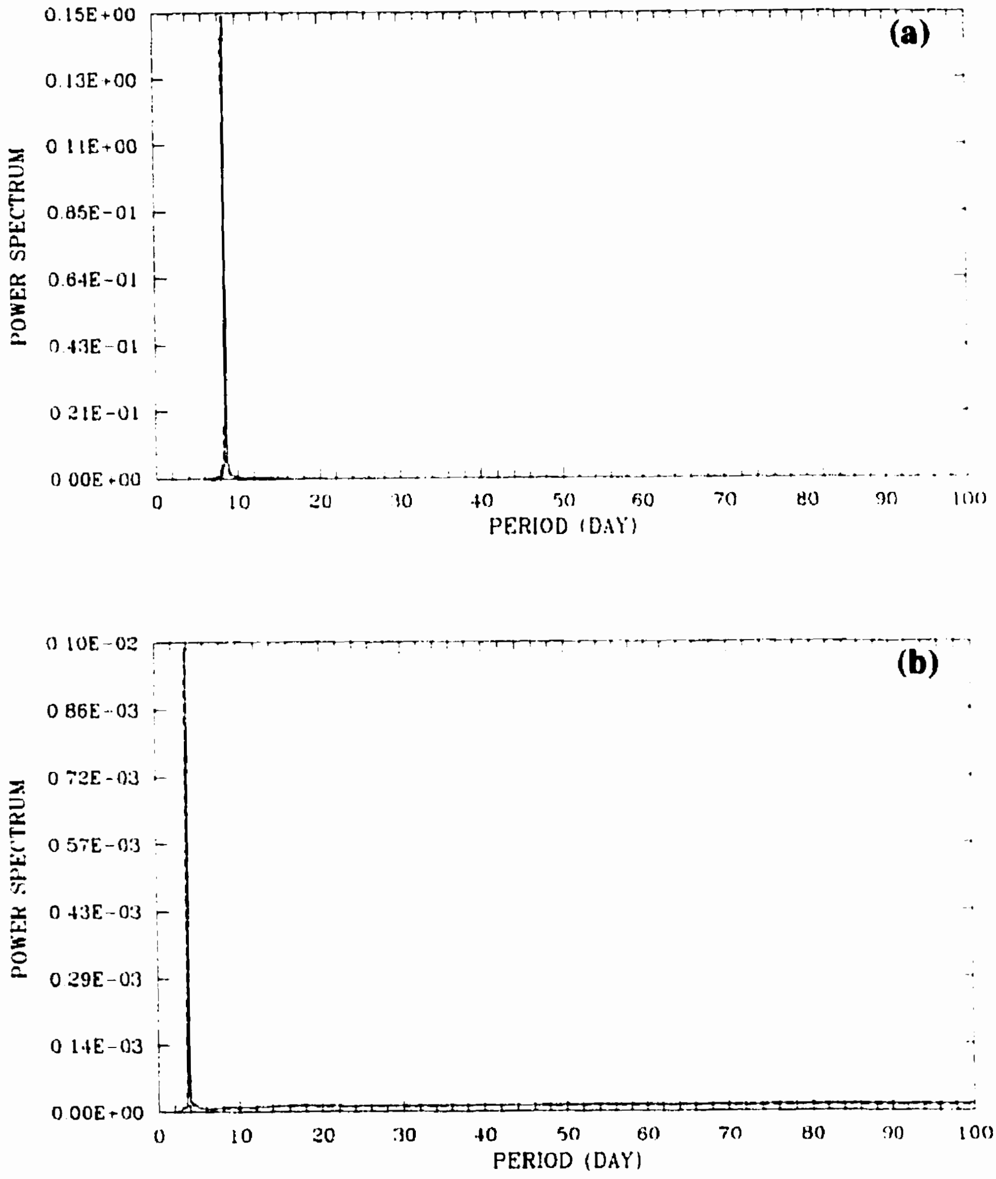

Figure 3.12: **(a)** The first ENM and **(b)** the second ENM power spectra of wave number 2 with mean depth H=8.8 km ($\epsilon = 10$) for 2000-day integration. Cosine is solid and sine is dashed.

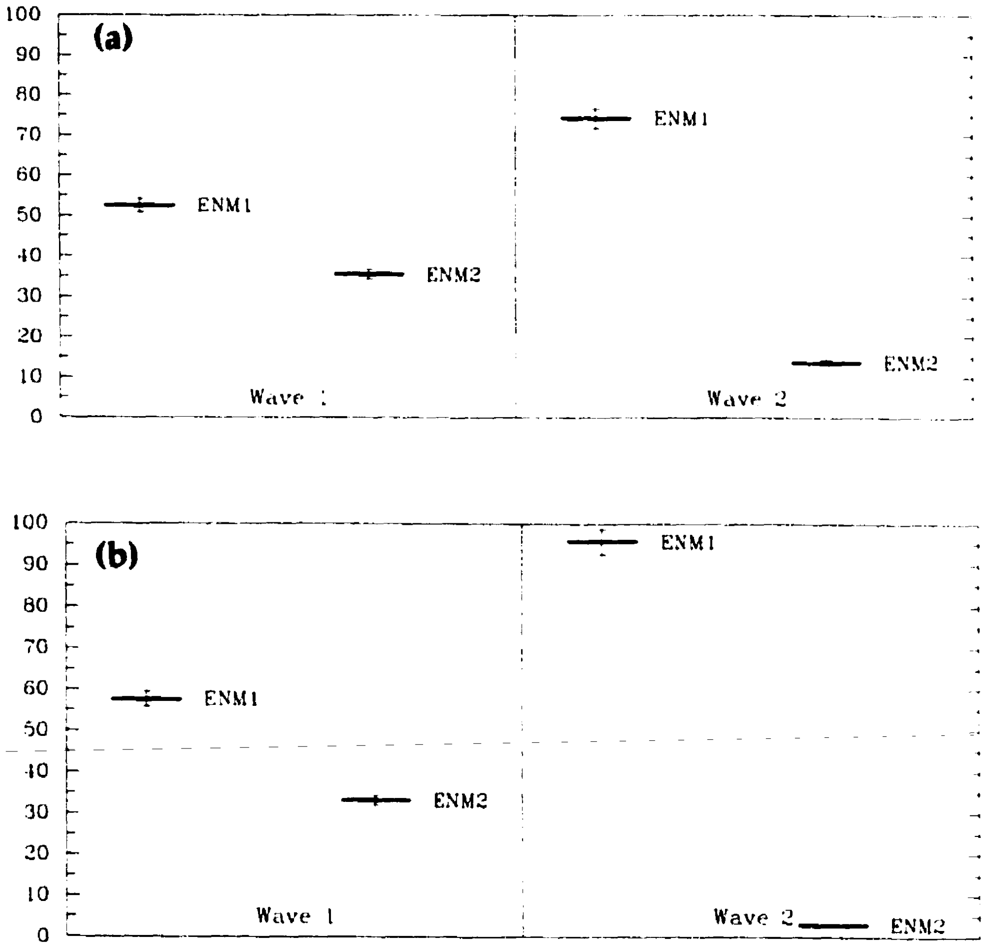

Figure 3.13: The sampling errors of eigenvalues corresponding to mean depths of **(a)** H=0.88 km ($\epsilon = 100$) and **(b)** H=8.8 km ($\epsilon = 10$) respectively.

Table 3.1: Periods (days) and eigenvalues for mean depth of 0.88 km obtained by Longuet-Higgins (LH), from equations (3.13) and (3.16) ["Structure" column] and from the power spectrum.

k	Mode	LH	Structure		Power Spectrum		Eigenvalue %	
			2000 d.	100 d.	2000 d.	100 d.	2000 d.	100 d.
1	ENM1	32.6	32.5	30.1	32.8	31.7	53	80
	ENM2	15.1	15.1	15.8	14.9	14.2	36	15
2	ENM1	17.5	17.5	17.4	17.5	18.1	74	75
	ENM2	8.4	8.3	8.4	8.3	8.8	14	18

Table 3.2: As in Table 3.1 but for a mean depth of 8.8 km

k	Mode	LH	Structure		Power Spectrum		Eigenvalue %	
			2000 d.	100 d.	2000 d.	100 d.	2000 d.	100 d.
1	ENM1	12.6	12.6	11.3	12.6	11.8	58	57
	ENM2	5.3	5.2	5.9	5.2	5.3	33	32
2	ENM1	8.6	8.6	8.4	8.6	8.4	96	80
	ENM2	3.8	3.5	3.4	3.8	3.8	3	18

Chapter 4

Application of ENM Analysis to Atmospheric Data

In the previous chapter, the ENM analysis technique has shown a high degree of accuracy in recovering the Hough modes and their associated frequencies from the linearized 2D shallow water model data sets. With this in mind, we advance further in this chapter and perform an ENM analysis of 3D atmospheric data. The purpose of this study is to use the ENM analysis technique to decompose the atmospheric data into empirical modes. These modes are then used to find common features, in the statistical sense, among stratospheric sudden warming events.

Section 4.1 describes the observational data used in this analysis. From this data set we illustrate, in Section 4.2, some common features in a number of stratospheric warming events which are later used for a comparison with the results of the ENM analysis. Section 4.3 presents the methodology of 3D ENM analysis. The results of the ENM analysis are discussed in Section 4.4.

4.1 Data

The data used for this analysis are daily operational National Center for Environmental Prediction (NCEP) geopotential height fields. The data are available on 15 pressure levels: 700, 500, 400, 300, 250, 200, 150, 100, 70, 50, 30, 10, 5, 2 and 1 hPa and were archived by Dr. William J. Randel at the National Center for Atmospheric Research (NCAR) from two different sources. The tropospheric data from the 700 to the 100 hPa pressure levels were obtained from NCEP analyses while the stratospheric data from the 70 to the 1 hPa levels were separately archived at the Climate Analysis Center (CAC), Washington, D.C. The stratospheric data were first converted from the satellite-retrieved mean layer temperatures between pressure levels to the geopotential thicknesses, ΔZ, by using the hydrostatic equation in finite difference form

$$\Delta Z_i = \frac{R}{g} ln\left(\frac{p_i}{p_{i+1}}\right)\left[\frac{T(p_i)+T(p_{i+1})}{2}\right] \tag{4.1}$$

where R is the gas constant. The thicknesses were then used to compute the stratospheric geopotential heights, starting from the NCEP 100 hPa geopotential heights. This daily global data set has been received from NCAR in the format of Fourier analyses truncated at zonal wave number 12 at each of the 40 Gaussian latitudes sampled at 1200 UTC. Finger *et al.* (1993) have reported that the NCEP analysis data at the 5 hPa level and above need to be adjusted due to the inconsistencies within the satellite TIROS Operational Vertical Sounder (TOVS) derived temperature database. The problem is due to the differences in the behaviour of the various satellite instruments providing the operational data. In addition, other contributions to the problem are related to changes in NCEP data analysis procedures. As suggested by Finger *et al.* the adjustment has been done by using the change in thickness equation:

$$\delta\Delta Z_i = \frac{R}{g} ln\left(\frac{p_i}{p_{i+1}}\right)\left[\frac{\delta T(p_i)+\delta T(p_{i+1})}{2}\right]. \tag{4.2}$$

This adjustment is done based on 12 rocketsonde station records (*in situ* measurements). The temperature biases, δT, between NCEP analyses and rocketsonde data are different at each pressure level and have changed over time. The linear-regression of the form $a + bl$ is used to fit data before and on October 16, 1980 where a is the adjustment at the equator, b is slope of the line and l is the absolute value of the latitude. Data after the above mentioned date are adjusted globally (no latitudinal variation). In this study, the adjusted geopotential heights according to Table 2 of Finger *et al.* (1993) of 15 pressure levels (from 700 to 1 hPa) and 11 winters (Dec. 1, 1979 to Feb. 28, 1990) are used. The winter season is taken to be from the beginning of December to the end of the following February.

In order to perform the ENM analysis of the real atmosphere using the 3D primitive equations (see also Section 2.3), we need 3 fields, namely, the horizontal velocity components (u, v) and temperature. The temperature field is quite simple to calculate from the geopotential height by using the hydrostatic equation. However the calculation of the horizontal winds from the geopotential height data alone is somewhat more complicated. Randel (1987) has used three different methods to evaluate the horizontal winds from the geopotential height: 1) the geostrophic winds, 2) the linearized momentum equations about a zonal mean flow (the linear winds) and 3) the full steady-state momentum equations less the vertical advection term (the balance winds). The lowest order horizontal winds approximation from the geopotential is the geostrophic balance, i.e.,

$$\mathbf{V}_g = \frac{1}{f}\mathbf{k} \times \nabla\Phi \tag{4.3}$$

where $\Phi = gZ$ is the geopotential, $\mathbf{V}_g$ is geostrophic winds and $\mathbf{k}$ is vertical unit vector. The higher order nonlinear wind-height balance, i.e.,

$$\nabla^2 \left[\Phi + \frac{1}{2}(\nabla\psi)^2\right] = \nabla \cdot [(f + \nabla^2\psi)\nabla\psi] \tag{4.4}$$

is also considered. The relation between the streamfunction, ψ, and the non-divergent wind is given by (1.24). The above equation can be solved for the wind from the geopotential by an iteration method starting from the geostrophic wind. The convergence of the solution to the equation often fails in the northern winter stratosphere where the amplitudes of planetary waves are usually large [see Randel 1987 for a more detailed discussion of the nonlinear balance winds]. The linear winds in the second method above are calculated from the horizontal momentum equations linearized about the zonal mean without the time tendency and vertical advection terms, that is,

$$\frac{\bar{u}}{a\cos\phi}\frac{\partial u'}{\partial\lambda} - f_1 v' = -\frac{1}{a\cos\phi}\frac{\partial\Phi'}{\partial\lambda} \qquad (4.5)$$

and

$$\frac{\bar{u}}{a\cos\phi}\frac{\partial v'}{\partial\lambda} + f_2 u' = -\frac{1}{a}\frac{\partial\Phi'}{\partial\phi} \qquad (4.6)$$

where overbars denote a zonal mean, primes describe the deviations from the zonal mean and

$$f_1 = f - \frac{1}{a\cos\phi}\frac{\partial}{\partial\phi}(\bar{u}\cos\phi)$$

$$f_2 = f + \frac{2\bar{u}}{a}\tan\phi.$$

The coupled equations (4.5) and (4.6) are easily solved for each zonal wave number of u' and v'.

In the balance winds (last method), again, the time tendency and vertical advection terms are neglected from the horizontal momentum equations to make the iterative scheme two-dimensional. Following is the calculation of the winds by the balance winds method. The horizontal momentum equations less the time tendency and the vertical advection terms can be expressed in spherical coordinates as:

$$v = \frac{1}{2\Omega a sin\phi cos\phi}\left\{\frac{\partial\Phi}{\partial\lambda} + \left[u\frac{\partial u}{\partial\lambda} + v\frac{\partial}{\partial\phi}(u cos\phi)\right]\right\} \qquad (4.7)$$

and

$$u = -\frac{1}{2\Omega a sin\phi}\left\{\frac{\partial\Phi}{\partial\phi} + \left[v\frac{\partial v}{\partial\phi} + u^2 tan\phi + \frac{u}{cos\phi}\frac{\partial v}{\partial\lambda}\right]\right\}. \qquad (4.8)$$

The geostrophic winds are first calculated by neglecting the nonlinear terms (inside the square brackets). Each iteration is evaluated by using the previous step winds. The convergence of the balance winds is measured by the ratio of the relative wind change between each iteration and the previous step wind, e.g.,

$$\epsilon(\phi) = \sqrt{\epsilon_u^2(\phi) + \epsilon_v^2(\phi)} \tag{4.9}$$

where the relative zonal mean RMS difference for u component is

$$\epsilon_u(\phi) = \left[\frac{\int_0^{2\pi} d\lambda [u_n(\lambda, \phi) - u_{n-1}(\lambda, \phi)]^2}{\int_0^{2\pi} d\lambda [u_{n-1}(\lambda, \phi)]^2} \right]^{\frac{1}{2}} .$$

All three derived winds from the geopotential alone were calculated in Randel (1987) using a General Circulation Model (GCM) output and the results compared to the "true" GCM winds. The comparisons have shown that the balance winds [equations (4.7)-(4.8)] are superior to the other two in the tests of zonal mean wind ($\overline{u}$) as well as the poleward momentum ($\overline{u'v'}$) and heat ($\overline{v'T'}$) fluxes.

Based on these results, we adopt the balance winds method to calculate winds for our analysis. If the solution fails to converge, e.g., $\epsilon(\phi)$ in (4.9) approaches to a small value (< 0.1) then the geostrophic wind is substituted for that particular location (not all points along the latitude circle). Practically, when the wind fails to converge at a certain point, its value becomes unreasonably high (order of thousands of metres per second or higher). Generally only three iterations are required to give a good result in comparison to model winds (Randel 1987). Because all the derivatives in (4.7) and (4.8) are done spectrally, new variables $\tilde{u} = u \cos\phi$ and $\tilde{v} = v \cos\phi$ are used so that the new variables are zero at the poles.

4.2 Observations of Stratospheric Sudden Warmings

In Section 1.3 we discussed the upward propagation of the planetary (Rossby) waves from the troposphere to the stratosphere and their interaction with the preexisting stratospheric circulation that might lead to a sudden stratospheric warming. This dynamical mechanism was first proposed by Matsuno (1971). We also showed in Fig. 1.4 the temperature gradient and zonal mean wind reversal at 80° of latitude and the 10 hPa pressure level during the 1984/85 major warming event. This type of figure will be used to identify the warming events [major and minor warmings are defined in Section 1.3]. In addition to that type of diagram, we also show in Fig. 4.1 the meridional-height zonal mean wind (for Northern Hemisphere only) to provide some idea of the evolution of the wind before and during the warming. Figure 4.1a shows the zonal mean wind on Dec. 24, 1984 (4 days before the warming onset). The wind structure is quite similar to the climatological one shown in Fig. 1.2 where the polar night jet is centred at around 45°N in the lower mesosphere. The jet in the troposphere which is located near (35°N, 200 hPa), is also similar in both figures. On the onset day (Dec. 28), the centre of the polar night jet shifted northward and downward to approximately 68°N and 1.5 hPa while the tropospheric jet strengthened somewhat as shown in Fig. 4.1b. Figure 4.1c exhibits the zonal mean wind when the zonal temperature at 80°N and 10 hPa reached its highest value in Fig. 1.4 (Jan. 1, 1985). The normal westerly wind in the polar region is now replaced by an easterly one, and again the tropospheric jet is almost still the same (in magnitude and position).

The average of nine (out of 11 years) observed pre-warmings (onsets) of the zonal mean wind is shown in Fig. 4.2. In comparison to Fig. 1.2 (the winter climatological zonal wind), the structure of the onset and winter climatological tropospheric jets are

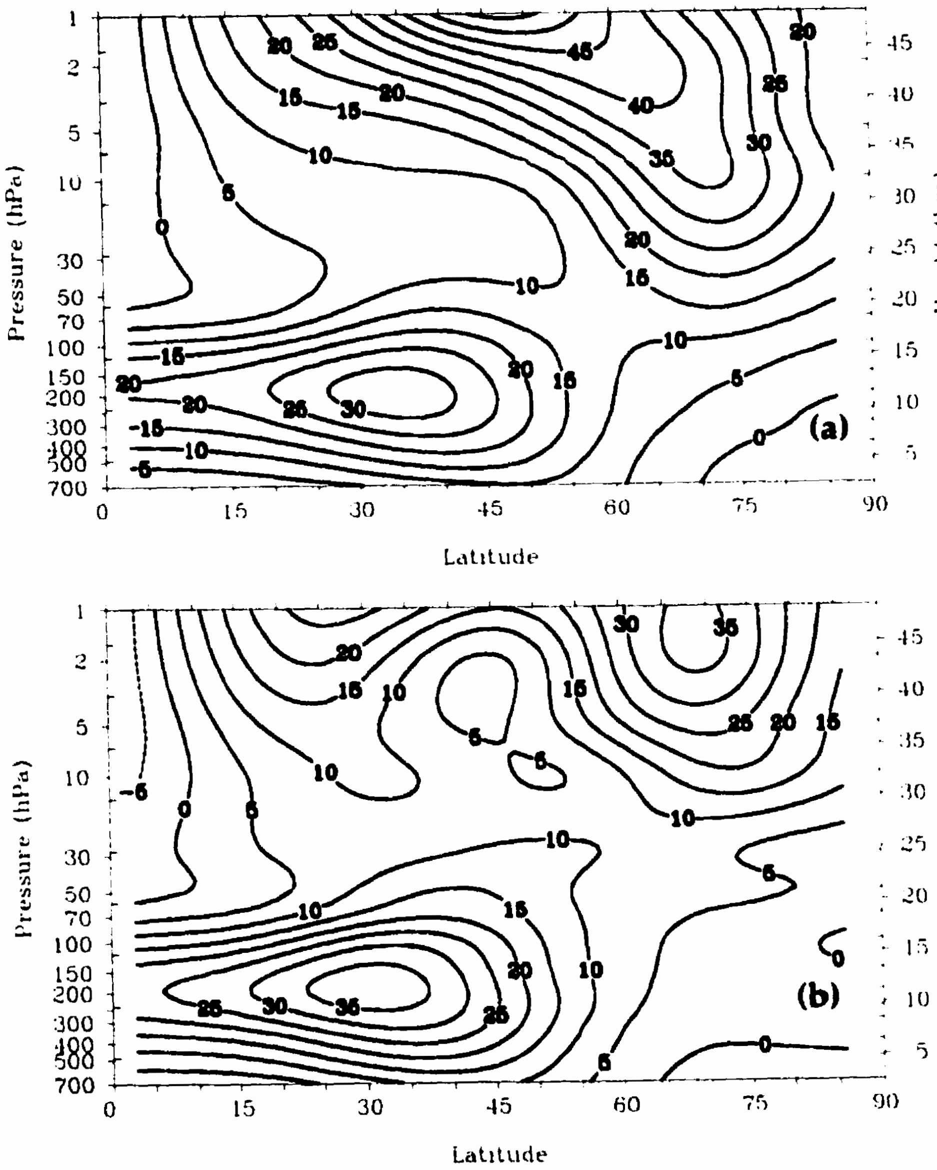

Figure 4.1: Observed zonal mean wind (ms^{-1}), derived from the geopotential height alone for the 1984/85 stratospheric major warming (**a**) December 24, 1984 (onset), (**b**) December 28, 1984 (middle) and (**c**) January 1, 1985 (peak) (*Figure continued.*)

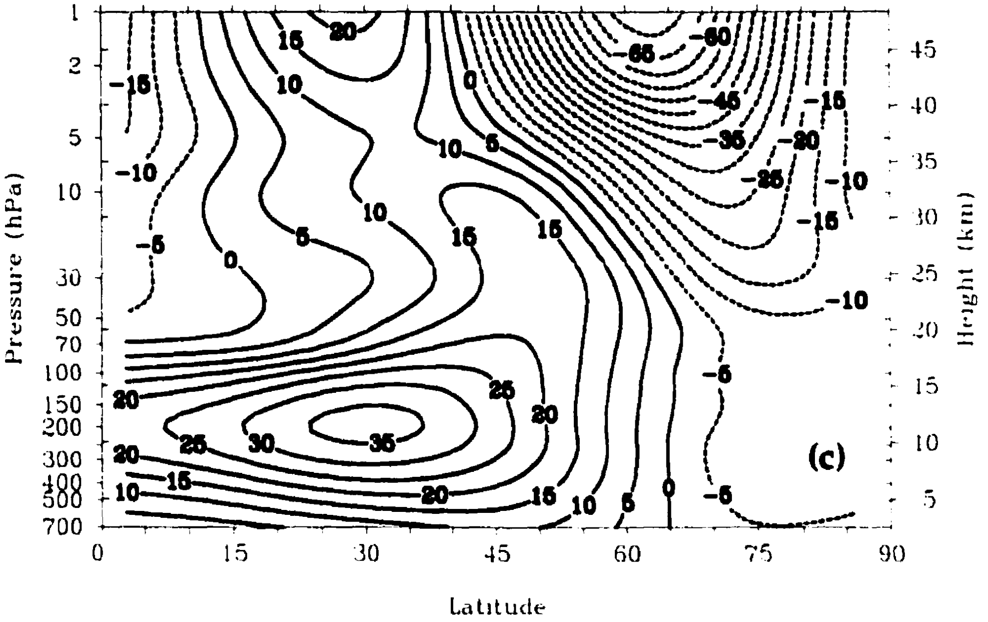

Figure 4.1: *(continued)*

similar. However the downward and poleward shifting from (45°N, 0.1 hPa) to (68°N, 2.5 hPa) of the onset stratospheric jet is observed in Fig. 4.2. The climatological southward tilt with height of the polar night jet is also replaced by a slightly northward tilt in the onset figure. If the zonal mean wind acts as a wave guide (see discussion in Matsuno, 1970 and Dickinson, 1968) then the onset zonal mean flow structure is more favourable to the direct upward propagation of waves to the polar region than the climatological one which guides the waves toward to the low latitudes. Butchart *et al.* (1982) used a fully nonlinear model to simulate the 1978/1979 winter major warming by starting with the onset zonal mean structure of February 16, 1979 and forced the model by the observed geopotential height at 100 hPa. They concluded that it is important to use the onset flow structure as the initial zonal mean wind instead of the climatological one to make the warming more likely to occur. They also

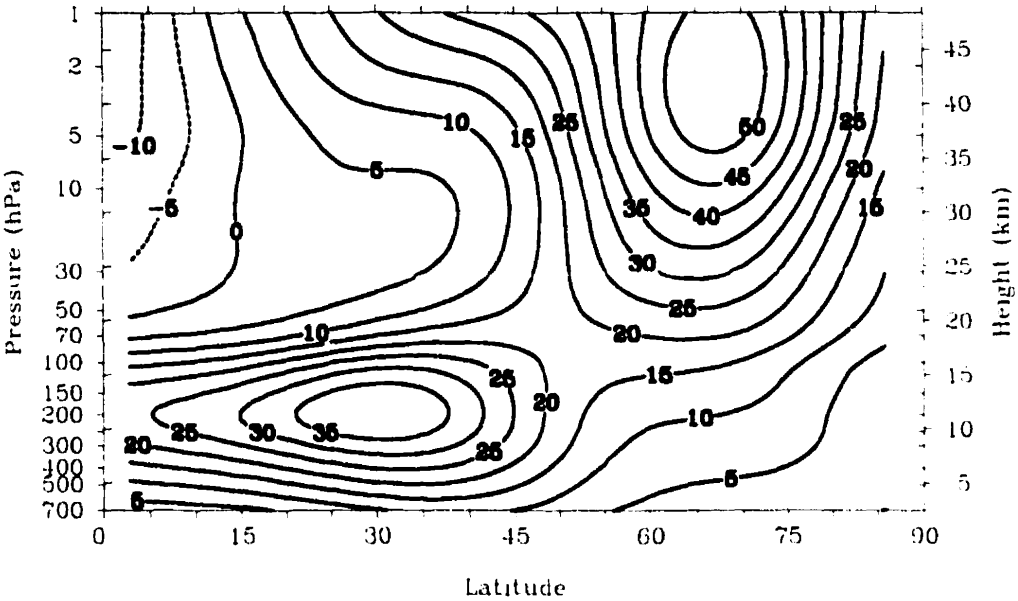

Figure 4.2: Average of 9 pre-warmings (onsets) zonal mean wind from 1980-1990 data set (both minor and major warmings are included).

found that the wave number 2 forcing should have an eastward phase speed and that the wave-wave interactions were not important for the development of the warming. The Butchard *et al.* case study warming agree quite well with the average of nine warmings (both major and minor) shown in Fig. 4.2.

The feature-rich stratospheric warmings are observed not only in the zonally average pictures (latitude-height diagrams) of the wind structure as described above but also in the wave structures. The normal cyclonic winter polar vortex in the middle stratosphere (10 hPa level) is pushed off the pole and sometimes a splitting of the main vortex (corresponding to the involvement of wave number 2) can be seen. We show in Fig. 4.3 the winter climatological QG potential vorticity. Comparing this chart to the winter climatological geopotential height in Fig. 1.3 we see that they have rather similar patterns except of course that the maximum in one field corresponds to a minimum in the other. The reason we show the observed QG potential

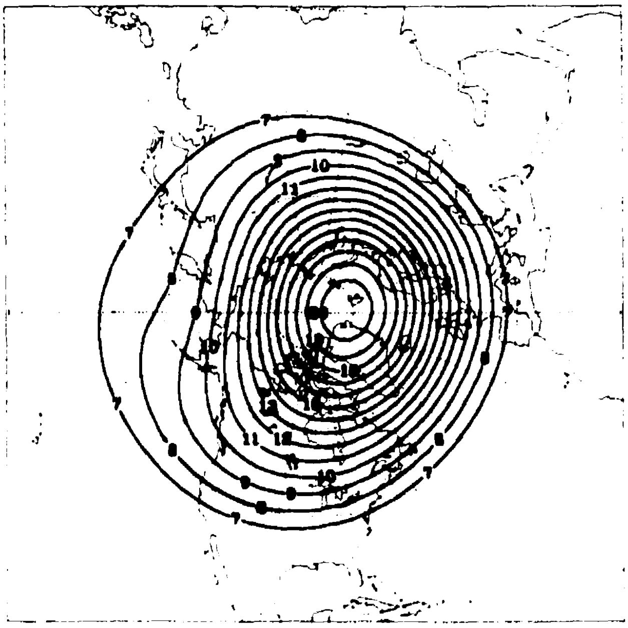

Figure 4.3: Polar stereographic map of 11-winter climatological quasi-geostrophic potential vorticity (QGPV) at 10 hPa (approximately 30 km) (contour interval of 1×10^{-5} s^{-1}); inner circle 80°N.

vorticity instead of the better-known geopotential height is that the QG potential vorticity, which can be approximated from Π in equation (A.13) (one component of the wave vector), is available from the ENM analysis for interpretation. Figures 4.4 and 4.6 show the observed QG potential vorticity (QGPV hereafter) at 10 hPa during the 1980/81 and 1984/85 major warming events, respectively. Figure 4.4a exhibits the elongation of the normal cyclonic polar vortex (see Fig. 4.3) at the onset (Jan. 20, 1981) of the warming. This elongated polar vortex is then pushed off the pole (Jan. 25, 1981) and the local low value of QGPV appears around (160°W, 65°N) in Fig. 4.4b. At this time, the zonal mean temperature at (80°N, 10 hPa) reaches its maximum value in Fig 4.5. The temperature decreases a few degrees two days later

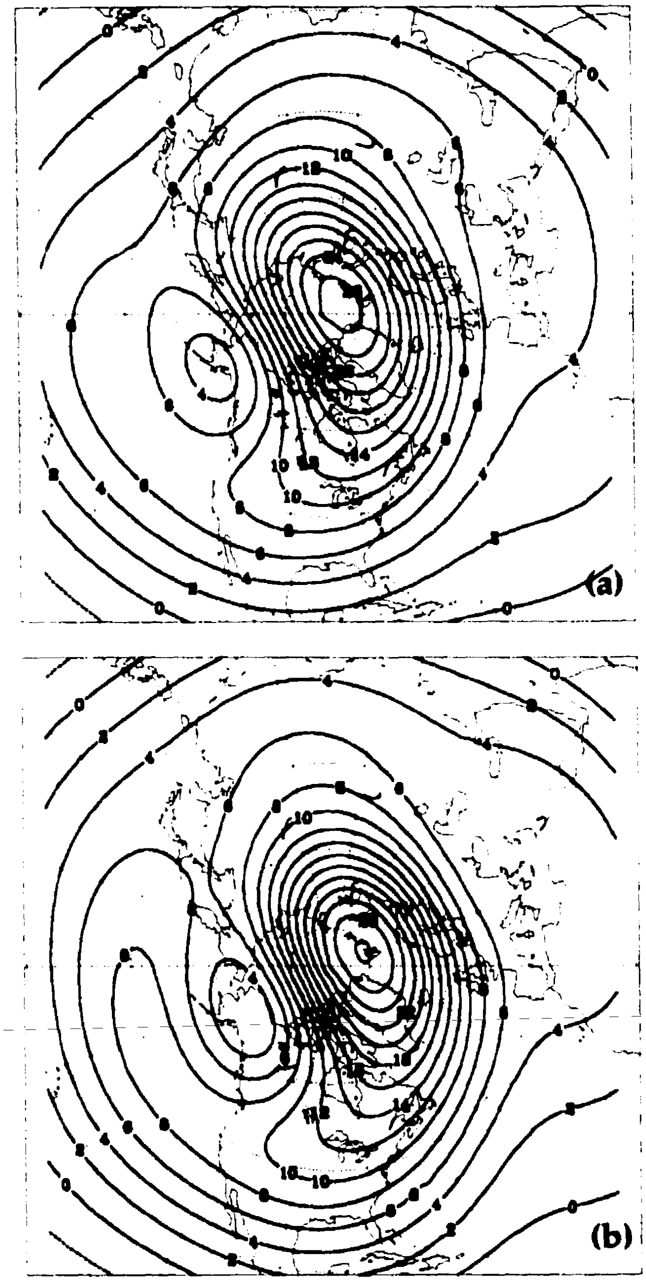

Figure 4.4: Polar stereographic maps of quasi-geostrophic potential vorticity (QGPV) at 10 hPa (approximately 30 km) (contour interval of $2 \times 10^{-5}\ s^{-1}$) for 1980/81 warming **(a)** January 20, 1981 (onset), **(b)** January 25, 1981 (first zonal temperature peak), **(c)** January 31, 1981 (second peak) and **(d)** February 5, 1981 (last peak). Outer circle, 20°N; inner circle 80°N. (*Figure continues*)

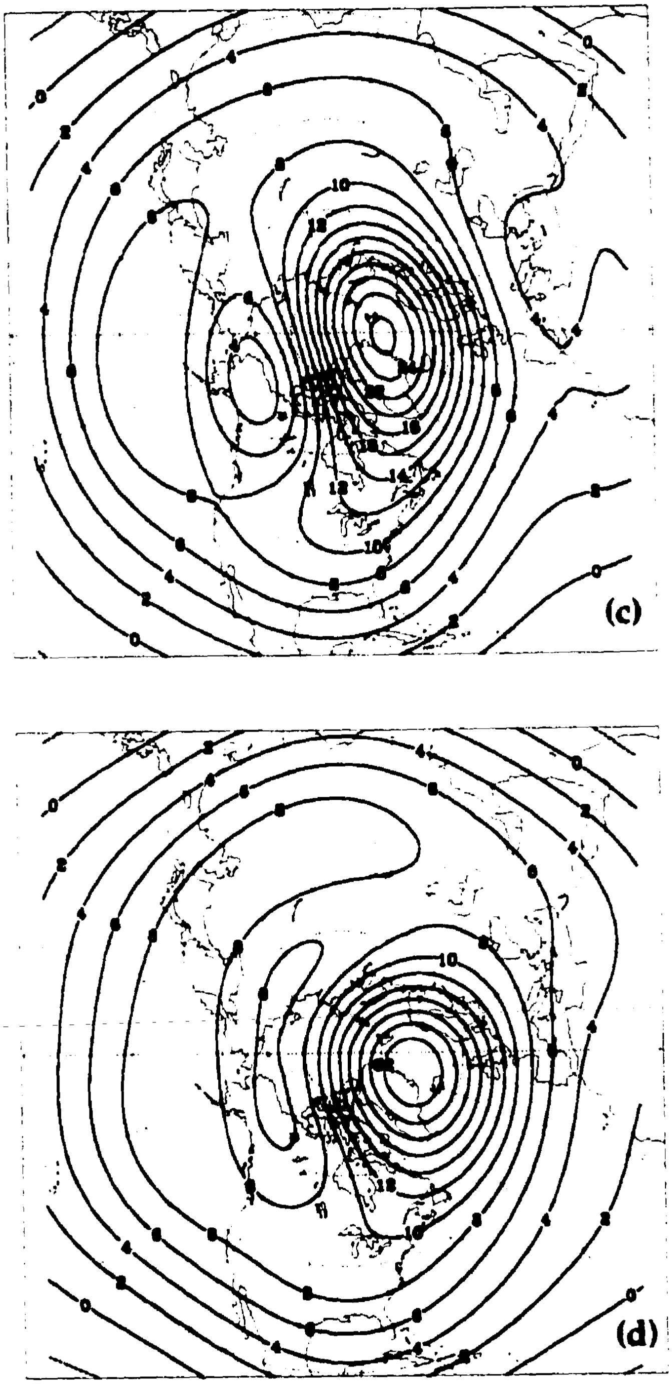

Figure 4.4: *(continued)*

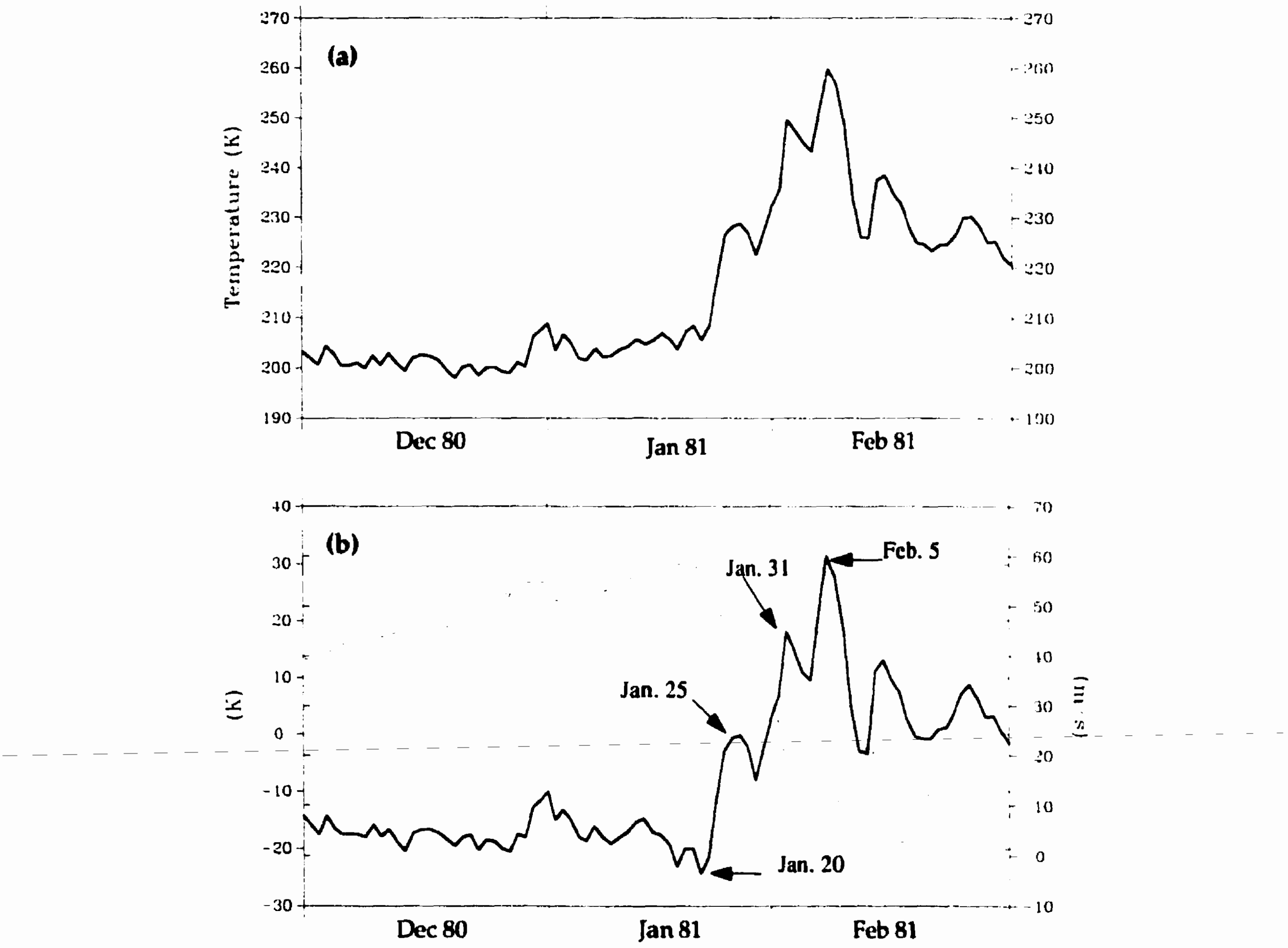

Figure 4.5: Observed winter 1980/81 (DJF) major warming at 10 hPa (**a**) zonal mean temperature at 80°N and (**b**) zonal mean temperature difference between 80°N and 50°N (solid) and zonal mean zonal wind at 65°N (dashed).

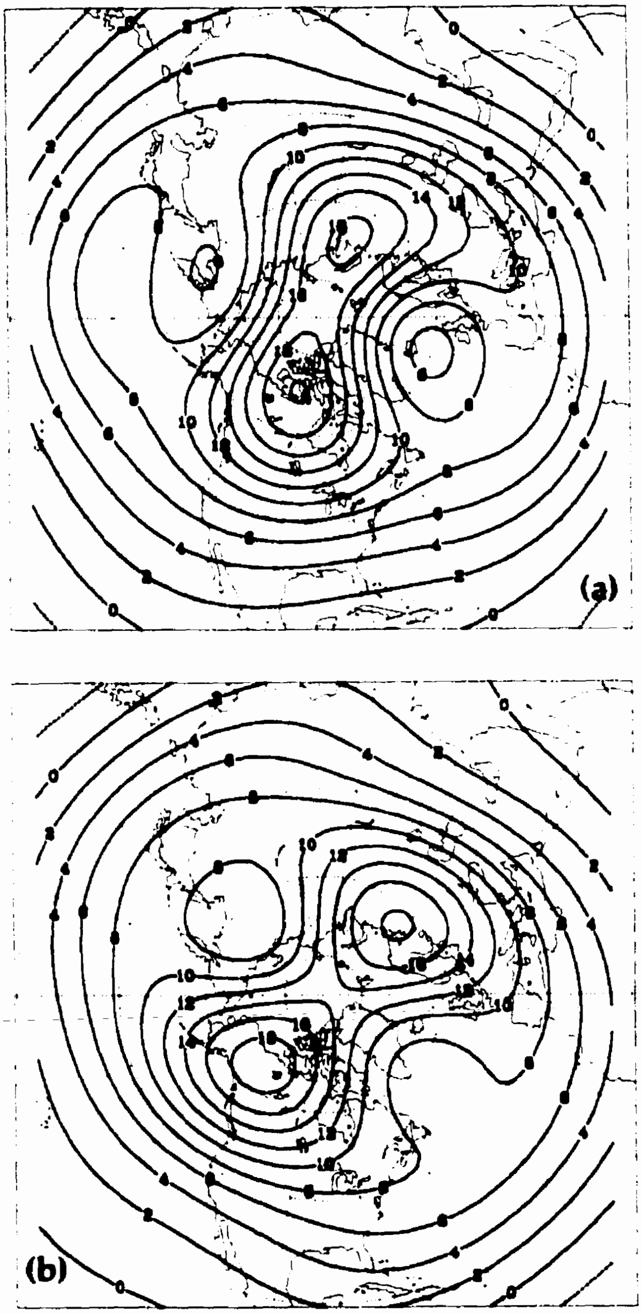

Figure 4.6: Polar stereographic maps of quasi-geostrophic potential vorticity (QGPV) at 10 hPa (approximately 30 km) (contour interval of $2 \times 10^{-5}\ s^{-1}$) for 1984/85 warming **(a)** December 28, 1984 (onset), **(b)** December 30, 1984 (middle) and **(c)** January 1, 1985 (zonal temperature peak). Outer circle, 20°N; inner circle 80°N. (*Figure continues*)

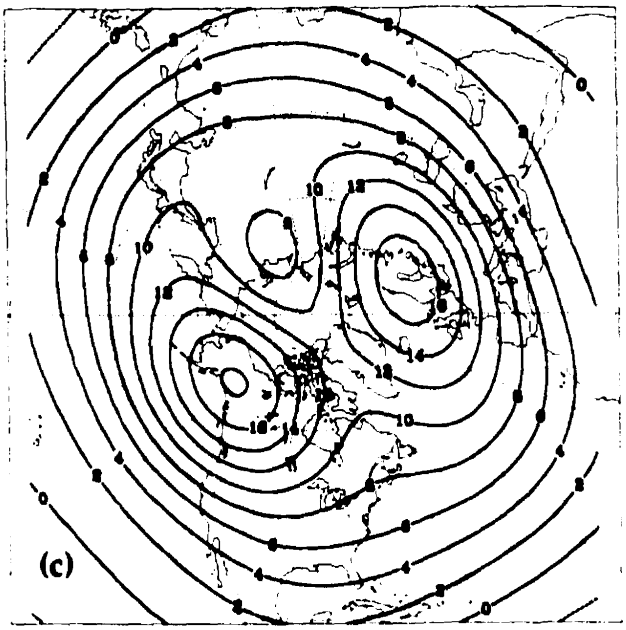

Figure 4.6: *(continued)*

and then reaches a new higher maximum value in Jan. 31, 81. The QGPV chart of this second maximum is shown on Fig. 4.4c which exhibits further equatorward movement of the polar vortex. The first two temperature maxima correspond to a minor warming in which the zonal mean westerly wind is not yet reversed. The major warming occurs on Feb. 5, 1981 when the wind reverses and the temperature reaches its highest value. Figure 4.4d shows further southward movement of the polar vortex. In this warming year, only zonal wave number 1 is involved in an important way and no vortex splitting occurs. In contrast, the 1984/85 major warming takes a different form, with only wave number 2 being involved from the beginning to the end, with no significant development of wave number 1. Figure 4.6a shows the development of two local low QGPV centres along the 20°W–160°E longitude line and the main vortex is squeezed and starts to break into two separated centres from the beginning of the warming (Dec. 28, 1984). While the zonal mean temperature rises at 10 hPa (see Fig. 1.4a), the polar vortex splits into two high centres on Dec. 30, 1984 (clearly seen in Fig. 4.6b). When the temperature reaches its maximum value on Jan. 1, 1985, the polar vortex (QGPV high) at the pole is replaced by a QGPV low and the vortex is completely separated into two high QGPV centres (Fig. 4.6c). These two typical warming scenarios in the stratosphere are often seen on synoptic maps.

4.3 Methodology

Similarly as in Section 3.3, we describe in this section the calculation of the ENMs for each zonal wave number using the primitive equations and its QG approximation. Based on the theory developed in Section 2.3, the wave vector for 3D primitive equations in (2.59) consists of 3 components, namely, the modified Ertel potential vorticity in log-pressure coordinate, Π, the potential temperature, θ, and the vertical wind shear, u_z. From the available data discussed in Section 4.1, we have derived the horizontal wind (u, v) with the balance equation and the temperature from geopotential height via the hydrostatic approximation. The potential temperature is computed from temperature with the relation $\theta = T(p/p_0)^{-\kappa}$. From the horizontal wind and potential temperature fields we use (A.5) to calculate the Ertel potential vorticity, P. The wave vector, $\mathbf{X}$, is formed based on (2.59). The wave vector is then zonally Fourier transformed into sine and cosine components for each wave number. For each sine and cosine component we separately construct the pseudo-momentum matrices according to (2.58). Notice that since we do not want to include the standing wave structure as one of the empirical modes, the time mean, of the wave vector is removed first, i.e., before the ENM analysis. The eigenvalue problem associated with these pseudo-momentum matrices (see (2.60)) is readily solved for the modal structures, $X_n(\phi, z)$, and their associated eigenvalues. The time series of each structure is calculated by projecting the observed wave vector onto each normal mode, e.g.,

$$a_n(t) = \frac{\left\langle X_n^\dagger(\phi, z)\mathbf{P}X(\phi, z, t)\right\rangle}{\left\langle X_n^\dagger(\phi, z)\mathbf{P}X_n(\phi, z)\right\rangle} \tag{4.10}$$

where the angle brackets denote the meridional and vertical integration.

In this study we partition the 11-winter data set (993 days) into two parts, namely, the "warming events" (269 days) and the rest of the data set (724 days). A "warming event" (or "warming period") is one during which the mean zonal temperature gradient between 50 and 80°N becomes positive at 10 hPa. More precisely, a warming event begins when $\overline{T}_{80N}$ starts to rise, its peak is reached when $\Delta\overline{T} = \overline{T}_{80N} - \overline{T}_{50N} > 0$ reaches a maximum and the event ends when $\Delta\overline{T}$ returns to a negative value. Note that as defined above, a "warming event" or "warming period" includes in fact a cooling phase during which $\Delta\overline{T}$ is decreasing. EOFs will be computed separately for "warming events" and for the rest of the winter data sets. The dates of the events are given in Table 4.1.

Since the data set has been partitioned in the above mentioned manner, using the power spectrum analysis method to find the frequencies of empirical modes (ENMs) is not applicable due to the gaps in the time series. In addition, the dynamics of the real atmosphere is generally not linear and the flow is not purely free (some forcing may be involved) so that the time series of amplitudes is quite noisy. To overcome the above problems, we use the kernel estimation technique to smooth out noise in the sine and cosine phase space diagram of each ENM. The kernel estimation technique can be used to interpolate data, α_i, at irregularly-spaced points, identified by the subscript i, to regularly-spaced points, by computing a weighted average of the data

Table 4.1: The dates of the warming events during winters 1979/80-1989/90.

Warming Periods			
Beginning	Max. temp.	Ending	Number of days
20-01-81	05-02-81	28-02-81	40
19-01-82	27-01-82	30-01-82	12
08-02-82	13-02-82	16-02-82	9
24-02-82	27-02-82	28-02-82	5
23-01-83	29-01-83	31-01-83	9
03-02-83	03-06-83	11-02-83	9
20-02-83	26-02-83	28-02-83	9
27-12-83	31-12-83	01-01-84	6
03-02-84	07-02-84	08-02-84	6
15-02-84	23-02-84	29-02-84	15
28-12-84	01-01-85	13-01-85	17
18-01-86	20-01-86	24-01-86	7
14-02-86	18-02-86	19-02-86	6
02-01-87	23-01-87	10-02-87	40
01-12-87	10-12-87	16-12-87	16
21-01-89	29-01-89	31-01-89	11
03-02-89	12-02-89	28-02-89	26
03-02-90	10-02-90	28-02-90	26

α_i, i.e.,

$$f(\alpha, \mathbf{a}) = \frac{1}{2\pi N h^2} \sum_{i=1}^{N} \alpha_i \exp\left(-\frac{1}{2}\left|\frac{\mathbf{a} - \mathbf{a}_i}{h}\right|^2\right) \tag{4.11}$$

where $f(\alpha, \mathbf{a})$ is the value of α at $\mathbf{a}=(a^c_{n,k}, a^s_{n,k})$, $a^c_{n,k}, a^s_{n,k}$ being the coordinates of the domain. In our case they are the coefficients of the $\cos(k\lambda)$ and $\sin(k\lambda)$ of the mode n and wave number k. h determines the size of the region over which the weighted average is done, N is the number of data points used in the weighted average. We note that when α is set equal to one, f yields an estimation of the probability density of the data points. For the optimal choice of the smoothing parameter, h, (which minimizes the root-mean-integrated-square error between the data set and the estimation) one can refer to the Appendix of Brunet (1994). Based on this probability density we estimate the tendency from

$$\bar{\dot{\mathbf{a}}} = \frac{f(\dot{\mathbf{a}}, \mathbf{a})}{f(1, \mathbf{a})} \tag{4.12}$$

where $\dot{\mathbf{a}} = (\mathbf{a}(t + \Delta t) - \mathbf{a}(t - \Delta t))/2\Delta t$ (Δt=24 hours) is the rate of change of the position. If we write $\mathbf{a}$ in a polar coordinate system, e.g., $\dot{\mathbf{a}} = \dot{a}_r \hat{r} + \dot{a}_\theta \hat{\theta}$, then $\dot{a}_r$ represents the amplitude growth of the ENM while $\dot{a}_\theta$ exhibits the rotation or phase speed.

In a frictionless adiabatic atmosphere the Ertel potential vorticity is a conserved quantity following the total flow. If the Ertel potential vorticity is derived in isentropic (constant potential temperature) coordinates and in the absence of diabatic heating ($d\theta/dt = 0$) there is then no "vertical" velocity so that particles will be confined to the isentropic surface. Similar to the isentropic Ertel potential vorticity, the QGPV is conserved following the geostrophic wind if the flow is frictionless and adiabatic. In other words, the QGPV is conserved on isobaric surfaces. We have used the log-pressure as the vertical coordinate so that it is natural to use the QGPV to discuss our results in the next section.

Since the QGPV is conserved on isobaric surfaces, it is natural to use this quantity to discuss results from the analysis. However, one component of the empirical modal structure from the ENM analysis technique is the modified Ertel potential vorticity, not the QGPV. Therefore we here describe how the QGPV can be approximated from the modified Ertel potential vorticity, Π. We first relate the QGPV gradient in (1.15) to the $\overline{J}$ defined in (A.14). Charney and Stern (1962) have shown the relationship between the derivative of the Ertel potential vorticity in isentropic coordinates and the QGPV in log-pressure coordinate to be:

$$\frac{1}{a}\left(\frac{\partial q}{\partial \phi}\right)_{z=const} = \frac{\rho}{a\theta_z}\left(\frac{\partial P}{\partial \phi}\right)_{\theta=const}. \tag{4.13}$$

where, as before, z is proportional to the logarithm of pressure. Taking the zonal average of the above equation we obtain (to leading order)

$$\frac{1}{a}\left(\frac{\partial \overline{q}}{\partial \phi}\right)_{z=const} = \frac{\rho}{a\overline{\theta}_z}\left(\frac{\partial \overline{P}}{\partial \phi}\right)_{\overline{\theta}=const}. \tag{4.14}$$

From the usual formula of derivative transformation in different vertical coordinates we relate the derivative of the zonal mean potential in isentropic and log-pressure coordinates as

$$\left(\frac{\partial \overline{P}}{\partial \phi}\right)_{\overline{\theta}=const} = \left(\frac{\partial \overline{P}}{\partial \phi}\right)_{z=const} - \overline{P}_z\overline{\theta}_z^{-1}\overline{\theta}_\phi. \tag{4.15}$$

Substituting (4.15) into (4.14) and using (A.14) we obtain the relation between the QGPV gradient and $\overline{J}$ as

$$\overline{q}_y = \frac{\rho}{\overline{\theta}_z^2}\overline{J}. \tag{4.16}$$

Furthermore, the zonal mean Ertel potential vorticity (A.7) and its perturbation (A.8) can be approximated in the quasi-geotrophic formulation as

$$\overline{P} = \frac{f_o\theta_{oz}}{\rho} \tag{4.17}$$

and

$$P' = \frac{\theta_{oz}}{\rho}(v'_{gx} - u'_{gy}) + f_o\theta'_z \tag{4.18}$$

where $\theta_o = \theta_o(z)$ is the horizontally averaged (background) vertical potential temperature profile. By using the perturbation QGPV in (1.14) and (4.18) we obtain

$$\frac{\rho}{\theta_z}\Pi' = q'. \tag{4.19}$$

The last two terms (A_2 and A_3) of the wave activity in (A.34) were calculated and shown to be negligible in comparison to A_1, so that the equivalent wave activity under the QG approximation (mid-latitude ($\phi_o = 45°$) β-plane) is

$$a\rho A_1 \cos\phi = \frac{1}{2} a\rho \cos\phi_o \frac{\overline{q'^2}}{\overline{q}_y}. \tag{4.20}$$

In the last part of this section we are going to discuss the wave-zonal flow interaction in terms of an ENM analysis. In Section 1.2 we have shown the relationship between the zonal mean wind tendency and the EP flux divergence (equation 1.6) in the β-plane QG approximation. In spherical geometry, this equation becomes

$$\overline{u}_t - f\overline{v}^* = \frac{1}{a\rho\cos\phi}\nabla\cdot\mathbf{F} \tag{4.21}$$

where the EP flux, **F**, is

$$\mathbf{F} = (F^{(\phi)}, F^{(z)}) = (-\rho a \cos\phi \overline{v'u'}, \rho a \cos\phi f \overline{v'\theta'}/\theta_{oz}). \tag{4.22}$$

The right-hand side of (4.21) represents the forcing of the eddies (waves) on the zonal mean flow. During a warming period, the plots of the EP flux and its divergence at various times are used as a diagnostic tool to see the flow of the wave activity (see Andrews *et al.* 1987 Section 6.2.3 for a more detailed discussion of the EP flux and its divergence during the 1978/79 winter warming). From the ENM analysis we obtain wave vector structures (ENMs) which cannot be used directly to form the EP flux vector; the latter requires the empirical modes of u'_n, v'_n and θ'_n as shown in (4.22). However, we can use the results of the ENM analysis to calculate the wave activity for each empirical mode and from its time derivative obtain the EP flux divergence (from the generalized Eliassen-Palm theorem, equation (1.12)).

We will use (4.19) and (4.20) along with the time tendency of the wave activity to discuss the results of the ENM analysis in the next section.

4.4 The Results of the 3D Primitive Equations ENM Analysis

In this Section we illustrate the QG approximation of the results of the ENM analysis based on the 3D primitive equations applied to the 11-winter data set mentioned in Section 4.1. The main purpose of this study is to use the ENM formulation to analyze data during stratospheric warming events in a statistical sense. It is well-known that the disturbances in the stratosphere consist predominantly of ultra-long waves (zonal wave numbers 1 and 2) due to the upward propagating waves from the troposphere (see Section 1.1). From the data set we verify this by computing the variance of the zonal wave number 3 relative to the total variance in the middle stratosphere (10 hPa pressure level). The result shows that the ratio is less than 2%. Based on this calculation we only discuss the ENM analysis results for zonal wave numbers 1 and 2.

We first present the latitude-height graphs of the first two QGPV empirical modes (the most important) of wave numbers 1 and 2 for both warming events and the rest of the data sets. Note that the parity in these diagrams is not important. From these diagrams we can deduce the relative importance between the two periods of the wave activity, which is proportional to the square of the QGPV (equation (4.20)). The ENMs are multiplied by the mean absolute value of their time series to make the comparison meaningful. Figures 4.7a and b show the ENM1 of the cosine of wave number 1 for the warming and non-warming periods, respectively. The sine Fourier components, which were also analyzed, gave similar results and are therefore

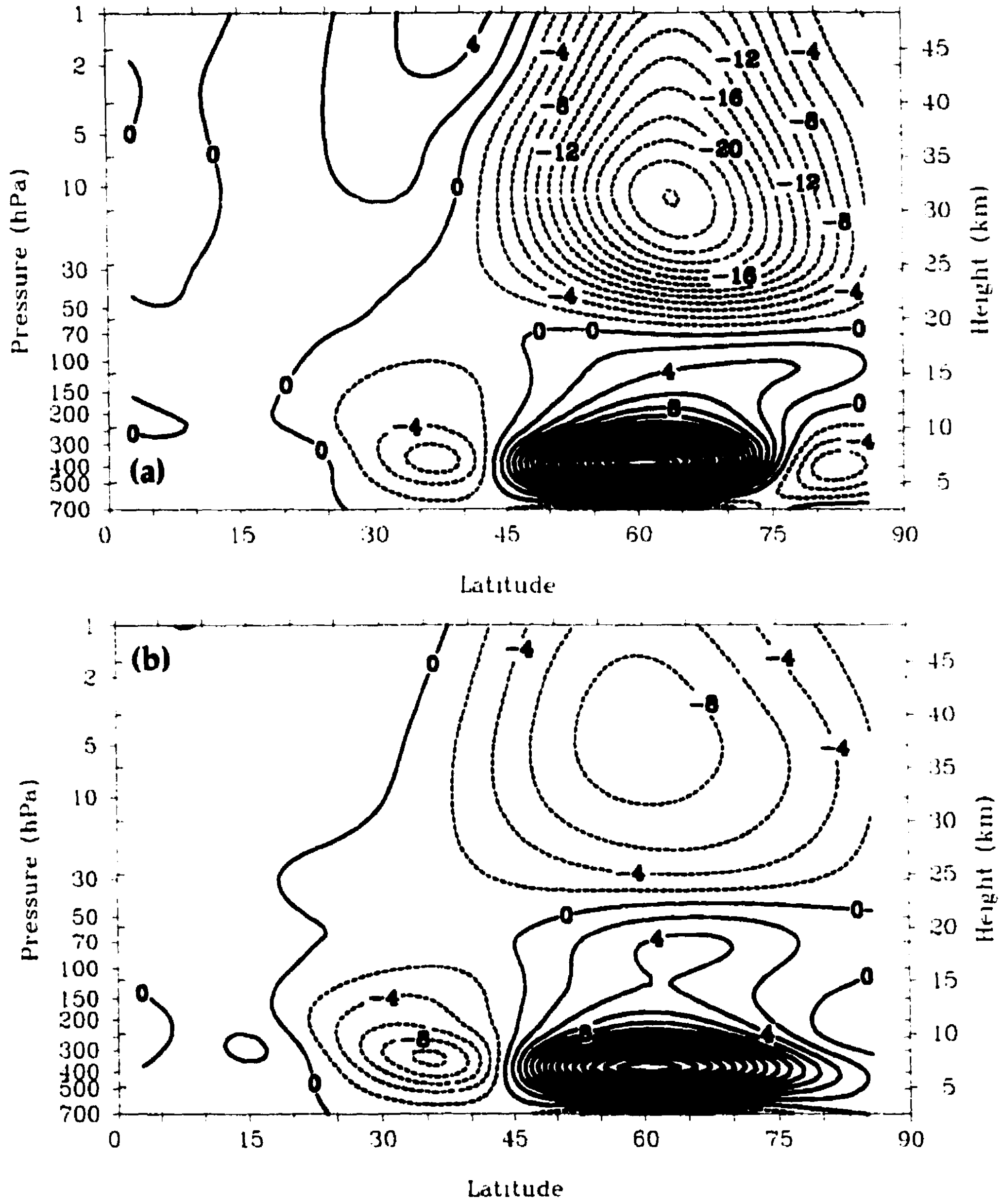

Figure 4.7: First empirical mode (ENM1) of the quasi-geostrophic potential vorticity of wave number 1 Fourier cosine component for **(a)** warming periods and **(b)** non-warming periods. Coutour interval $2\text{x}10^{-6}$ s^{-1}.

not discussed here. There are two large structures in each figure, one located in the middle troposphere (around 400 hPa level and 60°N of latitude) and the other in the middle stratosphere (around 10 hPa and 60°N of latitude). The tropospheric structure during the warming events is more latitudinally focused (extending from 45°N to 75°N) than for the rest of the data set (extending from 45°N to the north pole). There is also a smaller structure in the high latitude region in the figure for the warming events which it is absent in the mode for the rest of the data. In the extratropical region, there is more wave activity in the non-warming periods than in the warming ones. The amplitude of the tropospheric main structure in Fig 4.7a is slightly greater than the one in Fig 4.7b (innermost contours of 36 and 28 units, respectively). We also observe in the extra-tropics at levels 1 and 2 hPa that there is a non negligible QGPV in Fig. 4.7a but not in Fig. 4.7b. This is certainly linked to the large tongue of wave activity associated to the wave breaking in warming events. The amplitude of the stratospheric structure during the warming events is significantly (3 times) larger than during the non-warming periods which shows much more wave activity in the stratosphere during warming events than during normal winter conditions. The variance of the cosine ENM1 of wave number 1 is 30% of the total variance (of the wave number 1 cosine) for the warming and 24% for the non-warming periods, respectively. Figures 4.8a,b and 4.9a,b show the second empirical modal structures (ENM2) of the cosine and sine Fourier components of wave number 1, respectively. The structures in the troposphere of both Fig. 4.8a and b are much the same in both magnitude and location. However in the stratosphere, the cosine figure for the warming events (Fig. 4.8a) exhibits much more wave activity (centred at (65°N, 10 hPa)) than for the non-warming periods. The cosine ENM2 modes explain 19% and 20% of the variance in the warming and non-warming periods, respectively. We have noticed that the large stratospheric amplitudes of both ENM1 and ENM2 cosine wave number 1 for the warming period are located underneath the

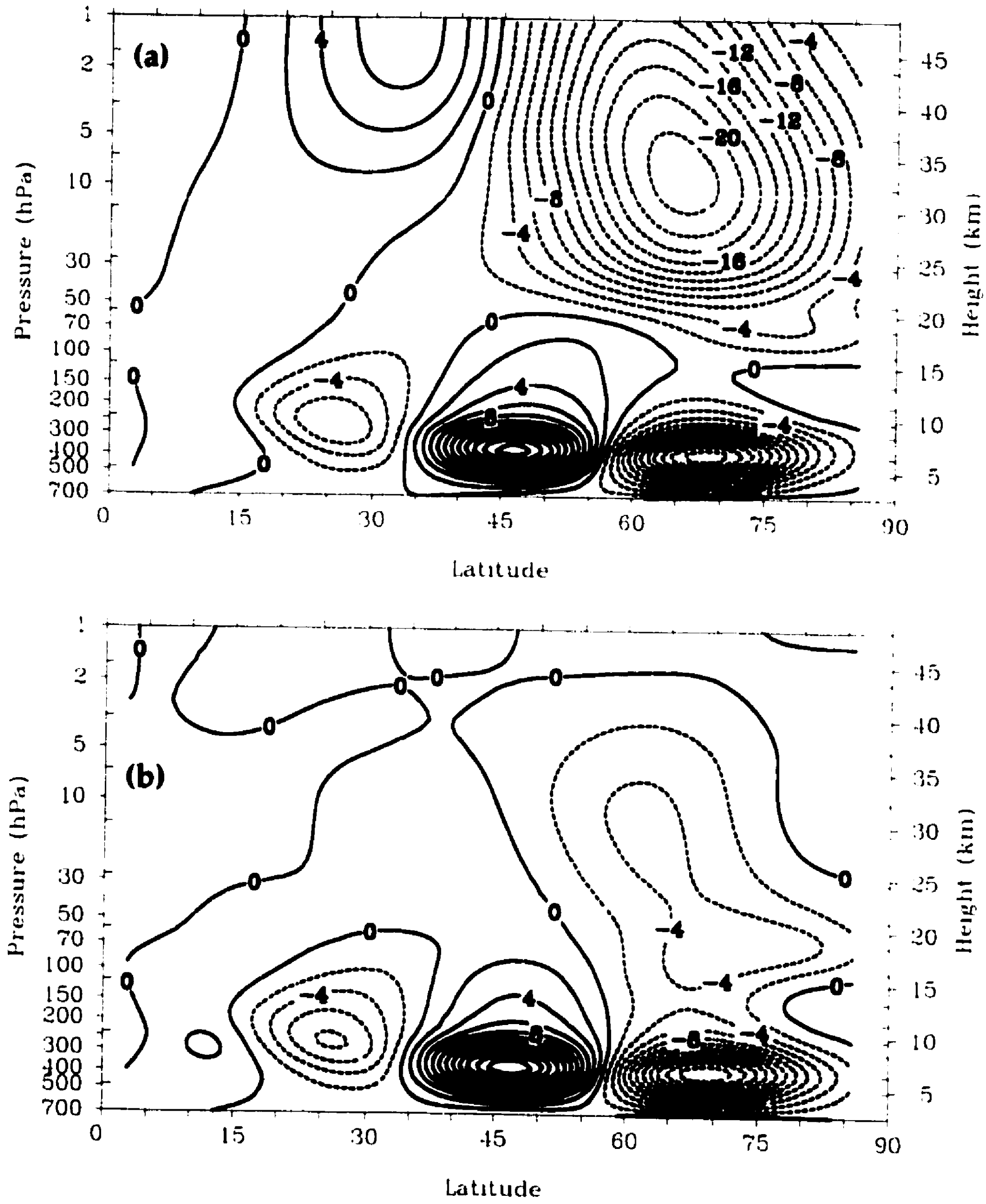

Figure 4.8: Second empirical mode (ENM2) of the quasi-geostrophic potential vorticity of wave number 1 Fourier cosine component for **(a)** warming periods and **(b)** non-warming periods. Coutour interval 2x10^{-6} s^{-1}.

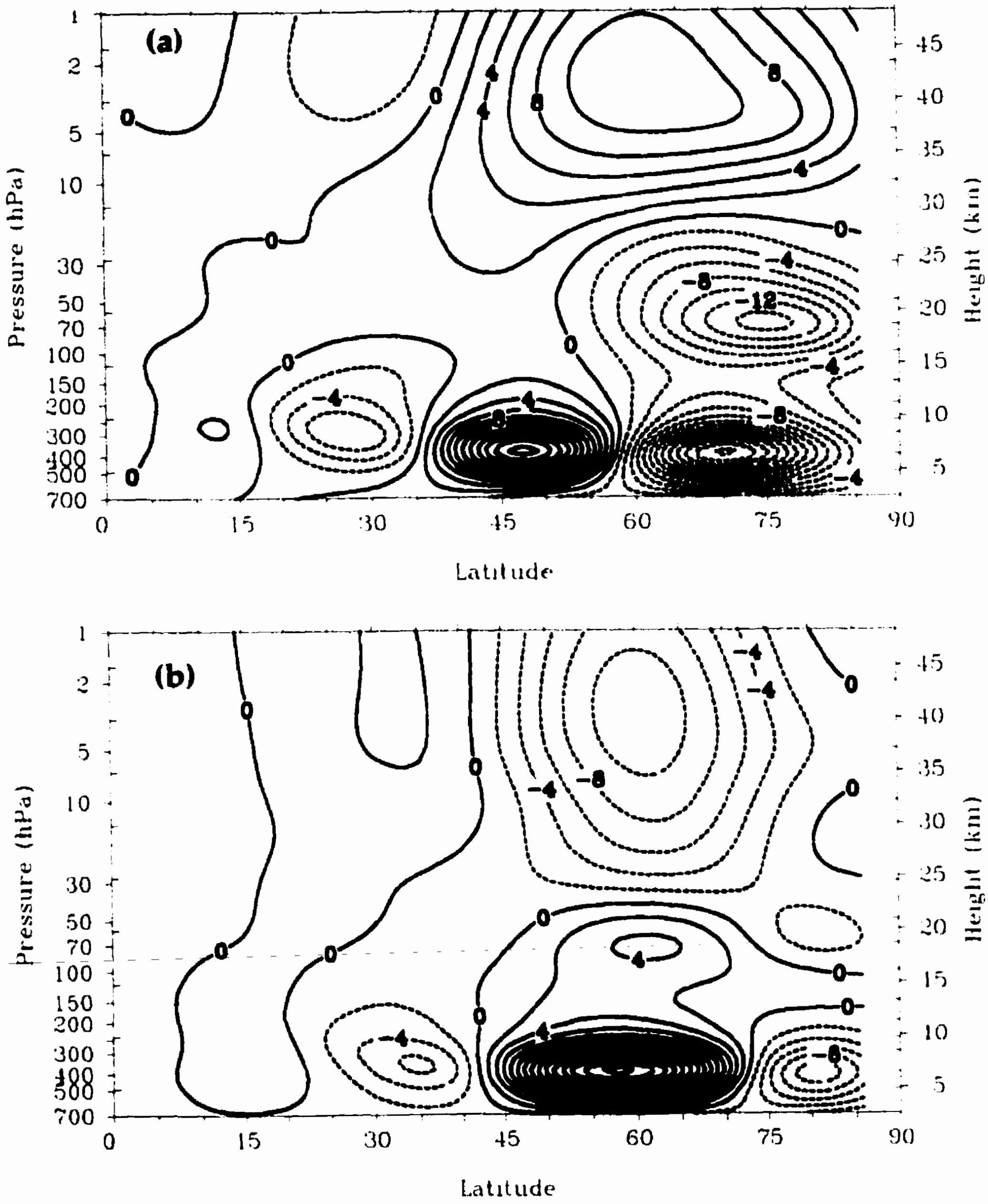

Figure 4.9: Second empirical mode (ENM2) of the quasi-geostrophic potential vorticity of wave number 1 Fourier sine component for (**a**) warming periods and (**b**) non-warming periods. Coutour interval $2\text{x}10^{-6}$ s^{-1}.

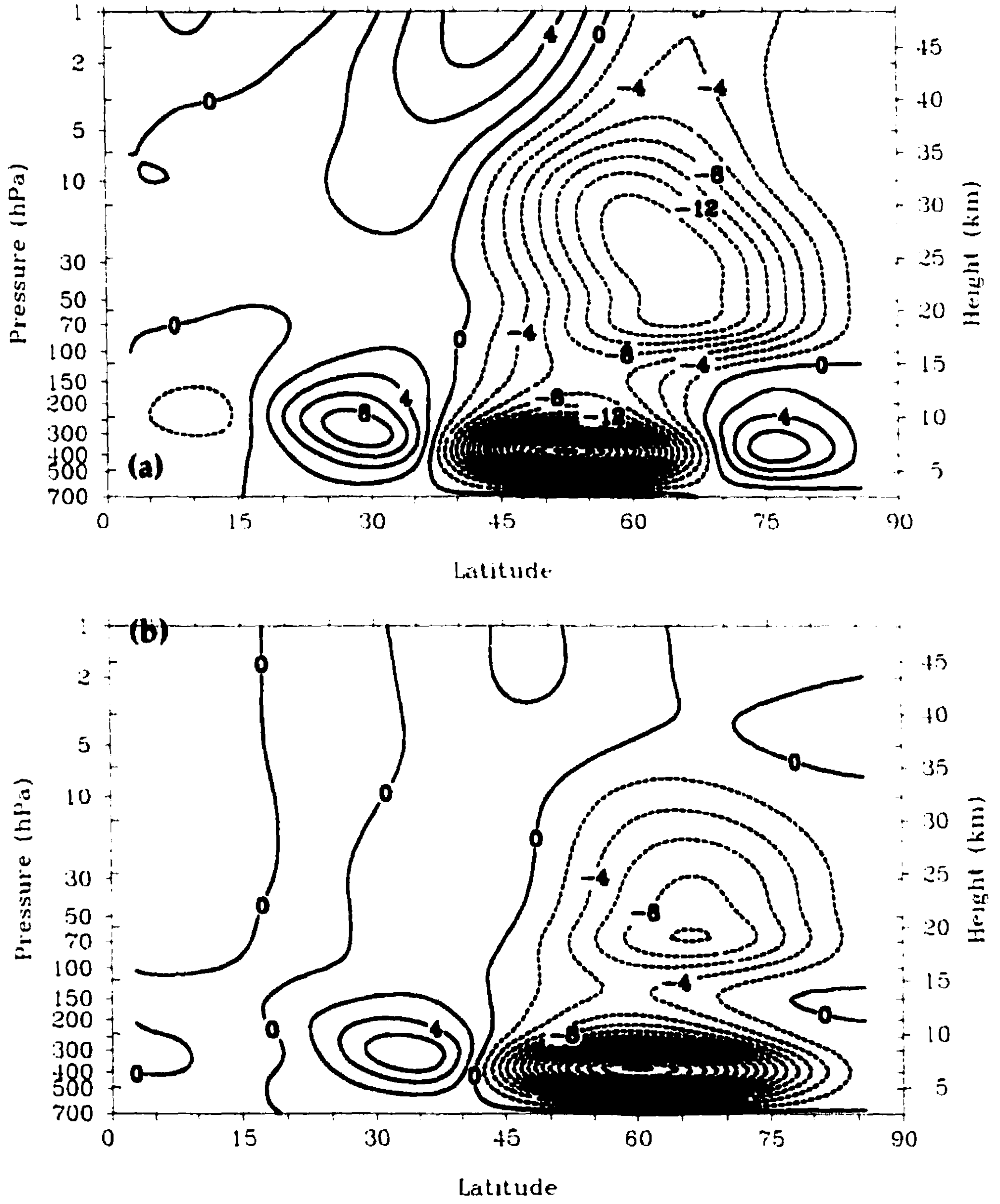

Figure 4.10: First empirical mode (ENM1) of the quasi-geostrophic potential vorticity of wave number 2 Fourier cosine component for **(a)** warming periods and **(b)** non-warming periods. Coutour interval 2x10^{-6} s^{-1}.

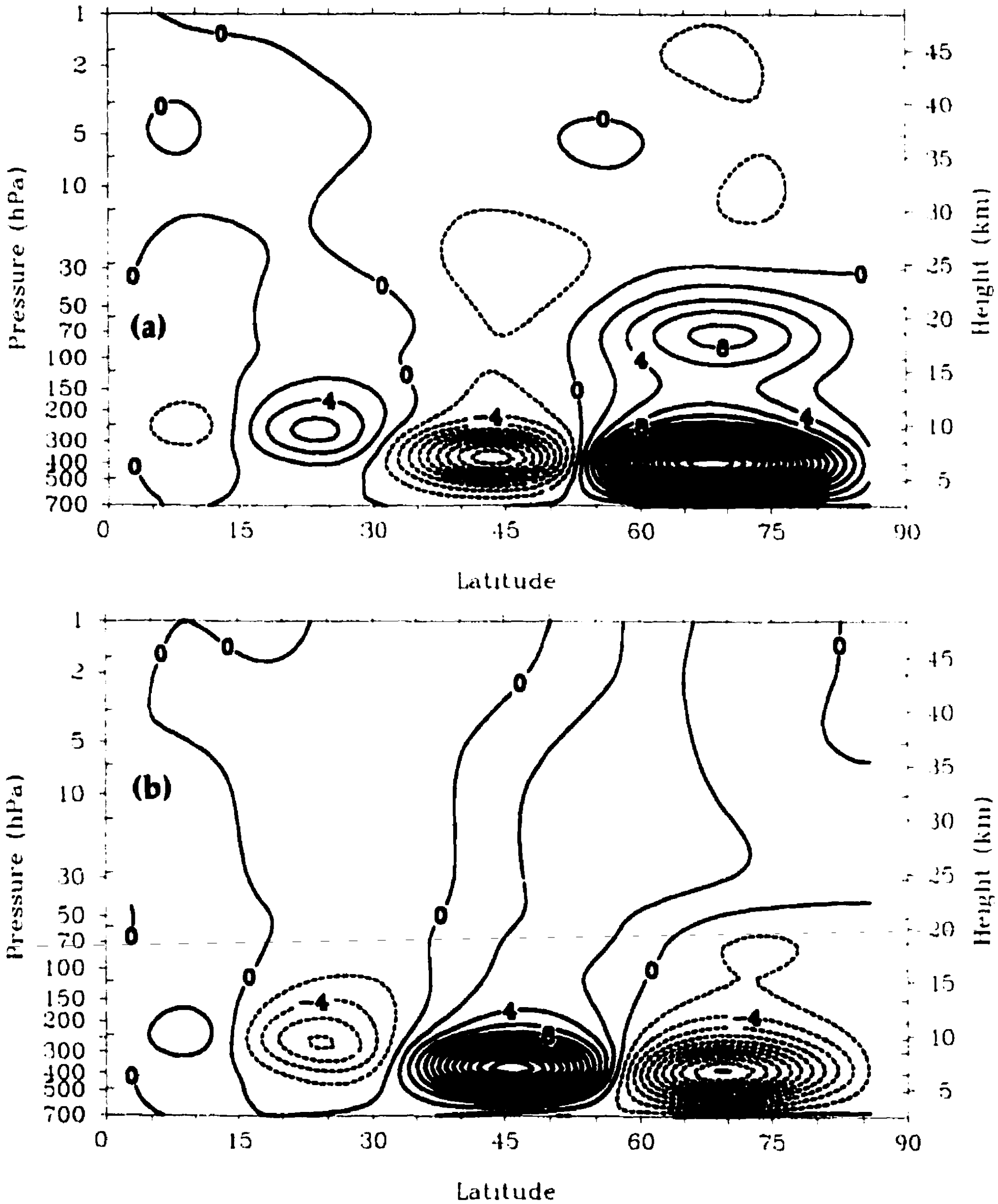

Figure 4.11: Second empirical mode (ENM2) of the quasi-geostrophic potential vorticity of wave number 2 Fourier cosine component for **(a)** warming periods and **(b)** non-warming periods. Coutour interval $2\text{x}10^{-6}$ s^{-1}.

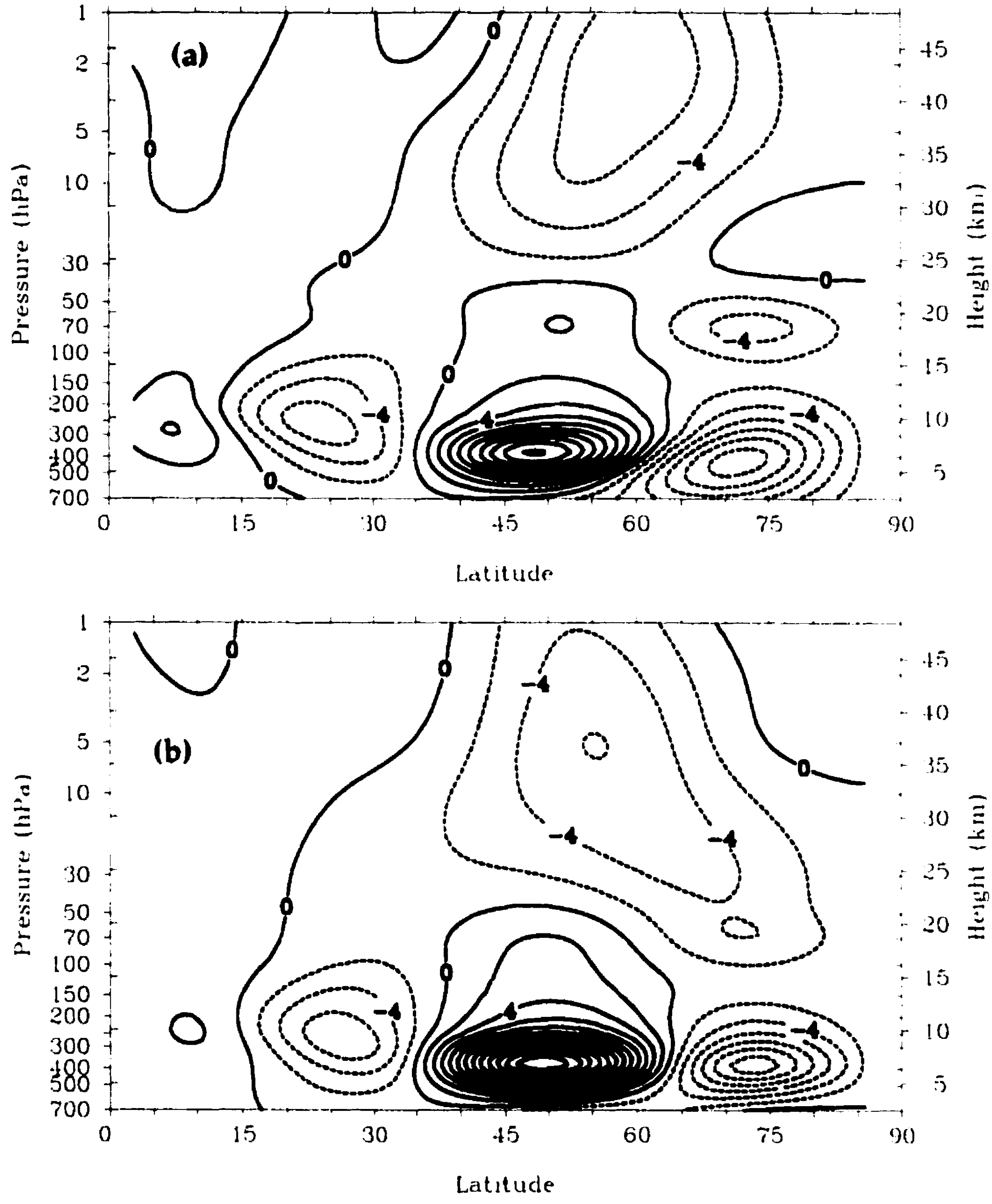

Figure 4.12: Second empirical mode (ENM2) of the quasi-geostrophic potential vorticity of wave number 2 Fourier sine component for **(a)** warming periods and **(b)** non-warming periods. Coutour interval 2×10^{-6} s^{-1}.

(pre-warming) polar night jet (see Fig. 4.2). The second empirical mode of the sine wave number 1 in Figs. 4.9a (warming) and 4.9b (non-warming) are quite different from the cosine wave structures (Figs. 4.8a and b). The high latitude tropospheric structure in Fig. 4.9a centred at (70°N, 400 hPa) is much larger than its counterpart in the non-warming periods at (82°N, 400 hPa) in Fig. 4.9b. The magnitude (10 units) and location (60°N, 3 hPa) of the centre of the upper stratospheric structures are the same in both figures. There is also a structure (14 units) in the lower stratosphere centred at around (75°N, 70 hPa) in the warming figure while it is absent in the non-warming diagram. The percent variance explained by the ENM2 sine wave for the warming and non-warming periods are 22% and 17%, respectively.

Figures 4.10a and b display the first empirical modes of the QGPV for the cosine component of zonal wave number 2 in the warming and non-warming periods. As for the wave number 1 case, the sine Fourier components of the wave number 2 (ENM1) were also analyzed and the results found to be analogous to the cosine component, so we do not include them here. In the troposphere, Fig. 4.10a shows three extrema in the extratropical, middle and high latitude regions. The middle latitude one centred at (52°N, 400 hPa) has the highest amplitude while the other two are much smaller. There are only two extrema in Fig. 4.10b with the main structure centred further North (60°N, 400 hPa) and wider than the main extremum in Fig 4.10a. Both of these main structures are comparable in magnitude. The stratospheric structure during the warming events is again more intense than in the non-warming periods (but not by as much as for zonal wave number 1). The percent variance explained by the ENM1 for warming and non-warming periods are 34% and 32%, respectively. Figure 4.11a and b display the second empirical modal structure (ENM2) of the zonal wave number 2 cosine Fourier component for the warming and non-warming periods, respectively. The extratropical and middle latitude tropospheric structures for the warming and non-warming periods are similar in location, but the amplitude of the high latitude structure centred around (68°N, 400 hPa) for the warming period is almost twice as large as the one in the non-warming period (innermost contours of 38 units in comparison to 20 units). There is no stratospheric structure in the non-warming picture (Fig. 4.11b), but a small structure is found at high latitudes in the lower stratosphere in Fig. 4.11a. For wave number 2, ENM2 explains 21% and 22% of the total variance for the warming and non-warming periods, respectively. We also present the results of the second empirical mode of the wave number 2 sine Fourier component for the warming and non-warming periods in Figs. 4.12a and b, respectively. The tropospheric structures are similar in both figures except that the main middle latitude structure in Fig. 4.12b is more intense than in Fig. 4.12a (innermost contour of 24 and 18 units, respectively). Unlike the wave number 2 cosine Fourier component, the sine wave has a few small amplitude structures in the stratosphere. These stratopheric structures have similar magnitudes and locations for both warming and non-warming periods. Figures 4.12a and b explain, respectively, 18% and 20% of the total variances for each period. In the comparison between wave number 1 and 2 for both warming and non-warming periods, we observe that the centres of the stratospheric structures are lower in altitude for wave number 2 than for wave number 1. This is consistent with the Charney-Drazin result (Section 1.1) that wave number 1 can penetrate higher into the stratophere than wave number 2. If wave activity in the troposphere "causes" the sudden stratospheric warming events, then based on the ENM analysis we have found that there is more wave activity in the tropospheric polar region, especially in the first ENM, during the warming periods than in the normal winter years. Of course the position of the polar night jet in the stratosphere also plays an important role in directing the upward propagating waves to the polar regions of the middle and upper stratosphere.

As mentioned earlier in the stratospheric sudden warming Section 1.3, the zonal mean temperature near the pole in the middle stratosphere rises spectacularly and the normal westerly zonal mean wind tends to decelerate, sometimes to the point of becoming easterly during the warming event. For example, Figure 1.4b shows that the temperature gradient starts to rise on Dec. 28, 1984 and reaches a peak on Jan. 1, 1985, at which time the zonal mean wind reaches its minimum value. According to the zonal mean wind tendency equation (4.21), the eddy forcing term on the right-hand side, ($\nabla \cdot \mathbf{F}/a\rho\cos\phi$), should act as a negative force in order to reduce the zonal mean wind during the growing stage. Here the growing stage is defined as the period between the time when the temperature starts to rise and the time when it reaches its peak. In the above 1984/85 warming event the growing stage is the period from Dec. 28, 1984 to Jan. 1, 1985 inclusively. Apart from the residual circulation fv^* this forcing term represents the zonal mean wind acceleration. The eddy forcing term is indirectly calculated from the results of the ENM analysis by using the generalized Eliassen-Palm theorem,

$$\frac{1}{a\rho\cos\phi}\nabla\cdot\mathbf{F} = -\frac{1}{a\rho\cos\phi}\frac{\partial \mathcal{A}}{\partial t}. \qquad (4.23)$$

Since the wave activity, $\mathcal{A}$, is decomposed into empirical modes (from the ENM analysis), we check the convergence of the sum of the empirical mode contributions to the forcing by computing the ratio

$$\epsilon_F = \frac{<(\nabla\cdot F_{N+1})^2>}{\sum_{i=1}^{N} <(\nabla\cdot F_i)^2>} \qquad (4.24)$$

where N is the number of modes and the angle brackets denote the domain integration. Figures 4.13a and b show contours of the time average of the forcing term for wave numbers 1 and 2, respectively, for the growing stage. Four empirical modes are needed in Fig. 4.13a to make $\epsilon_F < 0.1$ while only three modes are needed in Fig. 4.13b. During the growing stage of the warming, the wave number 1 eddy forcing in Fig. 4.13a exhibits a large negative force (innermost contour of -4.5 $\mathrm{ms^{-1}day^{-1}}$) in the high latitude regions of the upper and middle stratosphere. The centre of this negative force

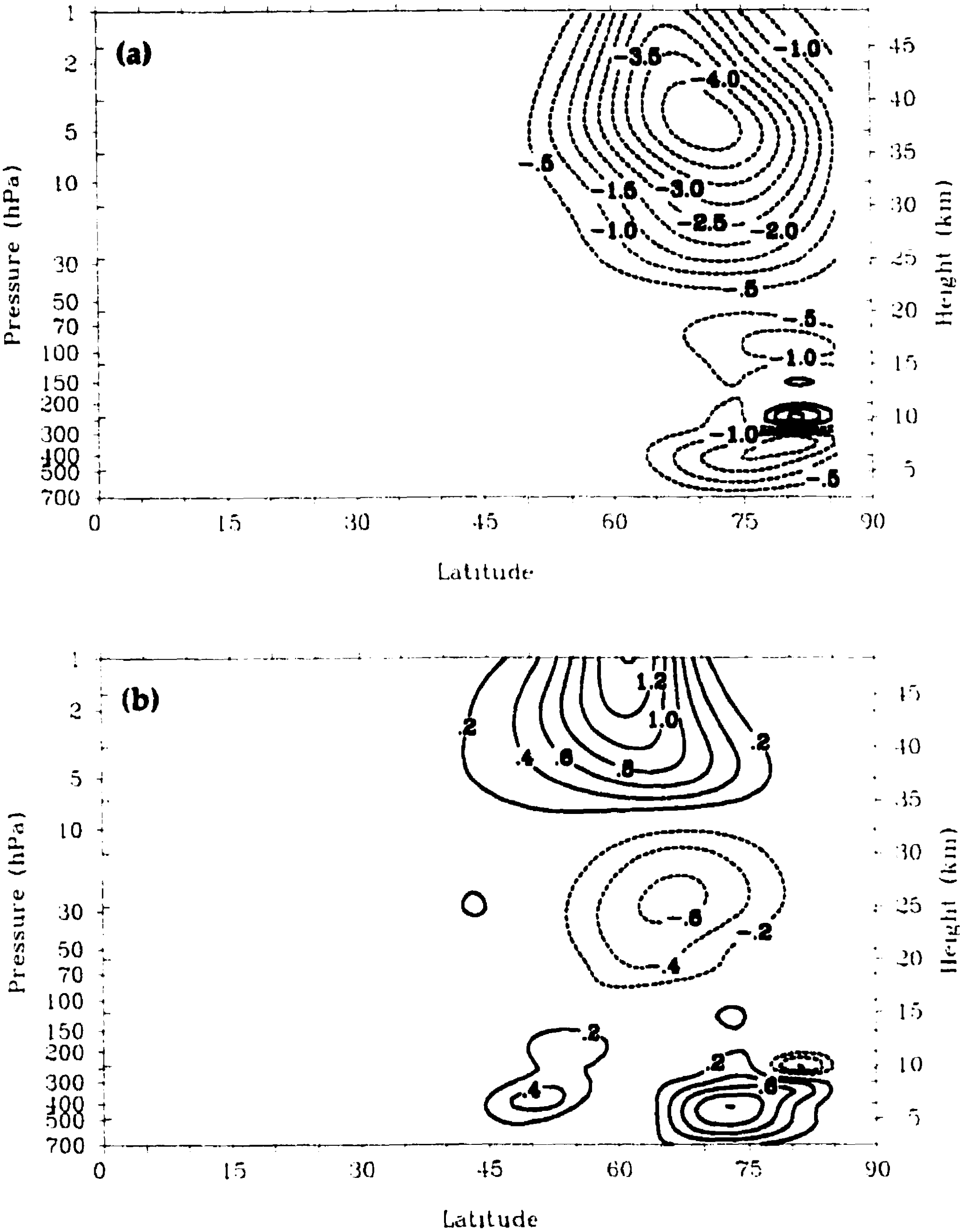

Figure 4.13: Contours of the time average of forcing term $(\nabla\cdot \mathbf{F})/(a\rho\cos\phi)$ (right-hand side of (4.21)) during the growing stage of the warming for (**a**) wave number 1 (first 4 ENMs) and (**b**) wave number 2 (first 3 ENMs). The contour interval is 0.5 and 0.2 ms^{-1}day^{-1} in (a) and (b), respectively.

is just below the pre-warming (Fig. 4.2) zonal mean wind maximum and obviously will reduce the normal westerly zonal wind. There are also two smaller negative forces in the high latitude regions in the middle troposphere and lower stratosphere and an unimportant positive force in the upper troposphere polar region. Figure 4.13b indicates that the eddy forcing for wave number 2 is much weaker than for wave number 1. There is a positive force centred around 60°N in the upper stratosphere and lower mesosphere (the layer above the stratosphere) with an innermost contour of 1 $ms^{-1}day^{-1}$, a negative force in the vicinity of (65°N, 30 hPa) of $0.6ms^{-1}day^{-1}$ and a few relative weak centres in the troposphere.

We next discuss the phase diagram showing the time series of the cosine and sine Fourier components of the QGPV (also the time series of the wave vector). In this type of diagram, the horizontal and vertical axes represent the amplitudes of the cosine and the sine waves, respectively. In other words, the radius (the distance from the origin) represents approximately the zonal wave amplitude. By using the density estimation function in (4.11), we can find the probability density (with $\alpha_i = 1$) and the estimated time tendency for each empirical mode. Notice that the axes are normalized from -1 to 1 and the integrated probability density over the area is unity. The tendency is represented in a polar coordinate system so that it has two (vector) components. The radial component exhibits the growth of the mode and the angular component shows the rotation or phase speed where a counterclockwise rotation represents an eastward wave propagation. Scales of tendency vectors are shown in each figure. The upper left corner scaling arrow represents the QGPV growth in unit of s^{-1} per day while the lower left corner arrow exhibits the phase speed in unit of degree of longitude per day.

Figure 4.14a is the composite diagram of the probability density (contour lines) and the tendency (vectors) of the ENM1 for the growing stage of the warming periods, i.e., for phase during which $\Delta\overline{T} = \overline{T}_{80N} - \overline{T}_{50N}$ is increasing. This phase space diagram can be interpreted as follows: if the point chosen is in the first quadrant then the principal components of both the sine and cosine are positive and these values are averaged over the growing period. In the same quadrant, if the point chosen is close to the origin (small amplitude wave) then the wave propagates eastward without changing its amplitude. However, for the larger wave (further from the origin), the wave's amplitude increases while it propagates eastward. The solid contours give the probability density, which shows how often the wave is found at that point in the diagram. The amplitude of the wave is given by the distance to the origin. The amplitude in this type of diagram is normalized to have a maximum value of $\sqrt{2}$ since each coordinate ranges from -1 to +1. For the absolute value of the wave amplitude, one needs to construct a diagram such as Fig. 4.14b. We observe that the maximum density is shifted to the left from the origin which indicates that when the zonal temperature is rising, the first empirical mode of the wave number 1 has a preferred phase, e.g., the high/low value of geopotential height/QGPV usually appears along the date line at 10 hPa during the warming periods (the Aleutian High). An eastward phase speed (counterclockwise) is clearly seen in this figure. The outward radial components of the tendency are found in the first and second quadrants to indicate the amplification of the ENM1 amplitude during the growing stage of the warming in these areas. In the first half of the third quadrant, the radial components point outward when the amplitude is large (further from the origin) and inward when its amplitude is smaller. In the second half of the third quadrant and the fourth quadrant, the radial components of the tendency vector is directed inward implying an amplitude decay. Overall we observe that during the warming periods near the North Pole at 10 hPa, the amplitude of the first empirical mode is not always amplifying. This might come from the fact that in some warming years (of the nine warming years) the involvement of the wave number 1 is much less important than that of wave number 2, e.g., winter 1984/85. The amplitude of the less important wave may not always synchonize with the temperature during the growing stage. It is interesting to note that in the first quadrant where the amplitude of the empirical mode grows at the greatest value, the fastest phase speed is also found there.

Using the centre of the probability density (the most probable) position in Fig. 4.14a as the mean position of the phase, along with the first empirical modal structures, e.g., using Fig. 4.7a for the cosine Fourier component for ENM1 and the other structure for the sine component (not shown), we construct the QGPV for the growing stage of the warming at the 10 hPa pressure level in Fig. 4.14b. Recall that the winter climatological QGPV in Fig. 4.3 has a high centre off the pole along the Greenwich meridian. If we superpose Fig. 4.14b on the winter climatological figure, we observe the higher value of QGPV on the right-half and the lower value on the left-half. This composite picture implies that during the growing phase of the warming, the polar vortex is further displaced from the pole along the Greenwich meridian due to the poleward movement of the Aleutian High (low value of the QGPV).

In contrast to the growing stage, the decaying stage is defined as the period where the 10 hPa zonal temperature gradient from 50°N to 80°N goes from a maximum value to zero. These two stages makes up the warming data set. Similar to the growing stage we construct the phase space diagram for the decaying stage for the first empirical mode (ENM1) of wave number 1. Notice that these two stages have the same modal structures but different time series. Figure 4.15a shows the probability density and the tendency vectors as in Fig. 4.14a. We first note that during the cooling stage ENM1 has no preferred phase, i.e., the centre of the probability density contour is located almost at the origin of the graph. The radial component of the tendency points towards the origin almost everywhere in the diagram indicating that the amplitude of the ENM1 decreases with time. We see that the higher wave amplitudes (further from the origin) have a strong damping, especially in the first quadrant and the area extending from second half of the second quadrant to the first half of the third

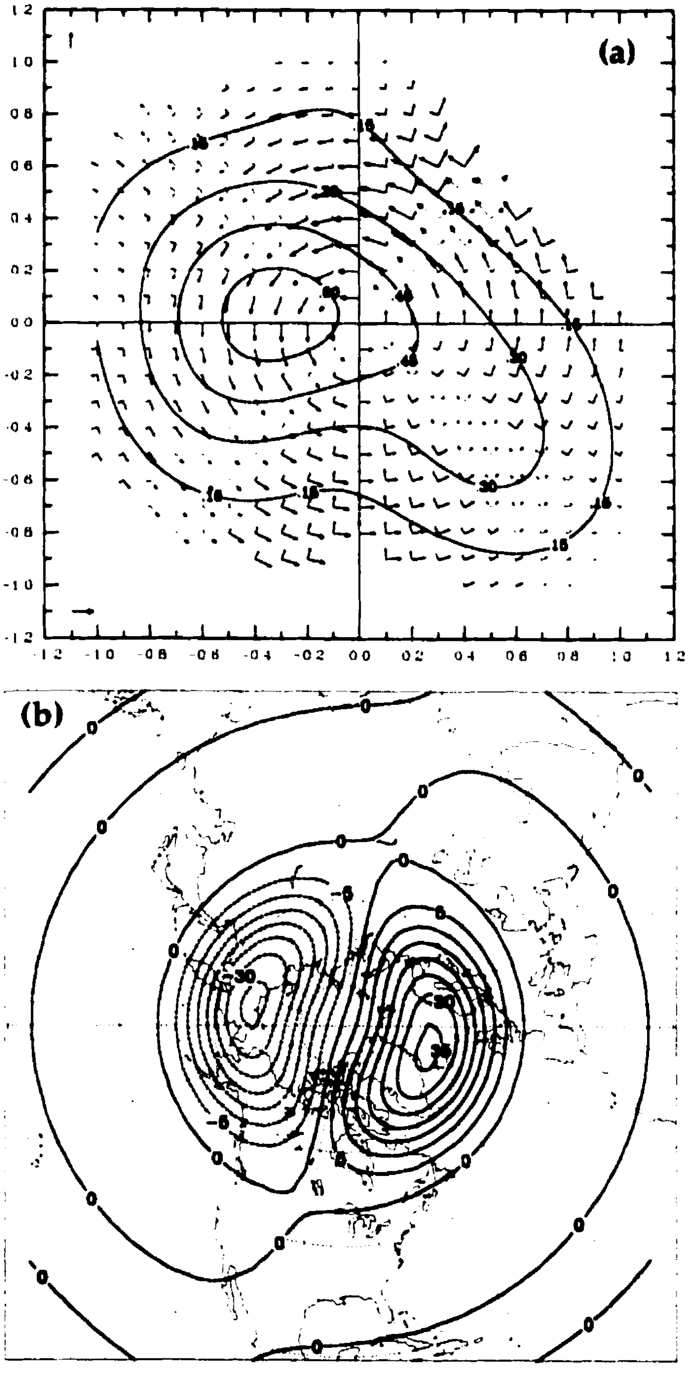

Figure 4.14: First empirical mode (ENM1) of wave number 1 for the growing stage (**a**) contours of the probability density and tendency vectors (upper left: growth scale vector of 3x10^{-6} s^{-1} day^{-1}, lower left: rotational scale vector of 10° longitude day^{-1}) and (**b**) the constructed quasi-geostrophic potential vorticity at the 10 hPa pressure level (contour interval 5x10^{-6} s^{-1}).

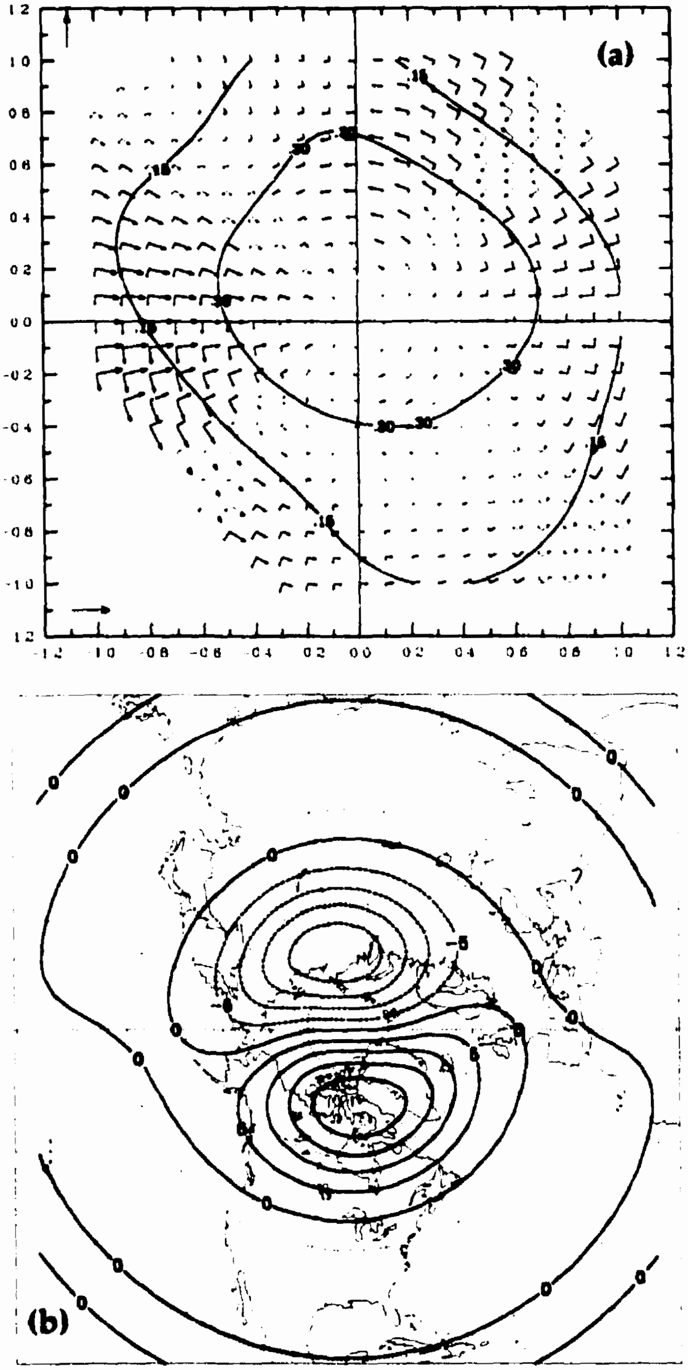

Figure 4.15: First empirical mode (ENM1) of wave number 1 for the decaying stage (**a**) contours of the probability density and tendency vectors (upper left: growth scale vector of 3×10^{-6} s^{-1} day^{-1}, lower left: rotational scale vector of 10° longitude day^{-1}) and (**b**) the constructed quasi-geostrophic potential vorticity at the 10 hPa pressure level (contour interval 5×10^{-6} s^{-1}).

quadrant. This damping seems to increase linearly in the radial direction which could be consistent with a fixed damping rate like we would expect to have for a radiative cooling (Andrews *et al.* 1987 Section 2.5). Eastward propagation (counterclockwise) is found in this mode from the angular component. Similar to the growing mode of ENM1, the decay in the cooling stage has a positive correlation with the phase speed. We also constructed the 10 hPa QGPV which is shown in Fig. 4.15b. Even though the phase from this diagram is not meaningful (the structure can be rotated around the North Pole without loss of generality), it does exhibit that the mean amplitude of the decaying stage is smaller than for the growing stage (innermost contours of 20 vs. 35 units). The contours of the ENM1 probability density are more highly concentrated in Fig. 4.14a than in Fig. 4.15a (innermost contour values of 0.6 vs. 0.3) which implies that the horizontal (time) mean structure for the growing stage is more meaningful than in the decaying one.

Similar to the ENM1 growing stage in Fig. 4.14a, Figure 4.16a exhibits the probability density and the tendency for the empirical modal structures (ENM2) of wave number 1. We see that the centre of the probability density is not far from the origin so that the preferred phase is not as clear as in Fig. 4.14a. The outward radial components everywhere in Fig. 4.16a of the tendency vector obviously demonstrate an amplitude growth of the mode. The counterclockwise rotation of the angular component represents an eastward wave propagation except for a small area of slow westward propagation in the second and fourth quadrants. Figure 4.16b displays the constructed horizontal QGPV at 10 hPa based on its most probable phase position for the second growing mode. Similar to the first empirical mode in Fig. 4.14b, we found negative contours of the QGPV on the left half and positive value on the right half in this figure. Again, if we superpose this second modal structure on the top of the climatological QGPV and the first growing mode (Fig. 4.14b) then the composite picture would have lesser QGPV on the left half and greater on the right half. In

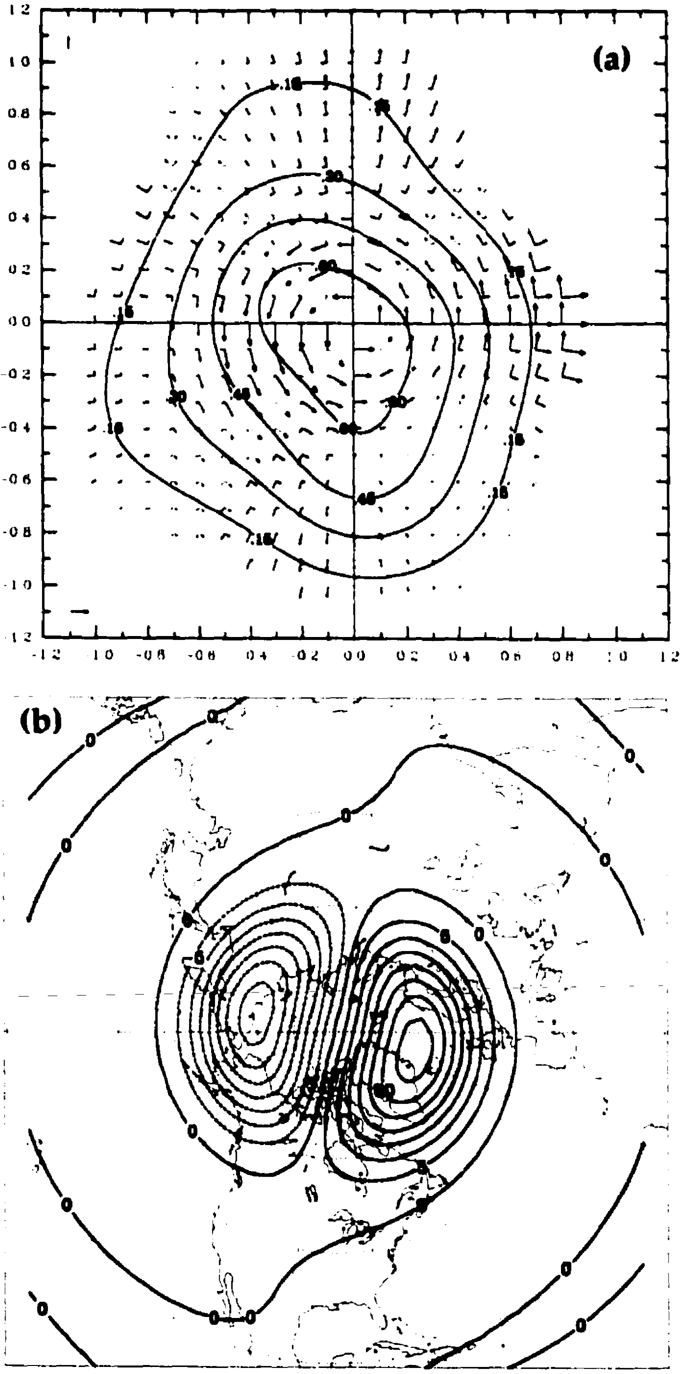

Figure 4.16: Same as Figure 4.14 but for second empirical mode (ENM2).

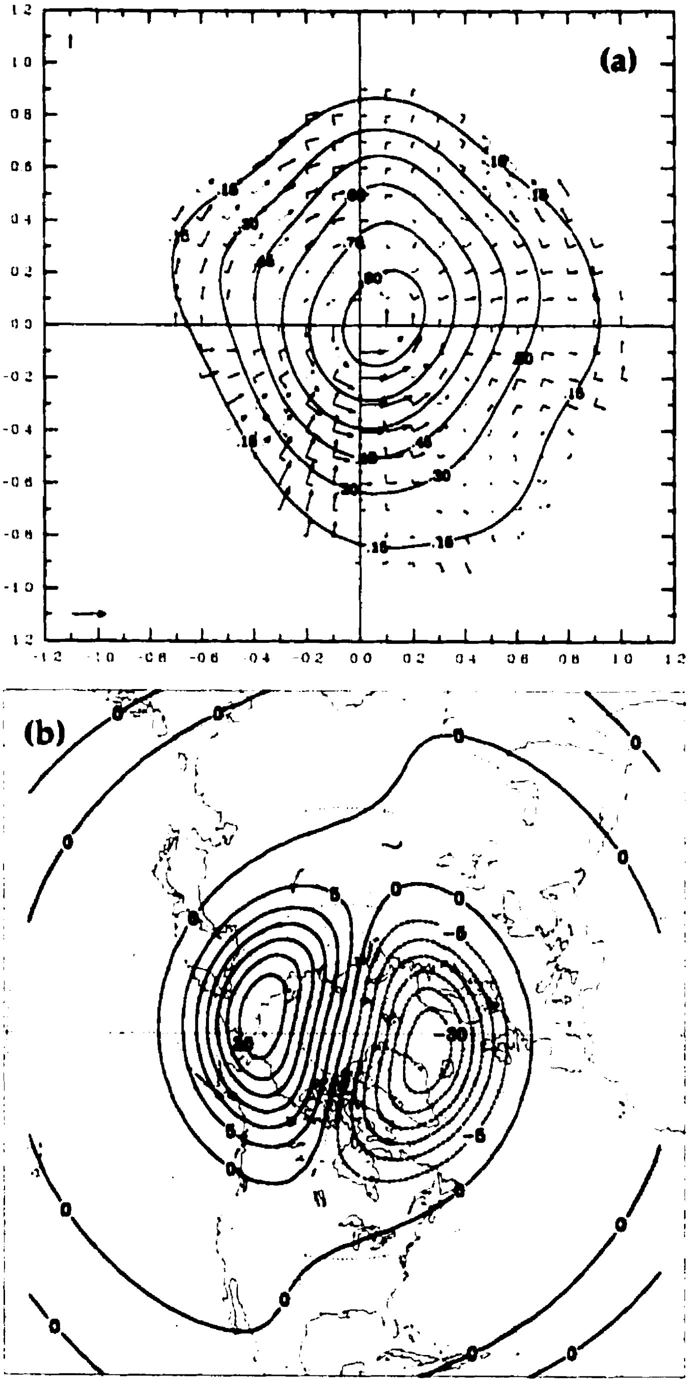

Figure 4.17: Same as Figure 4.15 but for second empirical mode (ENM2).

other words, the polar vortex (the high centre of the QGPV) tends to shift to the right along the Greenwich meridian. Thus, during the growing stage of the warming, in the statistical sense, the polar vortex is pushed off its normal position along the Greenwich meridian. This is consistent with the observed northward movement of the Aleutian High during warming periods. Since the innermost contours of the the probability density of both ENM1 and ENM2 during the warming phase are relatively high (0.6), the mean phase positions (or horizontal QGPV structures) are meaningful.

The tendency and probability density for the decay stage of the second empirical mode of wave number 1 are shown in Fig. 4.17a. Both radial and angular components of the tendency vectors are quite complicated in this empirical mode. We first note a relatively large inward radial components in the third quadrant indicating an amplitude reduction of the ENM2 with time. The eastward phase speeds are mostly found in the same area. In the second quadrant, the growth is negligible and the westward wave propagation is detected in most area. The eastward phase speeds are considerable when the amplitude is small in the first half of the fourth quadrant. The constructed horizontal QGPV in Fig. 4.17b shows a much larger amplitude than for the decaying ENM1 (this amplitude is comparable to the growing modes). The decaying ENM2 QGPV structure has negative contour lines on the right half of the figure and positive on the left half. This decay ENM2 figure has an opposite sign of the growing modes ENM1 and ENM2 which implies a restoring of the polar vortex along the Greenwich meridian or a pushing of the Aleutian High southward back to its normal position. In contrast with the ENM1 mode during the decay phase, this ENM2 mode has a remarkable high probability density value (innermost contour line of 0.9) which makes the constructed horizontal QGPV noteworthy.

We now discuss the results of the ENM analysis for wave number 2. The difference between phase space diagrams of wave numbers 1 and 2 is that in the phase space diagram of wave number 1, the positive x-axis represents the longitudes of 0° and 360°.

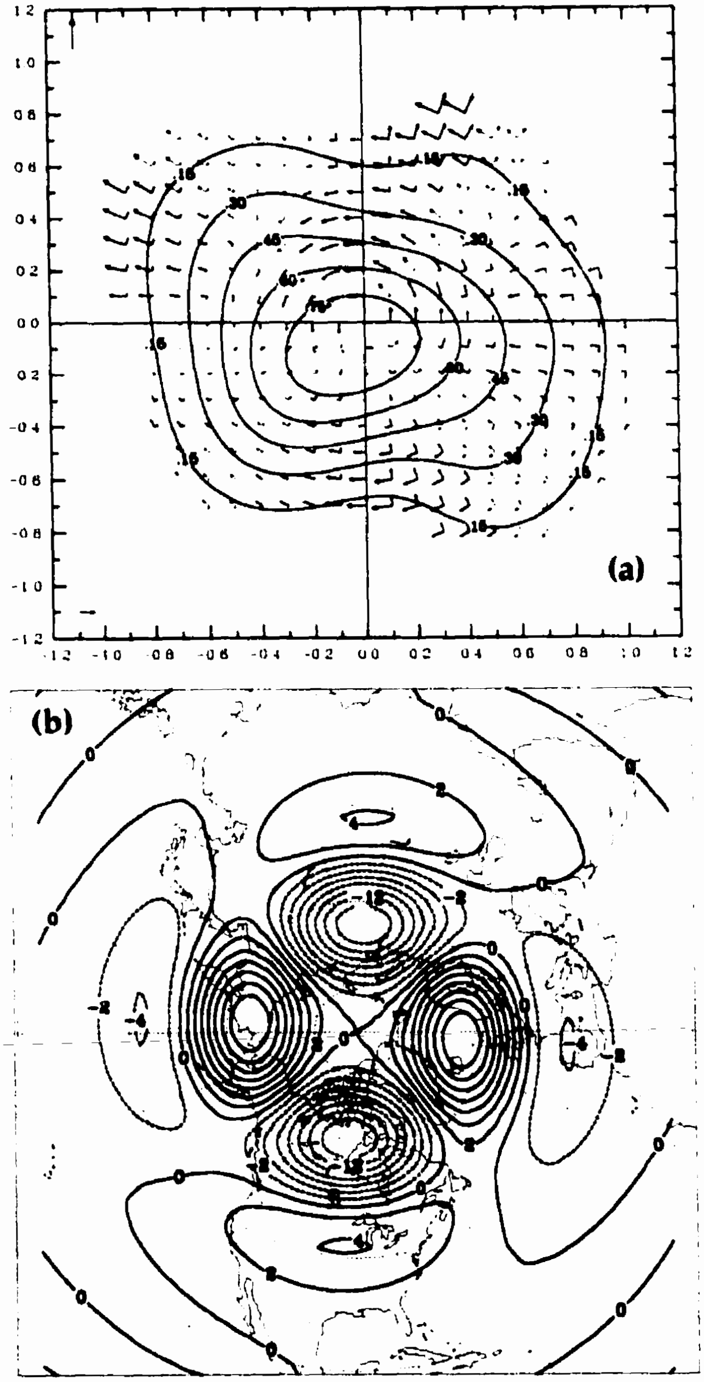

Figure 4.18: First empirical mode (ENM1) of wave number 2 for the growing stage (**a**) contours of the probability density and tendency vectors (upper left: growth scale vector of $3\text{x}10^{-6}$ s^{-1} day^{-1}, lower left: rotational scale vector of 10° longitude day^{-1}) and (**b**) the constructed quasi-geostrophic potential vorticity at the 10 hPa pressure level (contour interval $5\text{x}10^{-6}$ s^{-1}).

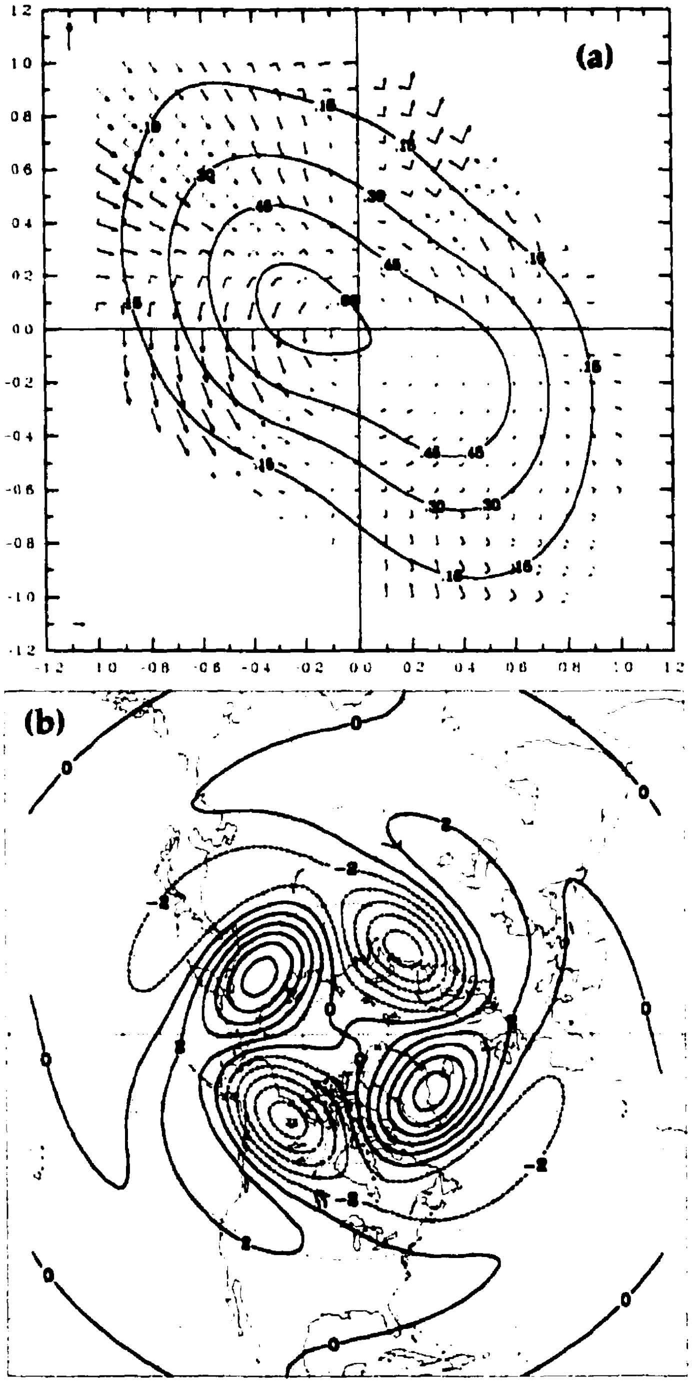

Figure 4.19: First empirical mode (ENM1) of wave number 2 for the decaying stage (**a**) contours of the probability density and tendency vectors (upper left: growth scale vector of 3×10^{-6} s^{-1} day^{-1}, lower left: rotational scale vector of 10° longitude day^{-1}) and (**b**) the constructed quasi-geostrophic potential vorticity at the 10 hPa pressure level (contour interval 5×10^{-6} s^{-1}).

while in the wave number 2 figure, this horizontal axis shows the longitudes of 0° and 180°. More generally, the positive x-axis represents the longitudes of 0° and $360°/k$ where k is the zonal wave number. Figure 4.18a exhibits the probability density and the tendency of the first empirical mode (ENM1) for the growing stage of the warming events. The centre of probability contours is shifted into the third quadrant, between the longitude of 90° (or 270°) and 135° (or 315°), from the origin. Relatively large outward radial components in the second half of the first quadrant and the second half of the second quadrant, where the amplitude is larger, but the probability low, are clearly seen in this figure. A less intense decay (inward radial components) is also found in other areas in Fig 4.18a. An eastward phase speed of order of 10 degrees longitude per day or higher is observed in the first two quadrants where the amplitude is small and in the large amplitude second half of the first quadrant. A slower westward rotation is detected in other areas except the high amplitude first half of the fourth quadrant where the westward phase speed of order of 10 degrees per day. Figure 4.18b shows the constructed horizontal QGPV structure based on the centre of the probability density in Fig. 4.18a. We notice that the amplitude of the empirical mode is about one-half of that for the wave number 1 growing modes.

The probability density and the tendency vectors for the cooling stage of the first empirical mode of wave number 2 are shown in Fig. 4.19a. The amplitude reduction is clearly exhibited in the second quadrant due to large inward radial components of the tendency vectors, especially for the largest amplitudes. A few noticeable outward vector components are found in the large amplitude second half of the first quadrant. Radial vector components in other areas of the figure are small and negligible. A relatively fast eastward wave propagation is found in the first half of the third quadrant. There are also some moderate eastward phase speeds in the large amplitude second half of the first quadrant. Some negligible westward phase speeds also appear in this figure. The constructed horizontal QGPV is shown in Fig. 4.19b. Its amplitude is slightly less than that of the growing mode (Fig. 4.18b).

As seen in Fig. 4.11a, the second empirical mode of zonal wave number 2 has no significant amplitude in the middle stratosphere and so we do not discuss in detail this mode here. However, we present the constructed horizontal QGPV of the ENM2 for the growing and decaying stages in Figs. 4.20a and b, respectively, in order to discuss the phase tilt in these diagrams. Based on a barotropic model with a constant wind shear ($U = Sy$, where U is the zonal mean wind, S is a constant and y is the northward distance), Farrell (1987) has shown that disturbances grow (by extracting energy from the zonal flow) if their lines of constant phase slope opposite to that of the shear. Figure 4.20a clearly exhibits a westward phase tilt (against the wind shear) during the growing stage of the warming. The empirical mode amplifies during this period, according to Farrell, by extracting energy from the zonal flow. In constrast to the growing stage, the decaying stage horizontal QGPV shown in Fig. 4.20b has an opposite (eastward) phase tilt. This means that the disturbance gives back its energy to the zonal flow and its amplitude will be reduced. The phase tilts in Figs. 4.20a and b are resulted from the different structures at 10 hPa (see also Figs. 4.11a (cosine structure) and 4.12a (sine structure)) and the phase (of the most probable position) difference between the growing and decaying modes. As mentioned above, the amplitude of the zonal wave number 2 ENM2 is much smaller than that of the ENM1 of the wave number 2 or of the other two empirical modal structures of zonal wave number 1, so that the phase tilt discussion makes its role somewhat less important in comparison to the other. Since the second empirical mode has a higher amplitude in the lower stratosphere (see Fig. 4.11a), we have also constructed the horizontal QGPV at this level (70 hPa, not shown) instead of 10 hPa and the result showed no phase tilt at this level.

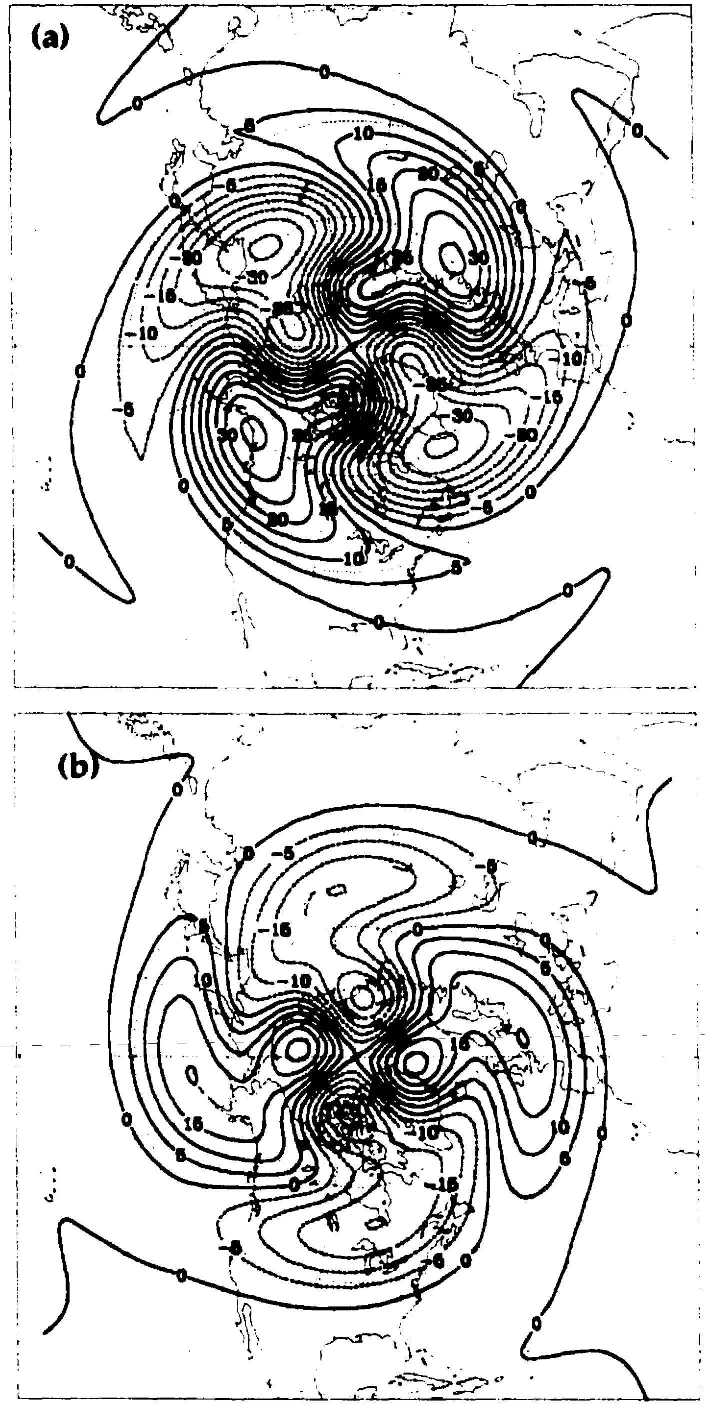

Figure 4.20: The constructed quasi-geostrophic potential vorticity at the 10 hPa pressure level (contour interval $5\text{x}10^{-7}$ s^{-1}) of second empirical mode (ENM2) of wave number 2 for the **(a)** growing stage and **(b)** decaying stage.

Chapter 5

Summary and Conclusions

In this thesis we have used the Empirical Normal Mode Analysis technique to analyze data from a Shallow Water Model as well as 3-dimensional atmospheric data, with a focus on stratospheric sudden warming events.

The Empirical Normal Mode Analysis is an extension of the Empirical Orthogonal Function Analysis. This method uses both a statistical technique from the Empirical Orthogonal Function Analysis and a dynamical constraint from the generalized Eliassen-Palm theorem to ensure that modes (from the analysis) are orthogonal to each other and are the solutions of dynamical linearized equations.

We have calculated the normal modes (ENMs) and their associated frequencies from the data generated by a Shallow Water Model (linearized version with a basic state at rest). The results were tested against the theoretical (numerical) solutions provided by Longuet-Higgins and showed that the ENM analysis technique can capture the spatial structures and their frequencies with a great degree of accuracy, especially in long temporal records. The average errors (in periods) for the 2000 and 100 day time series are found to be 1% and 4.6%, respectively. The error grows, as expected, when the time series is shortened since the number of oscillations in the period is smaller. The meridional normal mode structures of the perturbation height and also zonal wind (not shown in the thesis) calculated from the ENM analysis are in good agreement with theoretical results from Longuet-Higgins in all aspects, e.g., location of the peaks, the zero line intersection(s) as well as the way they approach the pole and the equator.

It has been known from observations that the stratospheric polar vortex (from the climatological data) in the Southern Hemisphere during winter (JJA) is fairly zonally symmetric while the Northern Hemisphere winter (DJF) the vortex is distorted and off the pole [see Fig. 1.3a–d]. This suggests that some wave activity propagates upward from the troposphere into the stratosphere due to the ocean-continent thermal contrast and orography (more high mountains in the Northern Hemisphere than in the southern one). Stratospheric sudden warming events are spectacular events during some winters in the Northern Hemisphere. During the warming period the zonal mean temperature in the middle stratosphere near the pole rises dramatically and produces a meridional temperature gradient reversal. Following the abrupt change in temperature, the normal westerly zonal wind decelerates and sometimes reverses and becomes easterly. Not only do the zonal mean temperature and wind change but so do the wave disturbances (mainly zonal wave numbers 1 and 2). Common features observed in the middle stratosphere (10 hPa) are the Aleutian High (high value of geopotential height near 180°W) moving northward, pushing the polar vortex off the pole along the Greenwich meridian (strengthening of wave number 1) and the development of wave number 2 splitting the polar vortex into two separate parts. It is also noticed that the evolution of zonal wave number 1 has a preferred phase (approximately along the 0–180° longitude line) and time (usually at the beginning of the warming) while the occurrence of wave number 2 does not. Another important observed feature that might lead to the stratosphere warming is the position of the polar night jet at the beginning of the warming. The averaged onset polar night jet in Fig. 4.2 is quite different from the 11 year climatological data in Fig. 1.2. The pre-warming polar night jet moves northward and downward to around (68°N,2.5 hPa) from its climatological location in the vicinity of (45°N,0.1 hPa). This position of the polar night jet is believed to guide the (winter) normal upward propagation wave activity to the polar region instead of propagating toward the equator. The "cause" of the polar night jet anormaly is still not quite well understood.

The Empirical Normal Mode analysis was used to characterize the stratospheric warming events. First, we partitioned the winter data set into two parts, namely, the warming events and the rest of the data set. The purpose of this study was to identify the difference in the structures of the quasi-potential vorticity and thus the wave activity by comparing the modes during the warming events with those for the rest of the data. As expected, the wave activity in the stratosphere during warming events is much stronger than that of the non-warming periods, especially for wave number 1 (both ENM1 and ENM2) [see Figs. 4.7 and 4.8]. For wave number 2, however, only the first normal mode clearly exhibits (though the difference is not as large as in wave number 1) this feature [Fig. 4.10]. If the "cause" of the stratospheric warming is the propagation of wave activity from below, then the tropospheric structure of quasi-potential vorticity might be a precursor for warming events. We first notice that the main tropospheric structure for the ENM1 wave number 1 (around 60°N) for warming events is about 28.6% (36 vs. 28 units) larger than same structure in the non-warming periods. There is also a smaller structure in high latitudes in the warming events while this structure is absent in the non-warming data set. For the second normal mode of wave number 1, the tropospheric structures are the same (in magnitude and position) in both periods. This suggests that this mode does not play a significant role in a upward propagation of wave energy.

The tropospheric main structures (around 50-60°N) for wave number 2 (ENM1) are the same in magnitude for both warming and non-warming periods, but the positions and shapes are different [Fig. 4.10]. Again, a small structure in the high latitude troposphere appears during warming events but not in the non-warming periods. By comparing structures between the warming and non-warming periods, we observed that the large stratospheric wave activity during the warming events might be related to the upward propagation of wave activity from the troposphere which appears in the first normal mode (the most important). This would be reflected in their differences in tropospheric structures.

We also investigated the forcing term [equation (4.21)] which is responsible for the zonal mean wind deceleration during the growing stage of the warming events from empirical modes and found that the negative forcing is mainly contributed by wave number 1 and is located near the pre-warming polar night jet as seen in Fig. 4.13a. The much smaller forcing contribution from zonal wave number 2 is not surprising since wave number 2 does not penetrate high into the stratosphere.

We have used the kernel density estimation method to calculate the probability density of normal modes and their tendencies which were displayed in phase space diagrams. The results show that during the growing stage, the modal amplitudes of wave number 1 are growing with eastward phase speeds. In contrast, the modal amplitudes are reduced during the decaying stage with an eastward phase speed found in ENM1 and a more complex phase propagation in ENM2. Neither wave number 1 nor 2 was found to have a meridional phase tilt in the stratospheric high wave activity regions. This implies that the disturbance development during the stratospheric warming periods is not due to barotropic instability. By combining the phase and structure of each empirical mode we constructed 10 hPa maps of the quasi-geopotential vorticity. These charts clearly exhibit the polar vortex pushed off along the Greenwich meridian by the northward movement of the Aleutian High during the growing stage of the warming events. This polar vortex is restored when the zonal mean temperature returns to normal winter conditions.

The ENM analysis, as expected, recovered the Hough modes and their frequencies from the data set generated by the shallow water model because the method itself was derived from the linearized dynamical equations [Section 2.2] and the data set was generated by the same set of equations. The technique accomplished the task remarkably well. In the real 3D atmosphere, the dynamics are not linear, especially during warming events, but the (linearized) ENM analysis method derived in Section 2.3 yielded informative results. The method captured the major features of stratospheric warming events with very few empirical modes.

Appendix A

The proof of 3D primitive equations wave activity conservation

We begin with the perturbation zonal wind and thermodynamic equations linearized about the zonal time mean basic state on a sphere for an inviscid, adiabatic system as

$$\mathrm{D}_t u' - \overline{\eta} v' + \overline{u}_z w' + \frac{\Phi'_\lambda}{a\cos\phi} = 0 \tag{A.1}$$

and

$$\mathrm{D}_t \theta' + \frac{\overline{\theta}_\phi}{a} v' + \overline{\theta}_z w' = 0 \tag{A.2}$$

where

$$\mathrm{D}_t = \frac{\partial}{\partial t} + \frac{\overline{u}}{a\cos\phi}\frac{\partial}{\partial\lambda}, \tag{A.3}$$

the basic state absolute vorticity, $\overline{\eta}$, is

$$\overline{\eta} = f - \frac{(\overline{u}\cos\phi)_\phi}{a\cos\phi}, \tag{A.4}$$

Φ is the geopotential height, θ is the potential temperature, w is the vertical wind component. The overbar and prime denote the basic state (zonal and time mean) and deviation from the basic state of the variable. The subscript (λ, ϕ, z, t) denote the derivative with respect to longitude, latitude, height and time respectively. The Ertel's potential vorticity P is defined as

$$\rho P = \theta_z \left[f - \frac{(u\cos\phi)_\phi}{a\cos\phi} + \frac{v_\lambda}{a\cos\phi} \right] - \frac{\theta_\lambda v_z}{a\cos\phi} + \frac{\theta_\phi u_z}{a} \qquad (\text{A.5})$$

where the density profile, $\rho(z)$, is

$$\rho(z) = \rho_s \exp\left(-\frac{z}{H}\right) \qquad (\text{A.6})$$

with ρ_s being the reference density which is usually taken at 1000 hPa. H ($\equiv$7 km) is the scale height and z is the log-pressure height and is defined in (1.3). The equation (A.6) shows that the atmospheric density decreases by a factor e every 7 km. We can separate (A.5) into the basic state (zeroth order) and the perturbation (first order) as follows:

$$\rho\overline{P} = \overline{\theta}_z\overline{\eta} + \frac{\overline{\theta}_\phi\overline{u}_z}{a} \qquad (\text{A.7})$$

and

$$\rho P' = \frac{\overline{\theta}_z}{a\cos\phi}[-(u'\cos\phi)_\phi + v'_\lambda] + \overline{\eta}\theta'_z + \frac{\overline{u}_z\theta'_\phi}{a} + \frac{\overline{\theta}_\phi u'_z}{a}. \qquad (\text{A.8})$$

For a conservative system (no source or sink) Ertel's potential vorticity is conserved following the material flow (Andrews *et al.* 1987 section 3.1), that is,

$$\mathrm{D}P/\mathrm{D}t = 0 \qquad (\text{A.9})$$

where D/Dt is the material derivative. The linearized form of the above equation can be written as

$$\mathrm{D}_t P' + \frac{\overline{P}_\phi}{a}v' + \overline{P}_z w' = 0. \qquad (\text{A.10})$$

Eliminating w' in (A.2) and (A.10) by operating $[\overline{\theta}_z \times$ (A.10) - $\overline{P}_z \times$ (A.2)$]$ we obtain

$$\mathrm{D}_t[\overline{\theta}_z P' - \overline{P}_z \theta'] + [\overline{\theta}_z \overline{P}_\phi - \overline{P}_z \overline{\theta}_\phi]\frac{v'}{a} = 0. \qquad \text{(A.11)}$$

The above equation can be rearranged as

$$\mathrm{D}_t \Pi' + \frac{\overline{\mathrm{J}}}{\overline{\theta}_z} v' = 0 \qquad \text{(A.12)}$$

where

$$\Pi' = P' - \frac{\overline{P}_z}{\overline{\theta}_z}\theta' \qquad \text{(A.13)}$$

and

$$\overline{\mathrm{J}} = \frac{1}{a}\frac{\partial(\overline{P}, \overline{\theta})}{\partial(\phi, z)} = \frac{1}{a}[\overline{P}_\phi \overline{\theta}_z - \overline{P}_z \overline{\theta}_\phi]. \qquad \text{(A.14)}$$

Multiplying (A.12) by Π' and taking zonal average, after rearranging we get

$$\frac{1}{2}\frac{\partial}{\partial t}\left(\frac{\rho}{\overline{\mathrm{J}}}\overline{\Pi'^2}\right) + \frac{\rho}{\overline{\theta}_z}\overline{v'\Pi'} = 0. \qquad \text{(A.15)}$$

Notice that overbars above the quadratic perturbation terms, e.g., $\overline{\Pi'^2}, \overline{u'v'}$, etc., denote zonal means which are time dependent while overbars above single variables, e.g., $\overline{\theta}, \overline{u}$, etc., denote zonal and time means which are independent of time. Substituting the definition of Π' in (A.13) into the last term of (A.15) we have

$$\frac{1}{2}\frac{\partial}{\partial t}\left(\frac{\rho}{\overline{\mathrm{J}}}\overline{\Pi'^2}\right) = \frac{\rho}{\overline{\theta}_z}\overline{v'\left(P' - \frac{\overline{P}_z}{\overline{\theta}_z}\theta'\right)}. \qquad \text{(A.16)}$$

Taking zonal mean of the operation $\theta' \times$(A.2) and multiplying the result by $\rho(\overline{u}_z/\rho)_z\overline{\theta}^{-2}$ yields

$$\frac{1}{2}\frac{\partial}{\partial t}\left[\frac{\rho}{\overline{\theta}_z^2}\left(\frac{\overline{u}_z}{\rho}\right)_z \overline{\theta'^2}\right] + \frac{\rho}{\overline{\theta}_z^2}\frac{\overline{\theta}_\phi}{a}\left(\frac{\overline{u}_z}{\rho}\right)_z \overline{v'\theta'} + \frac{\rho}{\overline{\theta}_z}\left(\frac{\overline{u}_z}{\rho}\right)_z \overline{w'\theta'} = 0. \qquad \text{(A.17)}$$

The hydrostatic equation is

$$\Phi'_z = \frac{R}{H}\exp(-\kappa z/H)\theta' \qquad \text{(A.18)}$$

where R is the gas constant and $\kappa=2/7$ is the ratio of the gas constant and the specific heat at a constant pressure. To eliminate the geopotential term in the zonal wind equation (A.1) we take $[\partial/\partial z(A.1) - (a\cos\phi)^{-1}\partial/\partial\lambda\ (A.18)]$ and obtain

$$\mathrm{D}_t u'_z + \frac{\bar{u}_z}{a\cos\phi}u'_\lambda - \bar{\eta}_z v' - \bar{\eta}v'_z + \bar{u}_{zz}w' + \bar{u}_z w'_z + \frac{R}{H}\frac{1}{a\cos\phi}\theta'_\lambda = 0. \tag{A.19}$$

By using the mass continuity equation

$$\frac{1}{a\cos\phi}[u'_\lambda + (v'\cos\phi)_\phi] + \frac{1}{\rho}(\rho w')_z = 0 \tag{A.20}$$

to eliminate the term w'_z in (A.19) we obtain

$$\begin{aligned}\mathrm{D}_t u'_z - \frac{\bar{u}_z}{a\cos\phi}(v'\cos\phi)_\phi - \left(\frac{\bar{\eta}}{\rho}\right)_z \rho v' - \frac{\bar{\eta}}{\rho}(\rho v')_z + \left(\frac{\bar{u}_z}{\rho}\right)_z \rho w' \\ + \frac{R}{H}\frac{1}{a\cos\phi}\exp(-\kappa z/H)\theta'_\lambda = 0.\end{aligned} \tag{A.21}$$

Notice that the identities

$$\bar{u}_{zz}w' - \frac{\bar{u}_z\rho_z}{\rho}w' = \left(\frac{\bar{u}_z}{\rho}\right)_z \rho w' \tag{A.22}$$

and

$$\bar{\eta}_z v' + \bar{\eta}v'_z = \left(\frac{\bar{\eta}}{\rho}\right)_z \rho v' + \frac{\bar{\eta}}{\rho}(\rho v')_z \tag{A.23}$$

have been used in the derivation of (A.21). Operating $\bar{\theta}_z^{-1}\overline{[\theta' \times (A.21) + u'_z \times (A.2)]}$ and using the periodic condition in longitude we obtain

$$\begin{aligned}\frac{1}{\bar{\theta}_z}(\overline{u'_z\theta'})_t + \frac{\bar{u}_z}{\bar{\theta}_z}\frac{\overline{\theta'(v'\cos\phi)_\phi}}{a\cos\phi} - \left(\frac{\bar{\eta}}{\rho}\right)_z \frac{\rho}{\bar{\theta}_z}\overline{v'\theta'} - \frac{1}{\bar{\theta}_z}\left(\frac{\bar{\eta}}{\rho}\right)\overline{\theta'(\rho v')_z} \\ + \frac{\rho}{\bar{\theta}_z}\left(\frac{\bar{u}_z}{\rho}\right)_z \rho\overline{\theta' w'} + \frac{\bar{\theta}_\phi}{a\bar{\theta}_z}\overline{u'_z v'} + \overline{u'_z w'} = 0.\end{aligned} \tag{A.24}$$

Adding (A.16) to (A.17) and subtracting (A.24) we obtain

$$-[A_1 + A_2 + A_3]_t = \frac{1}{\bar{\theta}_z}\overline{v'\left(\rho P' - \frac{\bar{\theta}_\phi}{a}u'_z\right)} + \frac{\rho}{\bar{\theta}_z^2}\left[-\bar{P}_z + \frac{\bar{\theta}_\phi}{a}\left(\frac{\bar{u}_z}{\rho}\right)_z + \bar{\theta}_z\left(\frac{\bar{\eta}}{\rho}\right)_z\right]\overline{v'\theta'}$$
$$+ \frac{\bar{\eta}}{\rho\bar{\theta}_z}\overline{\theta'(\rho v')_z} + \frac{\bar{u}_z}{\bar{\theta}_z}\frac{\overline{\theta'(v'\cos\phi)_\phi}}{a\cos\phi} - \overline{u'_z w'} \tag{A.25}$$

where

$$A_1 = \frac{1}{2}\frac{\rho}{\bar{J}}\overline{\Pi'^2}, \qquad A_2 = \frac{1}{2}\frac{\rho}{\bar{\theta}_z^2}\left(\frac{\bar{u}_z}{\rho}\right)_z\overline{\theta'^2}, \qquad A_3 = -\frac{1}{\bar{\theta}_z}\overline{u'_z\theta'}. \tag{A.26}$$

We now convert the right hand side (RHS) of (A.25) into a flux form. Substituting the definition of P' in (A.8) into the first term on the RHS of (A.25) we obtain

$$\frac{1}{\bar{\theta}_z}\overline{v'\left(\rho P' - \frac{\bar{\theta}_\phi}{a}u'_z\right)} = \frac{1}{\bar{\theta}_z}\left[-\overline{v'(u'\cos\phi)_\phi} + \bar{\eta}\overline{v'\theta'}_z + \frac{\bar{u}_z}{a}\overline{v'\theta'}_\phi\right]. \tag{A.27}$$

The coefficient of $\overline{v'\theta'}$ in (A.25) can be written as

$$\frac{\rho}{\bar{\theta}_z^2}\left[-\bar{P}_z + \frac{\bar{\theta}_\phi}{a}\left(\frac{\bar{u}_z}{\rho}\right)_z + \bar{\theta}_z\left(\frac{\bar{\eta}}{\rho}\right)_z\right] = -\frac{\bar{\eta}\bar{\theta}_{zz}}{\bar{\theta}_z^2} - \frac{\bar{u}_z\bar{\theta}_{\phi z}}{a\bar{\theta}_z^2}. \tag{A.28}$$

If we use the identity

$$\frac{1}{\cos\phi}\left[\left(\frac{\bar{u}_z\cos\phi}{a\bar{\theta}_z}\right)_\phi + \left(\frac{\bar{\eta}\cos\phi}{\bar{\theta}_z}\right)_z\right] = -\frac{\bar{\eta}\bar{\theta}_{zz}}{\bar{\theta}_z^2} - \frac{\bar{u}_z\bar{\theta}_{\phi z}}{a\bar{\theta}_z^2} \tag{A.29}$$

in (A.28) we have

$$\frac{\rho}{\bar{\theta}_z^2}\left[-\bar{P}_z + \frac{\bar{\theta}_\phi}{a}\left(\frac{\bar{u}_z}{\rho}\right)_z + \bar{\theta}_z\left(\frac{\bar{\eta}}{\rho}\right)_z\right] = \frac{1}{\cos\phi}\left[\left(\frac{\bar{u}_z\cos\phi}{a\bar{\theta}_z}\right)_\phi + \left(\frac{\bar{\eta}\cos\phi}{\bar{\theta}_z}\right)_z\right]. \tag{A.30}$$

Substituting (A.27) and (A.30) into (A.25) and multiplying the result by $(a\rho\cos\phi)$, after simplification, we obtain

$$-a\rho\cos\phi[A_1 + A_2 + A_3]_t = -\rho\overline{v'(u'\cos\phi)_\phi} - a\rho\cos\phi\overline{u'_z w'}$$
$$+ \frac{\rho}{\cos\phi}\left(\frac{\bar{u}_z\cos^2\phi}{\bar{\theta}_z}\overline{v'\theta'}\right)_\phi + \left(\frac{a\rho\cos\phi\bar{\eta}}{\bar{\theta}_z}\overline{v'\theta'}\right)_z. \tag{A.31}$$

Multiplying the mass continuity equation (A.20) by u' and taking zonal average and then multiplying the result by $-a\rho\cos\phi$ yields

$$-\overline{\rho u'(v'\cos\phi)_{\phi}} - a\cos\phi\overline{u'(\rho w')_z} = 0. \tag{A.32}$$

Adding (A.32) to (A.31) and simplifying we have

$$-\mathcal{A}_t = \frac{\rho}{\cos\phi}\left[\cos^2\phi\left(\frac{\overline{u}_z}{\overline{\theta}_z}\overline{v'\theta'} - \overline{u'v'}\right)\right]_{\phi} + a\cos\phi\left[\rho\left(\frac{\overline{\eta}}{\overline{\theta}_z}\overline{v'\theta'} - \overline{u'w'}\right)\right]_z \tag{A.33}$$

where

$$\mathcal{A} = a\rho\cos\phi(A_1 + A_2 + A_3). \tag{A.34}$$

Equation (A.33) is the inviscid, linearized form of the generalized Eliassen-Palm theorem (1.36) where

$$\mathcal{A} = a\rho\cos\phi\left[\frac{1}{2}\frac{\rho}{\overline{J}}\overline{\Pi'^2} + \frac{1}{2}\frac{\rho}{\overline{\theta}_z^2}\left(\frac{\overline{u}_z}{\rho}\right)_z\overline{\theta'^2} - \frac{1}{\overline{\theta}_z}\overline{u'_z\theta'}\right] \tag{A.35}$$

and the EP flux latitudinal and vertical components are:

$$\begin{aligned} F^{(\phi)} &= a\rho\cos\phi\left(\frac{\overline{u}_z}{\overline{\theta}_z}\overline{v'\theta'} - \overline{u'v'}\right), \\ F^{(z)} &= a\rho\cos\phi\left(\frac{\overline{\eta}}{\overline{\theta}_z}\overline{v'\theta'} - \overline{u'w'}\right). \end{aligned} \tag{A.36}$$

The divergence of the EP flux is

$$\nabla\cdot\mathbf{F} \equiv \frac{1}{a\cos\phi}\frac{\partial}{\partial\phi}(F^{(\phi)}\cos\phi) + \frac{\partial}{\partial z}(F^{(z)}). \tag{A.37}$$

Integrating (A.33) over the domain, the wave activity $\mathcal{A}$ is conserved providing the vertical EP flux, $F^{(z)}$, vanishes on the upper and lower boundaries or, less strictly, there is cancelation of the vertical EP flux on the upper and lower boundary.

REFERENCES

Andrews, D. G. and M. E. McIntyre, 1976: Planetary waves in horizontal and vertical shear: The generalized Eliassen-Palm relation and the mean zonal acceleration. *J. Atmos. Sci.*, **33**, 2031-2048.

Andrews, D. G. and M. E. McIntyre, 1978: Generalized Eliassen-Palm and Charney-Drazin theorems for waves on axissymmetric mean flows in compressible atmospheres. *J. Atmos. Sci.*, **35**, 175–185.

Andrews, D. G., 1987: On the interpretation of the Eliassen-Palm flux divergence. *Q. J. R. Meteorol. Soc.*, **113**, 323–338.

Andrews, D. G., J. R. Holton and C. B. Leovy, 1987: Middle Atmosphere Dynamics. Academic Press Inc., 489pp.

Arfken, G., 1985: Mathematical Methods for Physicists, 3rd Edition. Academic Press Inc., 985pp.

Boville, B. A., 1984: The influence of the polar night jet on the stratospheric circulation in a GCM. *J. Atmos. Sci.*, **41**, 1132–1142.

Boyd, J. P., 1976: The noninteraction of waves with the zonally averaged flow on a spherical earth and the interrelationships of eddy fluxes of energy, heat and momentum. *J. Atmos. Sci.*, **33**, 2285–2291.

Brunet, G., 1994: Empirical normal mode analysis of atmospheric data. *J. Atmos. Sci.*, **51**, 932–952.

—— and R. Vautard, 1996: Empirical normal modes versus empirical orthogonal functions for statistical prediction. *J. Atmos. Sci.*, **53**, 3468–3489.

Buell C. E., 1971: Integral equation representation for "factor analysis". *J. Atmos. Sci.*, **28**, 1502–1505.

——, 1978: The Number of Significant Proper Functions of Two-Dimensional Fields. *J. Appl. Meteor.*, **17**, 717–722.

Butchart, N., S. A. Clough, T. N. Palmer and P. J. Trevelyan, 1982: Simulations of an observed stratospheric warming with quasigeostrophic refractive index as a model diagnostic. *Q. J. R. Meteorol. Soc.*, **108**, 475–502.

Charney, J. G. and P. G. Drazin, 1961: Propagation of planetary-scale disturbances from the lower into the upper atmosphere *J. Geophys. Res.*, **66**, 83–109.

——, and M. E. Stern, 1962: On the stability of internal baroclinic jets in a rotating atmosphere. *J. Atmos. Sci.*, **19**, 159–172.

Dickinson, R. E., 1968: Planetary Rossby waves propagating vertically through weak westerly wind wave guides. *J. Atmos. Sci.*, **25**, 984–1002.

Edmond, H. J. Jr., B. J. Hoskins and M. E. McIntyre, 1980: Eliassen-Palm cross sections for the troposphere. *J. Atmos. Sci.*, **37**, 2600–2616.

Farrell B., 1987: Developing Disturbances in Shear. *J. Atmos. Sci.*, **44**, 2191–2199.

Finger, F. G., M. E. Gelman, J. D. Wild, M. L. Chanin, A. Hauchecorne and A. J. Miller, 1993: Evaluation of NMC upper-stratospheric temperature analyzes using rocketsonde and lidar data. *Bull. Amer. Meteor. Soc.*, **74**, 789–799.

Gill, A. E., 1982: Atmosphere-ocean dynamics. Academic Press Inc., 662 pp.

Hardy, D. M. and J. J. Walton, 1978: Principle components analysis of vector wind measurement. *J. Appl. Meteor.*, **17**, 1153–1162.

Held, I. M., 1985: Pseudomomentum and the orthogonality of modes in a shear flows. *J. Atmos. Sci.*, **42**, 2280–2288.

Holton, J. R., 1992: An Introduction to Dynamic Meteorology, 3rd Edition. Academic Press Inc., 511pp.

Kutzbach, J. E., 1967: Empirical eigenvectors of sea-level pressure, surface temperature and precipitation complexes over North America. *J. Appl. Meteor.*, **6**, 791-802.

Legler, D. M., 1983: Empirical orthogonal function analysis of wind vectors over the tropical Pacific region. *Bull. Amer. Meteor. Soc.*, **64**, 231 241.

Lin, B. D., 1982: The behavior of winter stationary planetary waves forced by topography and diabatic heating. *J. Atmos. Sci.*, **39**, 1206-1226.

Longuet-Higgins, M. S., 1968: The eigenfunctions of Laplace's tidal equations over a sphere. *Series A. Mathematical and physical Sciences*, **262**, 511-607.

Matsuno, T., 1970: Vertical propagation of stationary planetary waves in the winter Northern Hemisphere. *J. Atmos. Sci.*, **27**, 871-883.

——, 1971: A dynamical model of the stratospheric sudden warming. *J. Atmos. Sci.*, **28**, 1479-1494.

North G. R., T. L. Bell, R. F. Cahalan and F. J. Moeng, 1982: Sampling errors in the estimation of empirical normal functions. *Mon. Wea. Rev.*, **110**, 699-706.

Press W. H., B. P. Flannery, S. A. Teukolsky and W. T. Vetterling, 1986: Numerical recipes: The art of scientific computing. Cambridge University Press. 818 pp.

Randel W. J., 1987: The evaluation of winds from Geopotential height data in the stratosphere. *J. Atmos. Sci.*, **44**, 3097-3120.

Shepherd, T. G., K. Semeniuk and J. N. Koshyk, 1996: Sponge layer feedbacks in middle-atmosphere models. *J. Geophys. Res.*, **101**, 23,447-23,464.

Sirovich, L. and R. Everson, 1992: Management and Analysis of Large Scientific Datasets. The International Journal of Supercomputer Applications.

Volume 6, No. 1, spring 1992, pp. 50–68.

Washington W. M. and C. L. Parkinson, 1986: An introduction to three-dimensional climate modeling. University Science Books, 422 pp.